UNIVERSITY OF OKLAHOMA
GRADUATE COLLEGE

MATHEMATICAL MODELING AND ULTRASONIC MEASUREMENT OF SHALE ANISOTROPY AND A COMPARISON OF UPSCALING METHODS FROM SONIC TO SEISMIC

A DISSERTATION
SUBMITTED TO THE GRADUATE FACULTY
in partial fulfillment of the requirements for the
degree of
Doctor of Philosophy

By

DILEEP K. TIWARY
Norman, Oklahoma
2007

UMI Number: 3291054

UMI Microform 3291054

ProQuest Information and Learning Company
300 North Zeeb Road
P.O. Box 1346
Ann Arbor, MI 48106-1346

MATHEMATICAL MODELING AND ULTRASONIC MEASUREMENT OF SHALE ANISOTROPY AND A COMPARISON OF UPSCALING METHODS FROM SONIC TO SEISMIC

A DISSERTATION APPROVED FOR THE SCHOOL OF GEOLOGY AND GEOPHYSICS

By

Dr. Evgeni M. Chesnokov, Co-Chair

Dr. Roger A. Young, Co-Chair

Dr. Jean-Claude Roegiers

Dr. Raymon L. Brown

Dr. James M. Forgotson, Jr.

Dr. Kurt Marfurt

Dr. William Menke

Acknowledgements

I would like to express my deepest gratitude to an erudite professor Evgeni Chesnokov who took the risk of taking me on on as a student. His unwearied teaching, encouragement, guidance, patience, has immensely helped me to transform from a geology to a geophysics major. I am grateful to Dr. Roger Young, my co-advisor, for his guidance and excellent teaching which were the building blocks for this research.

Thanks to the illustrious committee members Dr. Jean-Claude Roegiers, Dr. Raymon Brown, Dr. James Forgotson, Dr. Kurt Marfurt, and Dr. Bill Menke (Columbia University) for their sapient advice and willingness to serve.

My sincere thank goes Dr. Irina Bayuk, Russian Academy of Sciences, who has been instrumental in helping me understand some key physical concepts and computing skills right from the beginning. Thanks to Nikolay Dyaur for his help during ultrasonic measurements. Many thanks to Dr. Alexander Vikhorev, Dr. Sergey Abaseev, and all the people involved with the Institute for Theoretical Geophysics for their insightful suggestions on my research. I am also grateful to Dr. Raymon Brown who was available to help me fine tune my understanding. I must also thank Mike Ammerman for his insightful suggestions and constructive criticisms. Thanks to Jamie Rich and Satish Sinha for their help while they were at the Institute. Thanks to Debbie Bristol and Yasser Mohammed for their co-operation.

Thanks to Devon Energy Inc. for the continuing generous support to the Institute for Theoretical Geophysics. I am thankful to Mr. Charles McBurney, Jr. for providing me a scholarship through the SEG foundation, and also to ConocoPhillips for the SPIRIT Scholarship.

Lastly, thanks to Prerna, my fiancee, for her love and support. Her help during core sampling for ultrasonic measurements is highly appreciated.

Contents

List Of Tables

List Of Figures

Abstract

The anatomy of shale is complicated because lithological heterogeneities are present at a very wide range of scales. Both the mineral and pore space contributions to the net seismic anisotropy of a shale are still subjects for research because of the extreme range of scales involved. There is no microscope of any form that allows all the details of shale to be studied first hand. This research takes what can be determined by microscopes and other available data, such as elastic properties, and develops a quantitative approach to understanding the seismic anisotropy of shale caused by the alignment of clay minerals and pores. In other words, when do the clay platelets dominate the anisotropy and when does the porosity play a role? This question is of interest for exploration purposes because the presence of cracks enhances the permeability. The answer depends upon the saturation of the pores. When the pores are water-filled, the mineral alignment dominates the anisotropy of the shale. When the pores are gas-filled, the pore alignment dominates the anisotropy produced by the mineral alignment to give a new signature to the shale anisotropy. This new signature includes a dramatic change in the S-wave anisotropy where a singularity point (a point where the two S-waves have the same velocity) is created giving a tell-tale signature of the gas.

The theoretical understanding of the effective media modeling is used to model Barnett Shale, which is one of the largest natural gas play in the World. After the estimation of mineralogical assemblage using FTIR- and XRD techniques, forward modeling is used to calculate the elastic properties of the Barnett Shale facies. In order to extract the information about the microstructure of shale, the mineralogy-based elastic constants are matched against laboratory-measured elastic constants using inverse modeling by applying a minimization function.

Upscaling of heterogeneous elastic media requirs accounting for elastic scattering and interaction among various elements of the heterogeneous media. Upscaling method based on pair correlation function approximation provides more accurate upscaling estimate of velocities at surface seismic exploration scales than Backus and simple averaging. The differences in the results are attributed to the energy loss due to elastic scattering.

Chapter 1

Introduction to the Dissertation

It is a well known fact that the earth's crust is heterogeneous, and that the heterogeneities are present at various scales. Seismic wave propagation through subsurface rocks is one of the most effective means to detect the presence of heterogeneity in the earth's crust. The relatively shallow earth's crust is of prime importance to the exploration geophysicist because of the presence of hydrocarbons and other minerals resources. One of the most apparent causes of heterogeneity in hydrocarbon reservoirs is the presence of fractures. Sometimes, these fractures can occur in more than one set. The presence of aligned fractures is not only responsible for making the medium heterogeneous, but also anisotropic. Traditionally, fractures have been generally natural, either open or filled. However, fractures can be created artificially to enhance permeability in unconventional types of reservoirs. This dissertation deals with the very small scale natural fractures in shale.

1.1 Shale

Shale comprises almost 75% of the clastic fill of sedimentary basins (Jones and Wang, 1981). Shale is defined as a fine-grained detrital sedimentary rock, formed by the consolidation of clay, silt, or mud (O'Brian and Slatt, 1990). The term "shale" is used for the smallest grain size in the classification of sedimentary rocks. Throughout this dissertation, shale is considered as an aggregate of clay-sized particles, smaller than 0.004mm ($4\mu m$). Shale is commonly composed of a mixture of clay minerals, quartz, feldspars, carbonate particles, organic material and small amounts of other minerals. The clay minerals, such as illite, smectite, kaolinite and chlorite are generally aligned, which is often suggested as a cause of shale anisotropy. The anisotropy in shale is not only due to clay platelets alignment, but also due to aligned cracks (Schoenberg and Sayers, 1995; Sayers, 2005) as can be observed in Figure 1.2. A crack is defined in this dissertation as an ellipsoidal open space having a non-unity aspect ratio[1].

The main causes of anisotropy in shale considered in this dissertation include:

1. clay minerals alignment,
2. alignment of cracks,
3. aspect ratio of the cracks,
4. friability factor, and
5. contrast between host matrix and crack-filling materials.

It has been assumed that besides clay minerals, all other silty minerals are present in polycrystalline form; hence, they can be considered macroscopically, fulfilling

[1] "The ratio of shorter to longer axes for an ellipse or ellipsoid" by: Sheriff (2002)

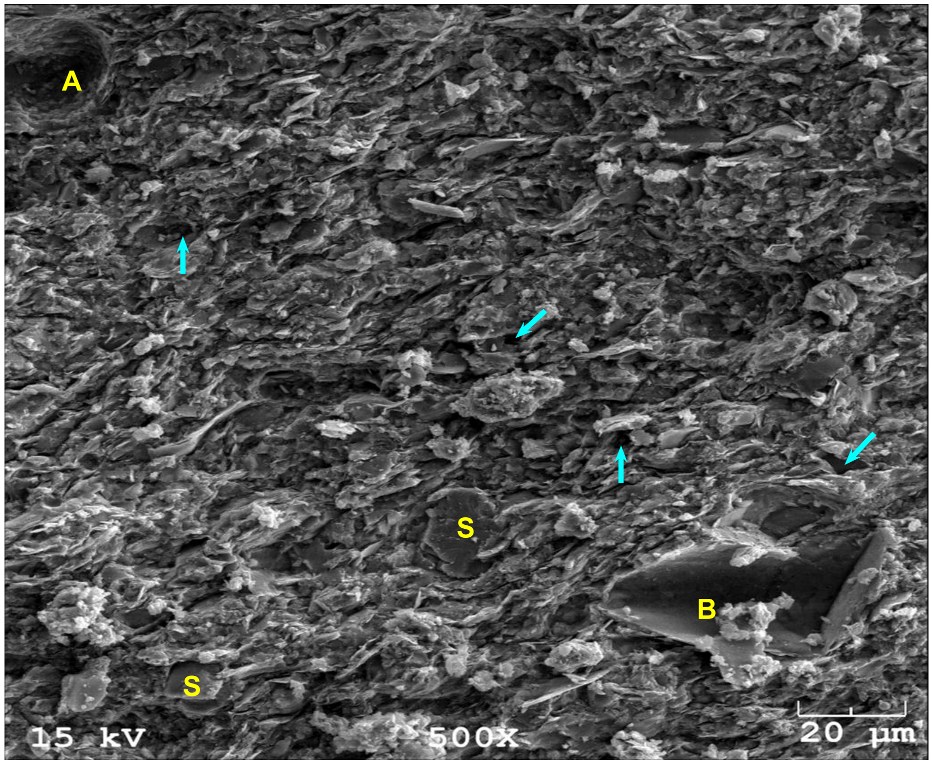

Figure 1.1: SEM photograph showing clay minerals alignment and aligned cracks in shale. The alignment of the clay minerals is modified around silt minerals (S). The blue arrows are pointing to small pores, but most of the cracks are along bedding, and also between the clay platelets. The cavities A and B are created due to dislocation of a silt size grain and dissolved organic matter respectively.

the condition of isotropy because the grains are randomly distributed and oriented (Kriessman et al., 1958).

1.2 Dissertation Objective

Since the seismic method is the most commonly used geophysical method in hydrocarbon exploration, seismic wave propagation in fractured heterogeneous media remains an interesting area of research, in spite of the fact that this topic has been extensively studied. In this dissertation, the main focus will be to evaluate various elements of the shale microstructure, such as clay mineral alignment, crack induced porosity, friability, and the aspect ratio of the cracks that affect the wave propagation in fractured shale reservoirs. Attempts to isolate the effect of the many causes of anisotropy reveal that the overall anisotropy exhibited by shale is controlled by its microstructure. The fractures embedded in an isotropic and anisotropic host rocks have a distinct signature on wave propagation. The disappearance of a singularity point in the shear wave phase velocities when the gas-filled fractures are embedded in isotropic host rocks, and its appearance in water saturated fractures is distinct. Though the disappearance and appearance of a "singularity point"[1] in shear waves can be used to differentiate between the presence of gas or water in the fracture system hosted in an isotropic matrix, the same can not be concluded when the host rock is anisotropic. To my understanding this has never been reported before in the literature.

In order to complement the theoretical investigation carried out in the first two chapters, this dissertation will focuss on a particular shale of interest, the Barnett Shale. What makes this shale interesting is that it is both a source rock as well as a reservoir rock for gas. The prolific gas production from the Barnett Shale has led to a worldwide consideration of the possibility for other potential prolific gas shales. Data from a number of sources and ultrasonic measurements at room temperature are used to study the factors that control the sonic velocity structure which includes any alteration of the core samples as a result of their removal from *in-situ* conditions.

[1] A point where two shear wave velocities are equal (i.e., $V_{S1} = V_{S2}$).

Mineral assemblages of the rock samples belonging to nine different sedimentary facies of the Barnett Shale are estimated through the X-ray diffraction method. These mineral assemblages are used to determine the elastic constants via forward modeling using a general singular approximation (GSA) method based on the effective medium theory (Bayuk and Chesnokov, 1997, 1999). These elastic constants are further used to estimate the aspect ratio of the cracks, friability, crack induced porosity, and the saturation properties and to compare these with the elastic constants extracted from ultrasonic measurements on the samples in the laboratory.

Lastly, the emphasis will be to compare different methods for measurements, such as those in the lab at ultrasonic frequencies, to measurements made at sonic, crosswell and surface seismic frequencies. This is a very important topic if one wishes to use ultrasonic measurements to predict field exploration velocities.

Two considerations are necessary for a complete understanding of the upscaling of laboratory measurements. One of these is the "intrinsic attenuation" due to fluid movement and the other is due to "elastic scattering" from the inhomogeneities of a formation at different scales of measurement. The aim is to understand the issue of upscaling due to the elastic scattering in a formation at different scales. Measurements made in the laboratory on a Barnett Shale core, show strong signs of heterogeneity indicating that the ultrasonic laboratory measurements require upscaling to account for elastic scattering. The three different methods used for upscaling the sonic frequency data to the surface seismic scales show a large variation in the results because each one of them considers different causes for the attenuation.

1.3 Literature Review

In sedimentary rocks, particularly in shale, the two main causes of seismic anisotropy are: (i) clay minerals alignment; and (ii) alignment of the cracks/fractures. Both of these causes are related to the burial history of the rock. A large number of theoretical studies dealing with seismic wave propagation in the cracked media is reported in the literature (Anderson et al., 1974; Hudson, 1980, 1981, 1986; Nishizawa, 1982; Schoenberg and Douma, 1988; Cheng, 1981; Thomsen, 1995; Schoenberg and Sayers, 1995; Crampin, 1978; Crampin et al., 1980; Crampin, 1984; Crampin et al., 1986; Sayers and Kachanov, 1995; Grechka, 2007). These studies can be classified into two categories: the first category includes those models that deal with small concentration and smaller aspect ratio of the cracks (also called the flat crack model), and other models that claim to be valid for the larger concentration and larger aspect ratios of crack can be clubbed in the second category. Another classification can be made among the models that have been studied previously based on interaction and non-interaction approximation. The models which use a non-interaction approximation, assume a very low concentration of cracks in the background matrix. A "very low" concentration implies isolated inclusions embedded into a homogeneous host matrix. In this case if the inclusions are homogeneous and ellipsoidal/elliptical, the exact solution of the problem can be obtained (Levin and Markov, 2005), but if the volume concentration of the inclusions is high, the interactions between the inclusions must be taken into account. In this case the whole system (random inclusions and host matrix) becomes a many-body problem for which no exact solution is possible, and the available solutions are based on approximations. The generalized singular approximation (GSA) method, is one such approximate solution.

Levin and Markov (2005) give a good review of the various effective medium theories and their physical consideration to obtain the solution. The popular self-consistent method is based on the effective medium approximation and reduces a many-body problem to a one-particle situation (O'Connell and Budiansky, 1974; Budiansky and O'Connell, 1976). A method developed by Norris (1985) called "differential effective medium" (DEM), and later used by Hornby et al. (1994) and Jacobsen et al. (2000) can also be considered to be a version of effective medium approximation. The main pitfall of these methods is that the effect of previously modeled inclusions is not considered.

Hudson's (1980, 1981) models are based on first order scattering theory and allows the propagating wave to scatter at the surface of penny-shaped ellipsoidal cracks embedded in an isotropic background matrix. These models are only valid for a low crack concentration. Based on Hudson model, a series of articles have been published by Crampin to explain the observed anisotropy in fractured media (Crampin, 1978, 1984; Crampin et al., 1986, 1980). Hudson's (1986) model which allows high order (second) scattering, predicts high moduli with crack density larger than 0.1 (Cheng, 1981).

The Thomsen (1995) model claims to be valid for a higher degree of crack concentration to estimate the elastic constants of cracked media using a self-consistent approach. This approach, however, takes into account the interaction of the main wave field in a heterogeneous media, but assumes a single heterogeneity in the equivalent homogeneous medium. Schoenberg and Sayers (1995) suggest that the effective compliance tensor of the fractured rock can be expressed as the sum of the background matrix compliance and the compliance of each set of the fractures. The linear-slip interface model of Schoenberg and Douma (1988) considers all types of fracture anisotropy in a general anisotropic elastic background matrix for relatively high aspect ratio (0.03) and low crack density (= 0.05). However, their model is based on the single scattering theory. Recently, Sayers (2005) analyzed the anisotropy of shale due to alignment of cracks and clay minerals. The central hypothesis of Schoenberg and Sayers (1995) and Sayers and Kachanov (1995) is that the effective compliance tensor of the fractured rock can be expressed as the sum of the individual compliance tensors. Grechka (2007) discusses the effect of multiple cracks in transversely isotropic media with a vertical axis of symmetry (VTI) but the analysis is valid only for the small concentration of cracks, because of non-interacting approximation of cracks.

In this dissertation, several types of shales are modeled using the GSA method, which allows arbitrary crack concentration and aspect ratio of the inclusions in the interacting media. The models deal with angle dependence of seismic wave velocity resulting from random, horizontal and vertically aligned cracks in isotropic/anisotropic background matrix. To check the robustness of the methodology, high values of the crack density are modeled to observe their effect on seismic wave propagation.

The second part of the dissertation is an analysis of three different types of seismic upscaling methods of elastic media. Upscaling of the elastic properties is necessary to integrate data obtained at different scales. Technological advancements have led to the acquisition of data at various frequencies to improve seismic imaging. The integration of data acquired at different frequencies is necessary to accomplish this task.

The classical work related to upscaling of heterogeneous media can be found in Postma (1955) Rytov (1956), Backus (1962), Shermergor (1977), Berryman (1979), Schoenberg and Muir (1981), Bayuk et al. (2003), and Vikhorev (2005). Backus's (1962) method of upscaling of thinly layered medium where individual layers are isotropic, is based on a long wavelength approximation; the physical realization of scattering attenuation is not considered. Shermergor (1977) and Schoenberg and Muir (1981) generalized the Backus formulation to allow individual layers to be anisotropic.

Shermergor (1977), Bayuk et al. (2003), and Vikhorev (2005) formulations of upscaling of the heterogeneous media are based on pair correlation and multi-point correlation approximation. The pair correlation approximation allows all the possible interaction between any pair of the heterogeneities present in the medium. The multi correlation approximation allows all the possible interaction that can take place in a heterogeneous medium due to all heterogeneities. The solution of the Green's function in heterogeneous media is based on the Dyson series. In this case, the calculation of the Green's function requires the summation of the infinite terms of the Dyson series. These methods consider different physical phenomena that occur during the wave propagation in heterogeneous media. The results show significant difference in elastic properties obtained by different upscaling methods.

1.4 Dissertation Organization

The dissertation is in two parts. Part one deals with the wave propagation in fractured anisotropic media. The comparison of different seismic upscaling methods is discussed in part two. The salient features of each chapter are organized as follows.

Chapter 2 introduces four different geological models of shale in which aligned /random cracks are embedded in the isotropic/anisotropic host matrix. As a result, these models exhibit different anisotropic symmetries. The most common minerals present in shale are discussed along with their elastic constants, density, and phase and group velocities. The behavior of elastic waves is studied for cracks filled with either gas or water. The mathematical background of the technique used in modeling is discussed. The quantitative analysis of crack-induced anisotropy and clay mineral-induced anisotropy is presented in detail. The results are analyzed and discussed in terms of Thomsen's parameters.

Chapter 3 discusses the effect of the clay mineral alignment, the aspect ratio of the crack, and the friability factor on anisotropy. The gap that exists between model-II and model-III (discussed in Chapter 2) is bridged. The question of what amount of crack-induced porosity is sufficient to dominate the clay mineral-induced anisotropy is investigated. The volume concentration of the aligned clay minerals required to exhibit anisotropy in the presence of aligned cracks is quantified.

Chapter 4 deals with the calculation of elastic constants by forward modeling using mineral assemblage of the rock samples estimated by X-ray diffraction technique and FTIR. Rock samples belonging to nine different facies were especially designed in such a way that the full elastic constants can be extracted for VTI symmetry using ultrasonic laboratory measurements. Inverse modeling is carried out to extract the information about the microstructure of the rock samples.

Chapter 5 compares three different methods of upscaling. The main features of these methods relating their physical considerations, and associated mathematical background are discussed. The concept of the running window to calculate frequency dependent elastic properties is explained. Upscaling methods based on pair correlation function approximation is compared with Backus averaging which does not account for elastic scattering.

Chapter 6 outlines the main conclusions drawn from this research and points out topic for future investigations.

Some of the important mathematical formulations which are helpful in understanding the physical characteristic of the elastic waves are included in the Appendices.

Chapter 2

Mathematical Modeling of Shale to Distinguish Saturation Properties

In this chapter shale anisotropy is modeled to account for alignment of clays and gas or water- filled cracks needs quantitative evaluation. The shale anisotropy in terms of clay mineral alignment and gas/water- filled aligned cracks requires a quantitative analysis. The behavior of P- and S- waves is analyzed when gas- and water-filled cracks are embedded in a host matrix are randomly, horizontally- and vertically aligned. The host matrix can be either isotropic or anisotropic. When the host matrix is isotropic, the presence or absence of a singularity point in shear waves can be used to distinguish between water-filled and gas-filled aligned porosity respectively. If the host matrix is anisotropic, like shale, the behavior of elastic waves depends on the concentration, alignment, aspect ratio, and connectivity of cracks. Quantitative investigation shows that even a small concentration of cracks having low stiffness is sufficient to dominate anisotropy resulting from clay mineral orientation. The models use published mineralogy and clay platelet alignment data along with other micromechanical measurements. The distinction between the models is based upon the alignment of the minerals and the alignment and orientation of the gas-filled cracks. Then the effective media modeling is used to predict the elastic properties of the shale and to identify the dominant contributions to the shale anisotropy. These results have important applications where the seismic is aimed at predicting the maturity state of the shale.

2.1 Introduction

Shales are the most common rocks in sedimentary basins and occur as cap rocks, hydrocarbon-bearing reservoir rocks, and fluid flow barriers. The conventional way (without anisotropy consideration as in the case of sandstone reservoirs) to characterize shales generally fails because of their inherent anisotropy due to clay mineral alignment. Accurate seismic data processing, seismic imaging, and interpretation of AVO anomalies need to account for shale anisotropy. The two main causes of anisotropy in shale are due to partial alignment of clay platelets and microcracks (Tosaya and Nur, 1982; Johnston, 1987; Schoenberg and Douma, 1988; Douma, 1988; Vernik and Nur, 1990; Hornby et al., 1994; Christensen and Johnston, 1995; Sayers, 2005).

Clay minerals in shale generally show preferential orientation, though this does not happen in all depositional environments (O'Brian and Slatt, 1990). The orientation of clay mineral alignment is a function of many factors, indicating depositional environment, state of stress and, diagenesis. Fracture patterns in shale are dependent on the state of stress and their mechanical properties, such as the stiffness of the shale. Multiple fracture sets observed in an outcrop are due to the changes in stress directions over geologic time. Figure 2.1 shows some of the most common combinations of the host rock matrix and the fractures. For simplicity it is assumed that the shale anisotropy is due to the clay mineral alignment and crack alignment. The main goal is to quantify these two causes of shale anisotropy. In other words, what concentration of aligned cracks would be sufficient to dominate the intrinsic anisotropy in shales.

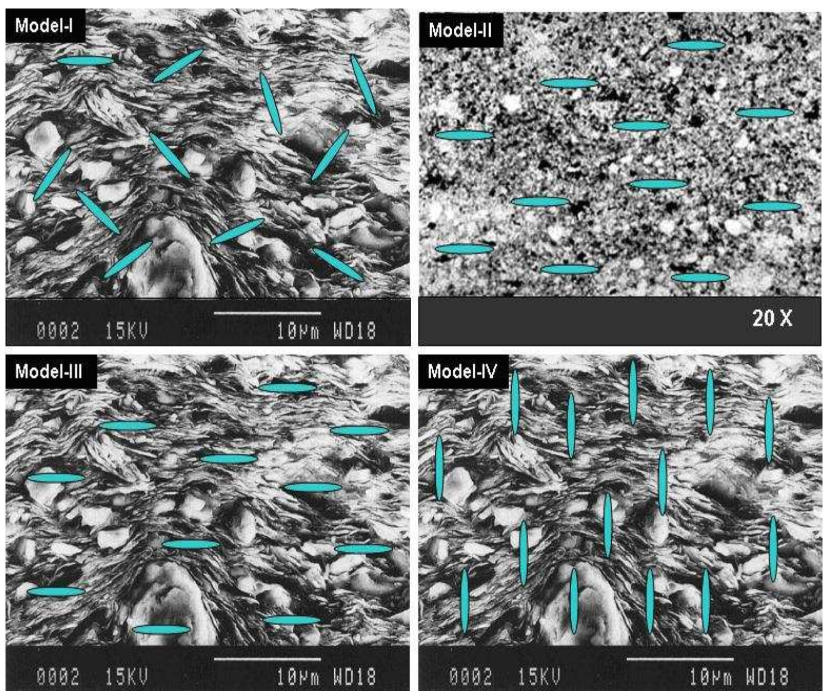

Figure 2.1: Schematic representation of four different types of shale models used to study shale anisotropy. Cyan ellipses represent fractures (or cracks) that are randomly distributed in model-I and aligned in models (II-IV). Model-I: randomly distributed cracks in aligned clay minerals matrix, Model-II: horizontal aligned cracks in randomly oriented clay minerals; Model-III: horizontal aligned cracks in aligned clay minerals matrix; Model-IV: vertical aligned cracks in aligned clay minerals matrix. Modified from (Hornby et al., 1994)
.

Through the construction of theoretical models in which the alignment of minerals and the orientation of microcracks can be controlled, the separate contributions of preferential mineral alignment and the orientation of microcracks to the anisotropy can be estimated (Figure 2.1). In model-I, clays are preferentially aligned and the cracks occur randomly, while in model-II aligned cracks are embedded in randomly distributed clays. Model-I and model-II are constructed to isolate the effect of clay mineral alignment and crack alignment in shale anisotropy. In model-III both clay minerals and cracks are aligned to provide their combined effect on shale anisotropy. In this model the effect of varying crack's concentration on shale anisotropy will be examined. Model-IV considers vertical cracks in a horizontal aligned clay mineral matrix (VTI host matrix). The resulting effective symmetry for this arrangement is orthorhombic. These models are used to determine the relative importance of these two main causes of shale anisotropy.

Clay mineral-induced anisotropy in shales are often cited as the underlying cause of their extreme anisotropy, are scarce (Christensen and Johnston, 1995). Hornby et al. (1994) calculate effective elastic constants as a function of porosity using self-consistent and differential effective medium theory. Their starting matrix is isotropic and anisotropy is due only to aligned cracks. The models in this study start with an anisotropic matrix which accounts for clay mineral alignment and cracks are added as an additional factor to be modeled. The models will separately study the effects of gas-filled and water-filled cracks. Water-filled and gas-filled cracks for different crack porosity have a direct effect on phase velocity (Tiwary et al., 2007b). Bayuk and Chesnokov (1999) compare many effective media modeling methods with the experimental data of Rathore et al. (1995) and conclude that the GSA method provides a better fit than other effective media modeling methods developed by Eshelby (1957), Brown and Corringa (1975) Hudson (1980, 1981), Nishizawa (1982) and Thomsen (1995). While all effective media solutions are based on approximations, the GSA provides the best approximation for the explanation of experimental data (Bayuk and Chesnokov, 1997, 1999).

Sparkman (2006) studied four different models of shale to analyze anisotropy induced by clay mineral alignment and cracks (Figure 2.1). This work differs from Sparkman (2006) who used single crystal illite stiffness tensors as the matrix to estimate effective elastic constants. The models in this study use an illite-rich clay stiffness tensor which has a considerably lower value than the single crystal of illite (Bayuk et al., 2007b). Another significant difference from Sparkman's (2006) modeling is that he does not quantitatively analyze the amount of crack induced porosity required to dominate the anisotropy exhibited due to clay mineral alignment at a given aspect ratio (χ) and friability $\Im$, an empirical parameter that defines the cracks connectivity.

2.2 Common Minerals in Shale

Although shale can be classified as an aggregate of any mineral with grain size smaller than $0.004mm$, the samples analyzed during this research work consist of quartz, calcite, dolomite, siderite, pyrite, apatite, orthoclase, albite and, oligoclase in addition to illite, smectite, kaolinite, chlorite and other mixed clay minerals. Tables 2.1 and 2.2 present the elastic constants and density, as well as the symmetry system of most common shale minerals.

Table 2.1: Elastic constants and density of commonly found minerals in shale. Reference for the elastic constants of different minerals are included in Table 2.2.

C_{ij}	Quartz	Calcite	Dolo-mite	Albite	Clay-water composite	Chlo-rite	Kaoli-nite	Illite-rich clay
C_{11}	86.0	144.5	205.0	74.0	23.66	181.76	171.52	127.387
C_{12}	7.4	57.1	71.0	36.3	12.3	56.76	38.88	48.067
C_{13}	11.91	53.4	57.4	37.6	3.05	20.34	27.11	28.369
C_{14}	-18.04	-20.5	-19.5					
C_{15}			13.7	-9.1				
C_{22}	86.0	144.5	205.0	137.5	23.66	181.76	171.52	127.387
C_{23}	11.91	53.4	57.4	32.6	3.05	20.34	27.11	28.369
C_{24}	18.04	20.5	19.5					
C_{25}			-13.5	-10.4				
C_{26}								
C_{33}	105.75	83.1	113.0	128.9	8.52	106.77	52.63	53.695
C_{34}								
C_{35}				-19.1				
C_{44}	58.2	32.6	39.8	17.2	0.83	11.41	14.76	14.411
C_{45}								
C_{46}			-13.7	-1.3				
C_{55}	58.2	32.6	39.8	30.3	0.83	11.41	14.76	14.411
C_{56}	-18.04	-20.5	-19.5					
C_{66}	39.3	43.7	67.0	31.1	5.71	62.5	66.32	39.66
ρ	2.65	2.7	3.795	2.62	2.17	2.69	2.52	2.70

Microscopic and SEM pictures analyses provide an estimate of mineral orientation. Recently, Wenk and Houtte (2004); Wenk et al. (2007); Lonardelli et al. (2007) used a new high-energy synchrotron X-ray method to provide a more quantitative estimate of mineral phase proportion, crystal structure, grain size and preferred orientation of minerals present in the sample. Wenk et al. (2007) and Lonardelli et al. (2007) claim in their analysis of illite-rich shale, that only clay minerals were aligned. This observation will be used to support the shale models considered for the analysis.

Table 2.2: Most common minerals present in shale and their symmetry system.

Mineral	**Symmetry System**	References
Quartz	Trigonal	Belikov et al. (1970)
Calcite	Trigonal	Peselnick and Robie (1963)
Dolomite	Trigonal	Bass (1995)
Albite	Monoclinic	Belikov et al. (1970)
Illite-rich clay	Hexagonal	Bayuk et al. (2007b)
Chlorite	Hexagonal	Katahara (1996)
Kaolinite	Hexagonal	Katahara (1996)
Clay water composite	Hexagonal	Bayuk et al. (2007a)

2.3 Phase and Group Velocity of Common Minerals in Shale

This section, the phase velocity of shale samples belonging to different symmetry systems due to the alignment in different orientations of clay minerals and cracks is analyzed. The velocity at which a single plane wave propagates in a particular direction is called the phase velocity of the wave. When multiple plane waves interfere, the group velocity of a wave is observed. The phase velocity can be thought of as the plane wave velocity for a single frequency, and a single direction. The group velocity can be thought of as a constructive interference of waves with different phase velocities.

If the variation of the plane wave velocities is all in the same direction, the group velocity is said to represent a dispersive medium because each frequency travels with a different velocity. If the variation of the velocity occurs in different directions, this type of velocity variation is called anisotropy. Sometimes the group velocity for the anisotropic case is called “ray” velocity. If the medium is both dispersive and anisotropic the group velocity is sometimes called "energy" velocity. The phase velocity and the group velocity of a wave can be defined in terms of angular frequency, ω, and wavenumber, k:

$$V_{phase} = \frac{\omega}{k}, \tag{2.1}$$

and

$$V_{group} = \frac{\partial \omega}{\partial k}. \tag{2.2}$$

Understanding the difference between group and phase velocity is imperative in analyzing laboratory measurement. Dellinger and Vernik (1994) numerically show that all pulse transmission experiments measure phase velocity, even when the separation between the transducer is more than three times the width of the transducers. The complete explanation of phase and group velocity is given in Appendix A.

Quartz, dolomite, calcite, kaolinite, chlorite, smectite, and illite are anisotropic shale minerals that occur as polycrystalline aggregates, which may behave isotropically (Chung et al. (1963)) because the grains are randomly distributed and oriented.

Figures 2.2, 2.3 and 2.4 show the phase and group velocities of quartz, calcite, dolomite, albite, kaolinite, chlorite, clay-water composite and illite-rich clay. Figures 2.2, 2.3 and 2.4 show that all minerals are anisotropic in their single crystal form, but their phase and group velocities are different. The most noticeable feature is the "cusp" in the qSV-wave (green) of the group velocity. The cusps in the group velocity of qSV-wave propagation are due to the rapid change of the velocity at the propagation direction near the cusps. This happens because the qSV-waves along one ray path will suffer interference by other neighboring qSV-waves.

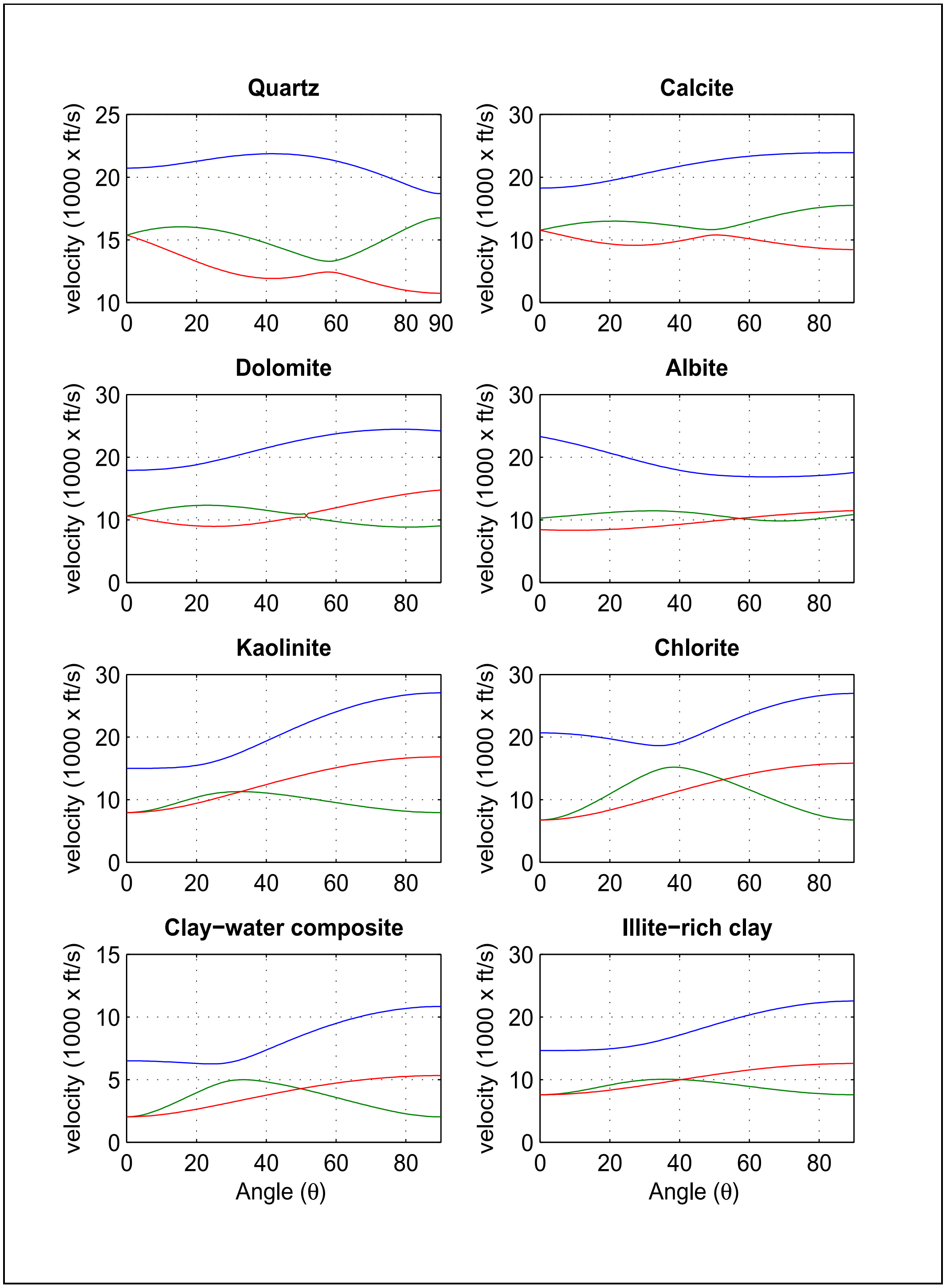

Figure 2.2: Phase velocity of the most common minerals in shale. Color-coded V_p (blue), V_{fast} (green) and V_{slow} (red) are in XZ plane. The source of elastic constants C_{IJ} are shown in Table 2.2. The angle (θ) is measured from the axis of symmetry.

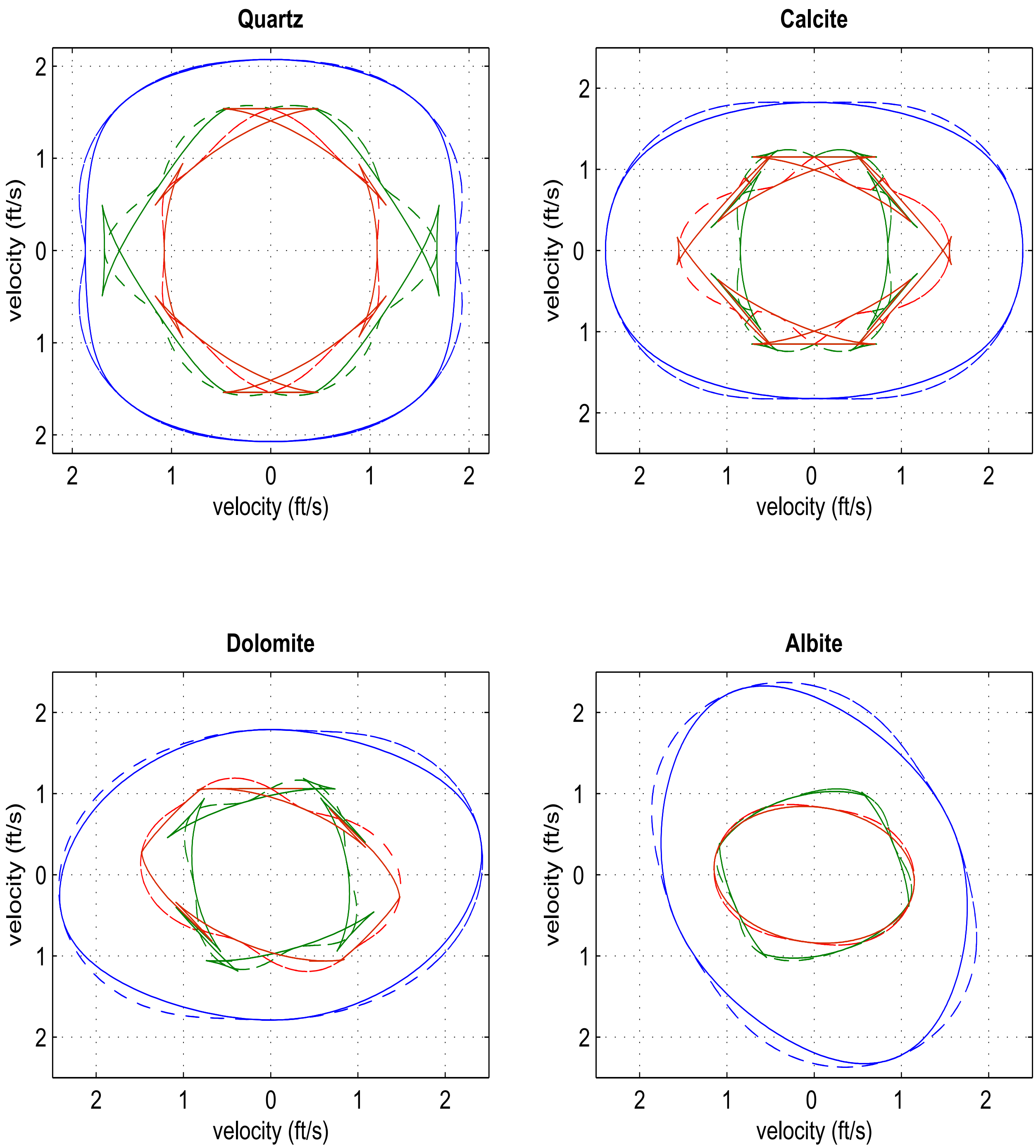

Figure 2.3: Phase velocity (dashed line) and group velocity (solid line) of dolomite, quartz, albite and calcite minerals in XZ-plane. Blue = P-wave, green = S_1 and red = S_2.

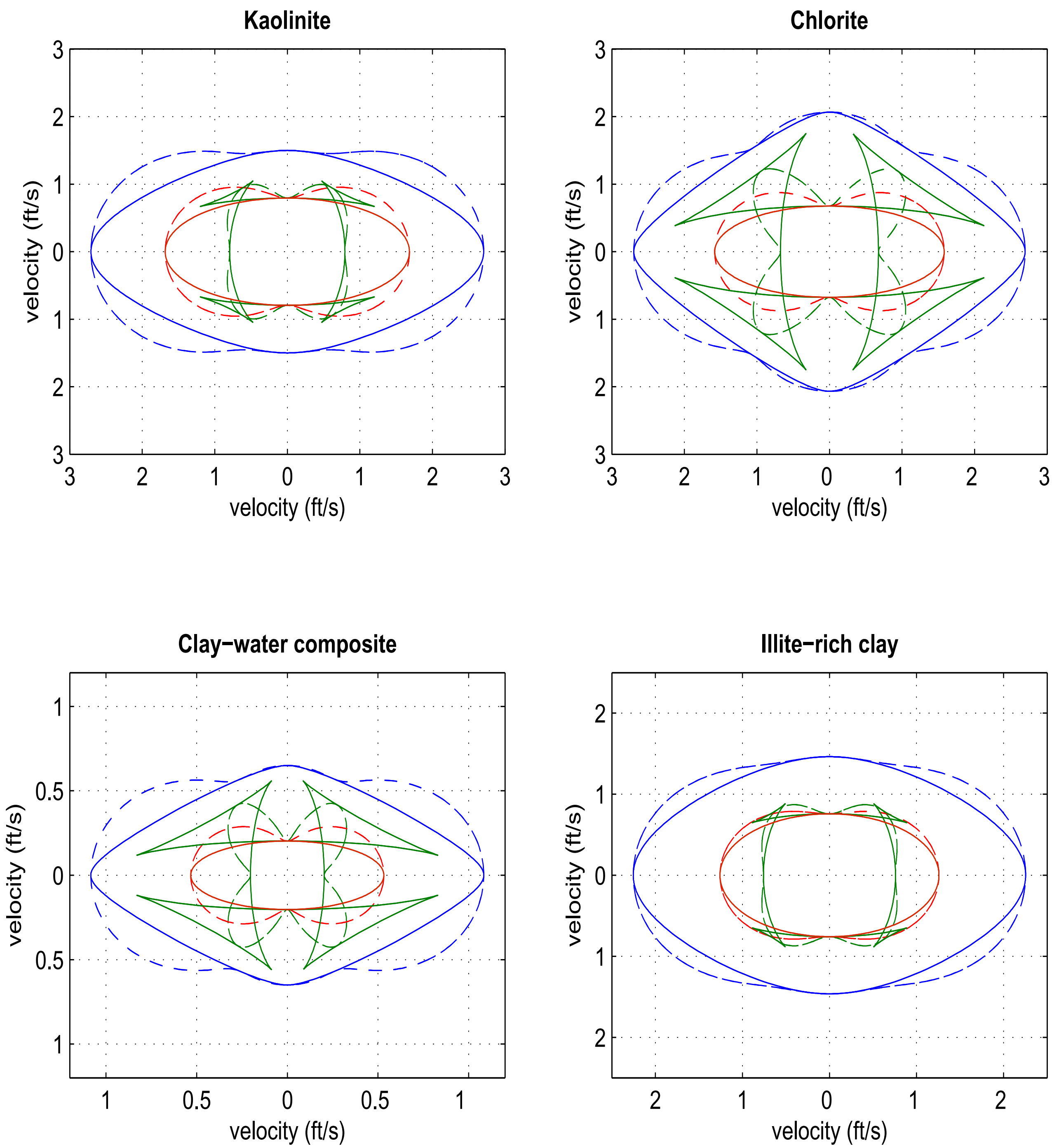

Figure 2.4: Same as Figure 2.3 but for minerals kaolinite, chlorite, clay-water composite and illite-rich clay.

2.4 Wave Propagation in Cracked Media

Wave propagation in cracked media has been studied extensively by many workers, but for limited aspect ratios and crack-induced porosity. The compliance of the crack depends on aspect ratio. The smaller the aspect ratio the larger will be the compliance of the crack. State of stress changes with the depth in the subsurface rocks and hence the aspect ratio of the cracks also changes, provided the rocks are normally pressured. A wide range of the aspect ratio and crack-induced porosity is modeled in this study because each rock behaves differently. Eshelby (1957) gives the static solution based on change in strain field inside a single ellipsoidal inclusion in an isotropic matrix. Hudson (1980, 1981) estimates effective elastic moduli of a medium consisting of thin, penny-shaped ellipsoidal cracks from scattering of the waves on the crack's surface. The Hudson model is valid for small concentrations of cracks having a small aspect ratio. Thomsen's (1995) model, valid for a higher degree of crack concentration, calculates the elastic constants of cracked media using a self-consistent approach. The self-consistent approach takes into account the interaction between heterogeneities within the medium and it assumes a single heterogeneity in an equivalent homogeneous medium. Nishizawa (1982) uses a numerical method to calculate the elastic constants of a cracked homogeneous matrix beginning with a single crack in the matrix and then replacing the initial matrix by the modified matrix to include successively more and more cracks, with no theoretical limit on the crack concentration. The effective media modeling methods mentioned above are not based on the many-body problem, because they either consider a small concentration of cracks, or the cracks are included in steps ignoring the interaction with previously included cracks. In contrast the GSA method computes the effective elastic constants of cracked anisotropic media for arbitrary crack concentration and aspect ratio. The GSA formulation takes into account the interaction between all heterogeneities (cracks) (Bayuk and Chesnokov, 1999).

2.5 Effective Media Modeling

2.5.1 Macroscopic Effective Properties of Random Heterogeneous Arbitrary Anisotropic Media

Following Shermergor's (1977) representation, stress, strain and stiffness tensors in random heterogeneous arbitrary anisotropic media are expressed in the following forms:

$$\begin{aligned} \sigma_{ij}(\mathbf{x}) &= \langle\sigma_{ij}\rangle + \sigma^{'}_{ij}(\mathbf{x}), \\ \varepsilon_{ij}(\mathbf{x}) &= \langle\varepsilon_{ij}\rangle + \varepsilon^{'}_{ij}(\mathbf{x}), and \\ C_{ijkl}(\mathbf{x}) &= \langle C_{ijkl}\rangle + C^{'}_{ijkl}(\mathbf{x}) \end{aligned} \tag{2.3}$$

where $\sigma_{ij}(\mathbf{x})$, $\varepsilon_{ij}(\mathbf{x})$, and $C_{ijkl}(\mathbf{x})$ represent stress, strain and the stiffness tensors, respectively. The angle bracket $\langle\ \rangle$ denotes the average value over a representative volume within which the medium is statistically homogeneous. $\sigma^{'}_{ij}(\mathbf{x})$, $\varepsilon^{'}_{ij}(\mathbf{x})$ and $C^{'}_{ijkl}(\mathbf{x})$, represent the fluctuations from the average value in stress, strain, and stiffness tensors at an arbitrary point $\mathbf{x}$ in a medium.

In random heterogeneous arbitrary anisotropic media, Hooke's law is given by

$$\sigma_{ij}(\mathbf{x}) = C_{ijkl}(\mathbf{x})\varepsilon_{kl}(\mathbf{x}). \tag{2.4}$$

Substituting equation 2.3 into equation 2.4 and averaging the results

$$\langle\sigma_{ij}\rangle = C^{*}_{ijkl}\langle\varepsilon_{kl}\rangle, \tag{2.5}$$

where, C^{*}_{ijkl} is the effective stiffness tensor.

Assuming that the relation between ε and $\langle\varepsilon\rangle$ can be written in the form

$$\varepsilon^{'}_{ij}(\mathbf{x}) = Q_{ijkl}\langle\varepsilon_{kl}\rangle, \tag{2.6}$$

or

$$\varepsilon^{'}_{ij}(\mathbf{x}) = \int Q_{ijkl}(\mathbf{x}-\mathbf{x}^{'})\langle\varepsilon_{kl}(\mathbf{x})\rangle dx^{'}, \tag{2.7}$$

where, $\mathbf{Q}$ is a functional (an integral operator) that depends an interaction between different elements of structure. In this study it is an interaction between the inclusions. The calculation of the functional, $\mathbf{Q}$, leads to a many-body problem (to be discussed in Chapter 5) that can can expressed as

$$C^{*}_{ijkl} = \langle C_{ijkl}\rangle + \langle C^{'}_{ijmn}Q_{mnkl}\rangle. \tag{2.8}$$

Levin and Markov (2005) state that there is no analytical solution of the 'many-body problem'. However, there are several different approximations to find the effective stiffness tensor defined by equation 2.8. In general, the effective and the average stiffness tensors are not equal in random inhomogeneous medium.

Equation 2.6 shows that the problem of determination of the effective stiffness tensor is reduced to determining a functional $\mathbf{Q}$, relating local and average strains.

If the wavelength is much greater than the inclusion size, the expression for the static effective elastic constants in equation 2.8, can be estimated using the equilibrium equation

$$\frac{\partial \sigma_{ij}(\mathbf{x})}{\partial x_j} = -f_i, \tag{2.9}$$

where, f_i is the the body force density function.

The stiffness tensor is represented in the form $\mathbf{C} = \mathbf{C}^0 + \mathbf{C}^{'}$, where $\mathbf{C}^0$ is a homogeneous comparison body with known properties and $\mathbf{C}^{'}$ is the fluctuation about the comparison body. Using equation 2.3

$$\frac{\partial}{\partial x_j} C^0_{ijkl} \varepsilon_{kl}(\mathbf{x}) + \frac{\partial}{\partial x_j} C^{'}_{ijkl}(\mathbf{x}) \varepsilon_{kl}(\mathbf{x}) = -f_i, \tag{2.10}$$

where, ε_{kl} are the component of the strain tensor, C^0_{ijkl} and $C^{'}_{ijkl}$ are the elasticity tensor of the comparison body and the fluctuation of the elasticity tensor from the comparison body respectively.

The derivation of the GSA method formula is based on the difference in displacements between a heterogeneous body and the comparison body subjected to an applied force under the same boundary conditions. The displacement $U_i(\mathbf{x})$ is expressed in terms of mean, $U^0_i(\mathbf{x})$, and fluctuations $U^{'}_i(\mathbf{x})$

$$U_i(\mathbf{x}) = U^0_i(\mathbf{x}) + U^{'}_i(\mathbf{x}), \tag{2.11}$$

where $\mathbf{U}^0$ represents the displacement of the comparison body, and is a solution for equation 2.10 when $\mathbf{C}^{'} = 0$.

Following Shermergor (1977) equation 2.11 can be expressed as

$$U_i^{'}(\mathbf{x}) = \int G_{ki}^0(\mathbf{x} - \mathbf{x}^{'}) \frac{\partial}{\partial x_l^{'}} C_{klmn}^{'}(\mathbf{x}^{'}) U_{m,n}(\mathbf{x}^{'}) d\mathbf{x}^{'}, \tag{2.12}$$

where G_{ik}^0 is Green's function, which describes the properties of the comparison body.

Substituting equation 2.12 in to equation 2.11, gives

$$U_i(\mathbf{x}) = U_i^0(\mathbf{x}) + \int G_{ki}^0(\mathbf{x} - \mathbf{x}^{'}) \frac{\partial}{\partial x_l^{'}} C_{klmn}^{'}(\mathbf{x}^{'}) U_{m,n}(\mathbf{x}^{'}) d\mathbf{x}^{'}. \tag{2.13}$$

Replacing index, i, with index, j gives

$$U_j(\mathbf{x}) = U_j^0(\mathbf{x}) + \int G_{kj}^0(\mathbf{x} - \mathbf{x}^{'}) \frac{\partial}{\partial x_l^{'}} C_{klnm}^{'}(\mathbf{x}^{'}) U_{n,m}(\mathbf{x}^{'}) d\mathbf{x}^{'}. \tag{2.14}$$

Applying the operator $\frac{\partial}{\partial x_j}$ to equation 2.13 and $\frac{\partial}{\partial x_i}$ to equation 2.14, and adding the results, Bayuk and Chesnokov (1997) obtain an equation for the strain tensor

$$\varepsilon_{ij}(\mathbf{x}) = \varepsilon_{ij}^0 + \frac{1}{2} \int \left[\left(G_{ki,j}^0(\mathbf{x} - \mathbf{x}^{'}) + G_{kj,i}^0(\mathbf{x} - \mathbf{x}^{'}) \right) \right] \frac{\partial}{\partial x_l^{'}} C_{klmn}^{'}(\mathbf{x}^{'}) \varepsilon_{mn}(\mathbf{x}^{'}) d\mathbf{x}^{'}, \tag{2.15}$$

or,

$$\varepsilon_{ij}(\mathbf{x}) = \varepsilon_{ij}^0 + Q_{ijkl} C_{klmn}^{'} \varepsilon_{mn}(\mathbf{x}), \tag{2.16}$$

where

$$Q_{ijkl}(\mathbf{x}-\mathbf{x}^{'})C_{klmn}(\mathbf{x}^{'})\varepsilon_{mn}(\mathbf{x}^{'}) \equiv \frac{1}{2}\int\Big[G_{ki,jl}(\mathbf{x}-\mathbf{x}^{'})+G_{kj,il}(\mathbf{x}-\mathbf{x}^{'})\Big]C_{klmn}(\mathbf{x}^{'})\varepsilon_{mn}(\mathbf{x}^{'})d\mathbf{x}^{'}. \tag{2.17}$$

Equation 2.17 represents the same functional that was previously used in equation 2.6.

2.5.2 Formal Solution of the Effective Elastic Tensor

Rewriting equation 2.16

$$\varepsilon_{ij}(\mathbf{x}) = \varepsilon_{ij}^{0} + Q_{ijkl}C_{klmn}^{'}\varepsilon_{mn}(\mathbf{x}), \tag{2.18}$$

and, using the rule of permutation of the indices gives

$$\varepsilon_{ij}(\mathbf{x}) = I_{ijmn}\varepsilon_{mn}(\mathbf{x}). \tag{2.19}$$

From equations 2.18 and 2.19

$$I_{ijmn}\varepsilon_{mn}(\mathbf{x}) = \varepsilon_{ij}^{0} + Q_{ijkl}C_{klmn}^{'}\varepsilon_{mn}(\mathbf{x}), \tag{2.20}$$

or

$$\Big[I_{ijmn} - Q_{ijkl}C_{klmn}^{'}\Big]\varepsilon_{mn}(\mathbf{x}) = \varepsilon_{ij}^{0}. \tag{2.21}$$

Using equation 2.21 gives

$$\varepsilon_{mn}(\mathbf{x}) = D_{mnij}\varepsilon_{ij}^{0},$$

where

$$D_{mnij} \equiv \left[I_{mnij} - Q_{mnkl} C^{'}_{klij} \right]^{-1}.$$

The formal solution of equation 2.18 is thus

$$\varepsilon_{mn}(\mathbf{x}) = \left[I_{ijmn} - Q_{ijkl} C^{'}_{klmn} \right]^{-1} \varepsilon^0_{ij} \ . \tag{2.22}$$

Averaging equation 2.22 gives

$$\Big\langle \varepsilon_{mn}(\mathbf{x}) \Big\rangle = \Big\langle \left[I_{mnij} - Q_{mnkl} C^{'}_{klij} \right]^{-1} \Big\rangle \varepsilon^0_{ij} \tag{2.23}$$

where $I_{ijkl} = \frac{1}{2}(\delta_{ik}\delta_{jl} + \delta_{il}\delta_{jk})$ is the unit tensor,

$\delta_{ij} = \begin{cases} 0 & \text{if } i \neq j, \\ 1 & \text{if } i = j. \end{cases}$ is the Kroneker delta, and

$\langle \ \rangle$ denotes the average value.

Equation 2.23 represents the average strain of the medium that can be obtained by averaging the expression 2.22.

Multiplying equation 2.23 by $\mathbf{C}$, and expressing the results in tensor form gives

$$\langle \mathbf{C}\boldsymbol{\varepsilon} \rangle = \Big\langle \mathbf{C}\big[\boldsymbol{I} - \mathbf{Q}\mathbf{C}^{'} \big] \Big\rangle \boldsymbol{\varepsilon}^{\mathbf{0}}. \tag{2.24}$$

Equation 2.5 can also be written without indices:

$$\big\langle \mathbf{C}\boldsymbol{\varepsilon} \big\rangle = \mathbf{C}^{*} \langle \boldsymbol{\varepsilon} \rangle. \tag{2.25}$$

Comparing equation 2.24 with equation 2.25 gives

$$\mathbf{C}^{*}\langle\varepsilon\rangle = \left\langle \mathbf{C}\left[\boldsymbol{I} - \mathbf{Q}\mathbf{C}'\right]\right\rangle \boldsymbol{\varepsilon}^{\mathbf{0}}. \tag{2.26}$$

From equation 2.23

$$\boldsymbol{\varepsilon}^{\mathbf{0}} = \left\langle \left[\mathbf{I} - \mathbf{Q}\mathbf{C}'\right]^{-1}\right\rangle^{-1} \left\langle \varepsilon \right\rangle. \tag{2.27}$$

Substituting equation 2.27 into equation 2.26, provides the following final expression

$$\mathbf{C}^{*} = \left\langle \mathbf{C}\left(\mathbf{I} - \mathbf{Q}\mathbf{C}'\right)\right\rangle \left\langle \left(\mathbf{I} - \mathbf{Q}\mathbf{C}'\right)^{-1}\right\rangle^{-1}. \tag{2.28}$$

Equation 2.28 gives the exact solution of the problem of the effective elastic tensor for a randomly inhomogeneous arbitrary anisotropic medium and coincides with Shermergor's (1977) equation 9.12 (p.165). The operator **Q** is an integral operator over coordinates. The GSA method uses equation 2.28 to estimate the effective elasticity tensors that provide the best fit to experimental data (Bayuk et al., 1998, 1999).

2.6 The General Singular Approximation (GSA) Method

The General Singular Approximation (GSA) method was first suggested by Shermergor (1977) and Willis (1977). It is assumed that the inclusions are all of ellipsoidal shape. The operator $\mathbf{Q}(\mathbf{x}-\mathbf{x}^{'})$ in equation 2.28 is replaced by a local operator $\mathbf{g}(\mathbf{x})$, which reflects the local interaction:

$$Q_{ijkl}(\mathbf{x}-\mathbf{x}^{'}) = g_{_{ijkl}}\delta(\mathbf{x}-\mathbf{x}^{'}), \tag{2.29}$$

where

$$g_{_{ijkl}}(\mathbf{x}) = \int d\mathbf{x}^{'} Q_{ijkl}(\mathbf{x}-\mathbf{x}^{'}). \tag{2.30}$$

In equation 2.29, the integral operator $\mathbf{Q}$ becomes a constant tensor at point $\mathbf{x}$. Shermergor (1977) showed that $\mathbf{g}$ can be expressed in a homogeneous isotropic medium as,

$$g_{_{ijkl}} = -\frac{1}{3\mu^0}\left[I_{ijkl} - \frac{1}{5}\left(\frac{\lambda^0+\mu^0}{\lambda^0+2\mu^0}\right)\delta_{ijkl}\right], \tag{2.31}$$

where $\left(\frac{\lambda^0+\mu^0}{\lambda^0+2\mu^0}\right)$ is the comparison body and λ, μ are the Lamé's parameters. The term δ_{ijkl} is not the usual Kronecker's delta as it contains four free independent indices, but can be represented in terms of Kronecker's delta as follows:

$$\delta_{ijkl} \equiv \delta_{ij}\delta_{kl} + \delta_{ik}\delta_{jl} + \delta_{il}\delta_{jk}, \tag{2.32}$$

where $i, j, k, l = 1, 2$ and 3.

For an effectively homogeneous isotropic two phase medium, the stiffness parameters $K^{^*}$ and μ^* can be found using Shermergor (1977):

$$\frac{1}{K^* + b_K^0} = \frac{v_1}{K_1 + b_K^0} + \frac{v_2}{K_2 + b_K^0}, \tag{2.33}$$

and

$$\frac{1}{\mu^* + b_\mu^0} = \frac{v_1}{\mu_1 + b_\mu^0} + \frac{v_2}{\mu_2 + b_\mu^0}, \tag{2.34}$$

where v_1 and v_2 are the volume concentration of two phases. b_K^0 and b_μ^0 can be expressed in terms of the bulk and shear moduli as

$$b_K^0 = \frac{4}{3}\mu^0, \tag{2.35}$$

and

$$b_\mu^0 = \frac{\mu^0(9K^0 + 8\mu^0)}{6(K^0 + 2\mu^0)}. \tag{2.36}$$

In general anisotropic media the local operator **g** takes a more complicated form (Shermergor, 1977) than shown in equation 2.31, and is summarized in Appendix B. Also, for general elastic media, equation 2.28 can be rewritten as:

$$\mathbf{C}^* = \left\langle \mathbf{C}(\mathbf{I} - \mathbf{Q}\mathbf{C}') \right\rangle \left\langle (\mathbf{I} - \mathbf{Q}\mathbf{C}')^{-1} \right\rangle^{-1}. \tag{2.37}$$

If the medium is statistically homogeneous, following the ergodicity hypothesis the volume average can be expressed as a statistical average. If the heterogeneities differ in their elastic properties, shape, and orientation, equation 2.37 can be written as

$$\begin{aligned} C^* \;=\; & \left\{ \sum_{i=1}^{n} v_i \mathbf{C}_i \int P_i(\chi_i; \theta, \phi, \psi) \left[\mathbf{I} - g_i(\mathbf{C}_i - \mathbf{C}^0)\right]^{-1} \sin\theta \; d\chi_i \; d\theta \; d\phi \; d\psi \right\} \times \\ & \left\{ \sum_{i=1}^{n} v_i \int P_i(\chi_i; \theta, \phi, \psi) \left[\mathbf{I} - g_i(\mathbf{C}_i - \mathbf{C}^0)\right]^{-1} \sin\theta \; d\chi_i \; d\theta \; d\phi \; d\psi \right\}^{-1} . \end{aligned} \tag{2.38}$$

where, v_i and $\mathbf{C}_i$ are the volume concentration and the elasticity tensor of the i^{th} component respectively. $\mathbf{I}$ is a rank four unit tensor. The tensor $\mathbf{C}^0$ is the elasticity tensor of the so-called comparison body, which can be arbitrarily chosen. The tensor $\mathbf{g}$ is controlled by the properties of the comparison body and the inclusion shape. χ is the aspect ratio of the inclusions, and θ, ϕ and ψ are the three Euler angles.

2.7 Friability Factor

In clastic sedimentary rocks, particularly in shale, only some of the pores and cracks are interconnected, such that the permeability of the rocks is low, even though the porosity is high (e.g. chalk). To model this type of rock, an empirical dimensionless parameter, friability ($\Im$), is introduced in the formulation to reflect the connectivity of the crack system. The value of friability ranges between 0 to 1, where ($\Im$) =0 means all the cracks are isolated and ($\Im$) = 1 means all cracks are connected. Friability quantifies the connectivity of the cracks, and is used to choose the stiffness of the comparison body (C^c). Bayuk and Chesnokov (1997) define the stiffness of the comparison body C^c

$$C^c = C^m(1 - \Im) + C^I \Im, \tag{2.39}$$

where, C^m and C^I are the elasticity tensor of matrix minerals and inclusions respectively, and $\Im$ is the friability factor.

This form of the comparison body helps to achieve upper and lower Hashin-Shtrikman bounds when $\Im$ is equal to 0 and 1, respectively. The Hashin-Shtrikman bounds are the upper and lower limits of the elastic constants for a composite depending upon the microgeometry of the composite (Mavko et al., 1998).

Xu and White (1996) proposed an alternative comparison body $C^c = C^m(1 - \phi\Im) + C^I\phi\Im$ where ϕ is the volume concentration of cracks, C^m and C^I are the elasticity tensor of matrix minerals and inclusions respectively, and $\Im$ is the friability factor. Unfortunately, this form of the comparison body does not give the lower Hashin-Shtrikman bound. For this reason, equation 2.39 will be used for the comparison body.

2.8 Modeling Steps

A simplified view of shales is that they are composed of matrix and inclusions. These inclusions can be either solid silty grains (quartz) or other granular materials (pyrite, dolomite, calcite, feldspar, etc.), or pores and fractures filled by gas, oil or water, or a combination of both. Hornby et al. (1994) assumed that the clay minerals matrix should be modeled first, and the inclusions should be introduced then in a second step . Furthermore, the soft component of a composite should be modeled first followed by a relatively harder component. Thus, the clay minerals matrix is adopted as the starting point when modeling shale. The following workflow is used in this study to model shale:

- approximate the matrix properties using the illite-rich clay mineral effective elastic constants;
- introduce all other minerals (quartz, calcite, dolomite, pyrite, feldspar, etc.) as inclusions and estimate the effective elastic constants of the composite as a function of porosity (0 - 100%);

- select elastic constants at the percentage which equals the percentage of the inclusions;
- define the aspect ratio of the cracks and introduce them into the matrix;
- define gas, oil or brine as the saturation properties of the cracks; and,
- define the friability value (an empirical parameter that reflects the connectivity of the fractures) of the rock.

Effective medium theory described above makes it possible to calculate the stiffness tensor relating strain and stress averaged over a representative volume. The inclusions here are: silty and granular minerals, pores, and cracks. The GSA method makes it possible to take into account the microstructure of a medium including shape of grains and ellipsoidal cracks, the crack connectivity to the matrix (friability) and their orientation in the medium (distribution function).

2.9 Effective Media of the Four Shale Models

Shales are very complicated rocks in which the shape, concentration, and connectivity of pores changes from sample to sample. The shale shown in Figure 2.1 is modeled for different combination of aspect ratio (from 10^{-5} to 1), friability factor (0.6 to 1), and crack-induced porosity (0.001 to 5%). In order to distinguish gas-filled and water-filled crack, four simple models of shale are used because the distinction is of economic interest. O'Brian and Slatt's (1990) analysis of a Huron shale composed of (63%) clay minerals, (31%) quartz, (4%) albite, and (2%) pyrite is used as the starting mineral assemblage. The clay minerals are mainly 87% illite and 13% chlorite. The elastic constants of illite-rich clay minerals and other minerals are are shown in Table 2.1.

Table 2.3: The values of aspect ratio, friability factors, and crack induced porosities for which all the four shale models are analyzed. The values of aspect are considered starting from 10^{-5}. On the main plot it may appear that the the same value of Φ, χ, and $\Im$ is representing singularity and no-singularity point, but that is not true. The points on the singularity and no-singularity plots have different values of Φ, χ, and $\Im$.

Crack's parameters	**Values**
Aspect ratio	0.00001, 0.0001, 0.0005, 0.001, 0.005, 0.01, 0.02, 0.03, 0.04, 0.05, 0.06, 0.08, 0.1, 0.2, 0.5, 1
Friability	0.6, 0.65, 0.7, 0.75, 0.8, 0.85, 0.9
Crack porosity	0.001, 0.005, 0.01, 0.05, 0.1, 0.2, 0.3, 0.4, 0.5, 0.6, 0.7, 0.8, 0.9, 1.0, 1.2, 1.5, 2.0, 2.5, 3.0, 4.0, 4.5, 5.0

2.9.1 Shale Model-I

In model-I (Figure 2.1) the total anisotropy is due to aligned clay platelets preferentially aligned in horizontal plane. Since the fractures are randomly oriented in the medium; and, hence, they do not contribute to the total anisotropy. Other minerals are considered as spherical inclusions in the system and, therefore, they do not play any role in the total anisotropy. Due to horizontal alignment of the clay minerals the medium will exhibit transversely isotropic symmetry with a vertical symmetry axis (VTI).

Model-I is analyzed for different values of aspect ratio, friability factors and total crack induced porosities (Table 2.3) and compute the stiffness matrix using equation 2.38. Then from the effective stiffness matrices the Thomsen's parameters (ε, γ, and

δ) are derived. In order to keep the model realistic, only those stiffness matrices are analyzed where the value of Thomsen's parameters (ε, γ, and δ) are less than unity. In nature it is highly uncommon for rock to exhibit Thomsen's parameters greater than unity, which correspond to a very high value of anisotropy coefficient. The mathematical expression for the Thomsen's VTI parameters (Thomsen, 1986) and orthorhombic media (Tsvankin, 1997) are summarized in Appendix-C.

Figure 2.5 shows combinations of aspect ratio, friability and crack-induced porosity for the gas-filled and water-filled cracks, color-coded by Thomsen's parameters. When the cracks are gas-filled, the shear waves (V_{S1} and V_{S2}) show a singular value (when V_{S1} and V_{S2} are equal) between 0^0 and 90^0, plotted in polar plane (Figure 2.7). The same behavior of shear wave velocity is noticed in a majority of cases when the cracks are water-filled. However, there are some cases, where shear waves do not show a singular value (Figure 2.6). Figure 2.6 shows that water-filled cracks do not exhibit singular values when the aspect ratio of the cracks is very small and when the crack-induced porosities are rather high. Analysis of crack densities shows that the these points happen to have very large crack density, which is higher than the threshold crack density (beyond which rocks lose their stability) for the crustal rocks (Crampin and Leary, 1993; Crampin, 1994). It can be concluded that if aligned clays are the cause of anisotropy, the shear wave will always show singularity point. In Figure 2.5 the P-wave anisotropy, ϵ, for gas-saturated cracks is relatively higher than water-filled cracks because of a smaller contrast in the case of water-filled cracks. However, δ, is relatively smaller in the gas-filled cracks model than its corresponding water-filled crack model. There is no significant change in γ, since shear waves are not sensitive to the fluid properties.

Figure 2.7 shows the phase velocity for three different values of crack concentration for the gas-filled and water -filled cracks. The anisotropic behavior of the P-wave and S- wave velocities is the same in gas-filled and water-filled cracks if the cracks are randomly oriented in VTI matrix. Even though the behavior of the phase velocity is consistent with the increase in porosity, the velocity decreases with the increase in porosity. The theoretical results obtained here help to explain the experimental data of Johnston and Christensen (1994). Johnston and Christensen's (1994) P- and S- waves velocities measured on a dry shale sample show an increase in P-wave velocity from 0^0 to 90^0 (0^0 being normal to the bedding plane), and a singularity point in the shear wave velocities. They report that when anisotropy is due to clay mineral alignment, the rate of increase in V_p and V_{sh} will be greatest between 20^0 and 70^0 which is also observed in the results obtained here in Figure 2.7.

GAS SATURATED **WATER SATURATED**

singularity point **singularity point**

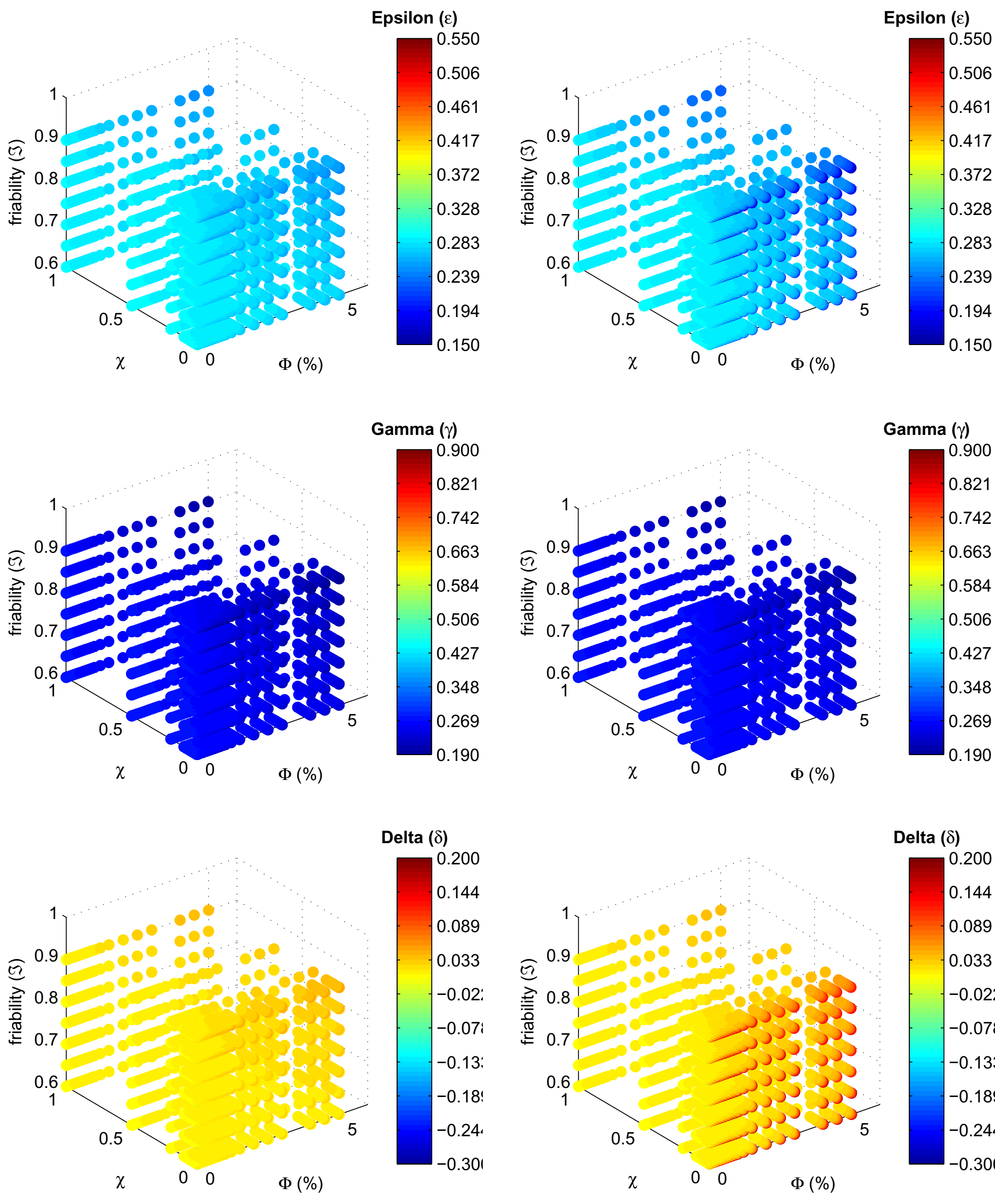

Figure 2.5: 3D plot of crack-induced porosities (Φ), aspect ratio (χ), and friability factor ($\Im$), color coded by Thomsen's parameters (ε, γ, and δ). For each point on the plot, the elastic constants of the corresponding effective medium are calculated. Only those points are shown which provide singular value in the shear waves for both gas-filled and water-filled cracks. Singularity point occurs when $V_{S1} = V_{S2}$.

WATER SATURATED

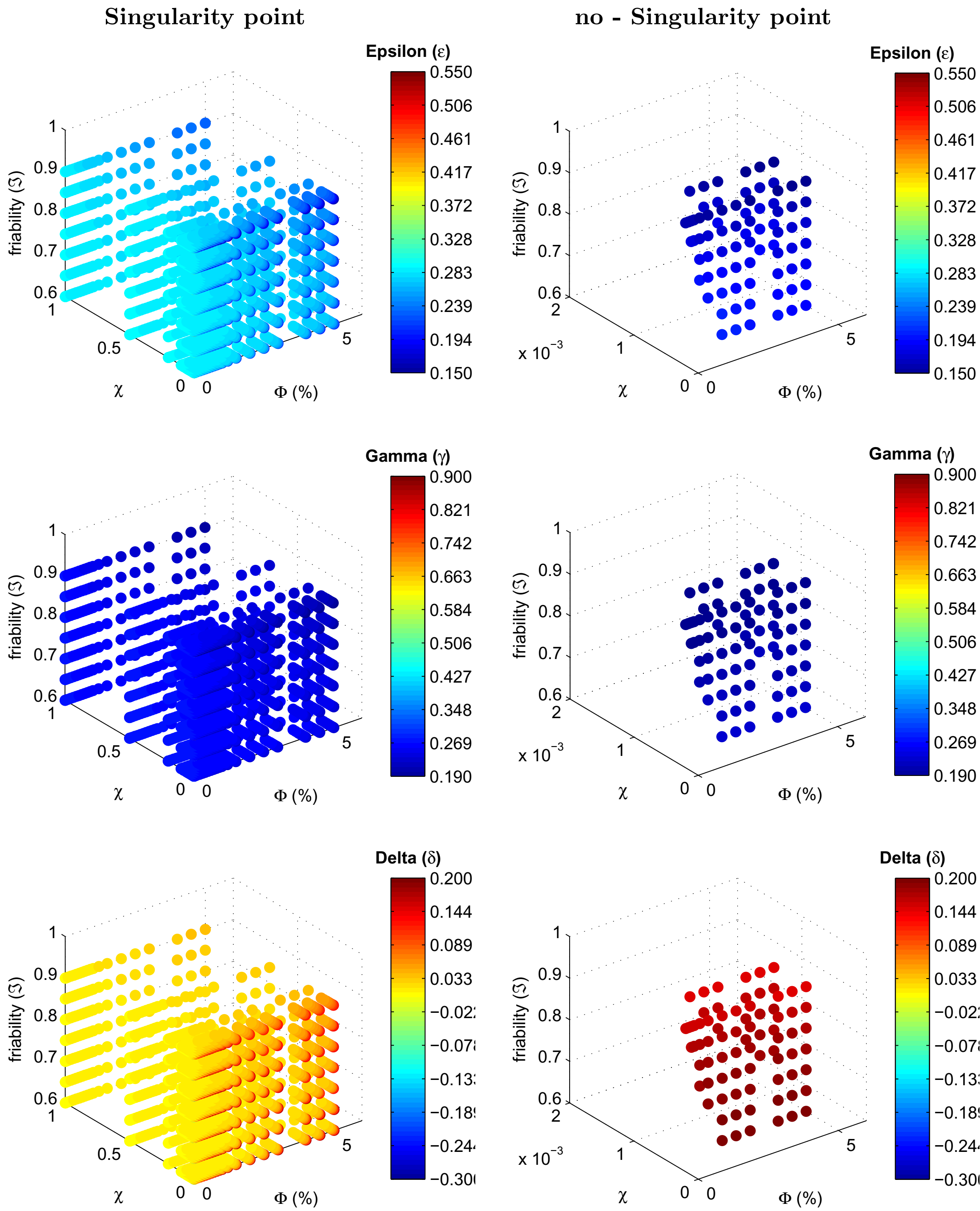

Figure 2.6: Same as Figure 2.4 but for water-filled cracks only. Left column shows only those points in which the singular value is present in their shear waves, and in right column the singular point is absent.

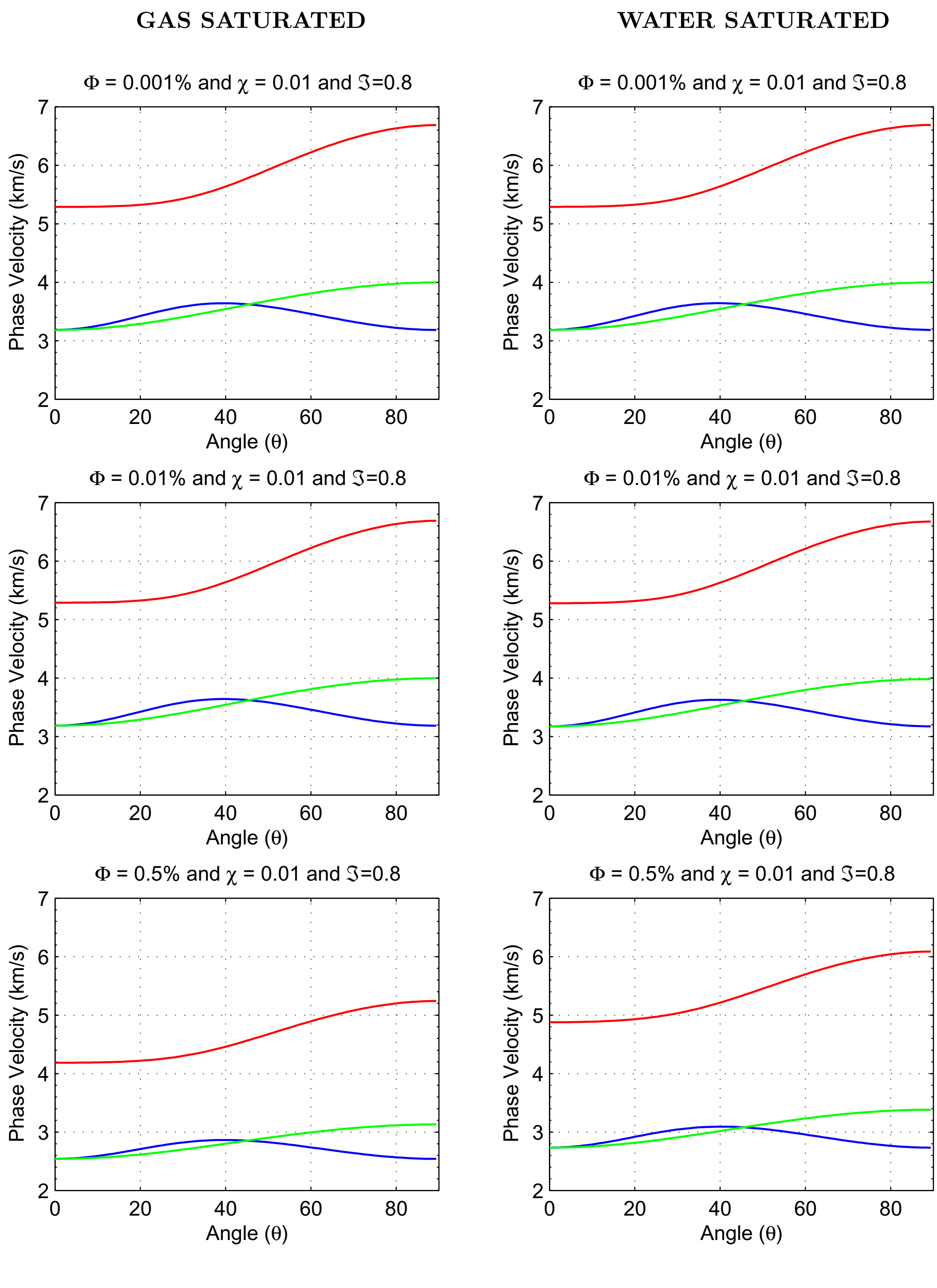

Figure 2.7: Phase velocity for three different crack-induced porosity (χ), but same aspect ratio (Φ), and friability ($\Im$) in model-I, where randomly distributed cracks are embedded in VTI matrix. The singular value ($V_{S1} = V_{S2}$) is observed (when V_{S1} crosses V_{S2})for both gas-filled and water-filled cracks. The color red = V_p , blue = V_{S1} and green = V_{S2}.

2.9.2 Shale Model-II

In model-II (Figure 2.1) the horizontally-aligned cracks are imbedded in the matrix of randomly oriented minerals resulting in an isotropic effective stiffness matrix. The main purpose of studying this model is to examine the effect of oriented fractures on velocity anisotropy, and to isolate the effect of fracture-induced anisotropy from mineral-alignment-induced anisotropy studied in model-I. This model is studied for the same values of aspect ratio χ, friability factors $\Im$, and crack-induced porosities Φ mentioned in Table 2.2. Figure 2.8 and 2.9 show color coded by the Thomsen's parameters (ε, γ, and δ), for each combination of aspect ratio, friability factors, and cracks induced porosities for gas-filled and water-filled cracks.

Figures 2.8 and 2.9 show that when the gas-filled cracks are embedded in an isotropic matrix, no singular value in shear waves exists for most of the combinations of χ, $\Im$ and Φ. However, there are few combinations that show singular value in the shear waves. Likewise, when the cracks are water-filled, most of the combinations of χ, $\Im$ and Φ show singular value in shear wave phase velocity, with few exceptions. Figure 2.7 shows that for the critical value of the aspect ratio for gas-filled cracks and water-filled cracks are 0.5 and 0.2, respectively, in order to keep the Thomsen's parameters less than unity. Furthermore, fewer combinations are possible in gas-filled cracks than in water-filled cracks for which the model provides realistic anisotropy parameters (Figure 2.8). The combinations for which shear waves show singular value in gas-filled cracks and no-singular value in water-filled cracks, are having high crack density value. These combinations are physically not possible in realistic shale models (Schoenberg and Douma, 1988; Crampin, 1994).

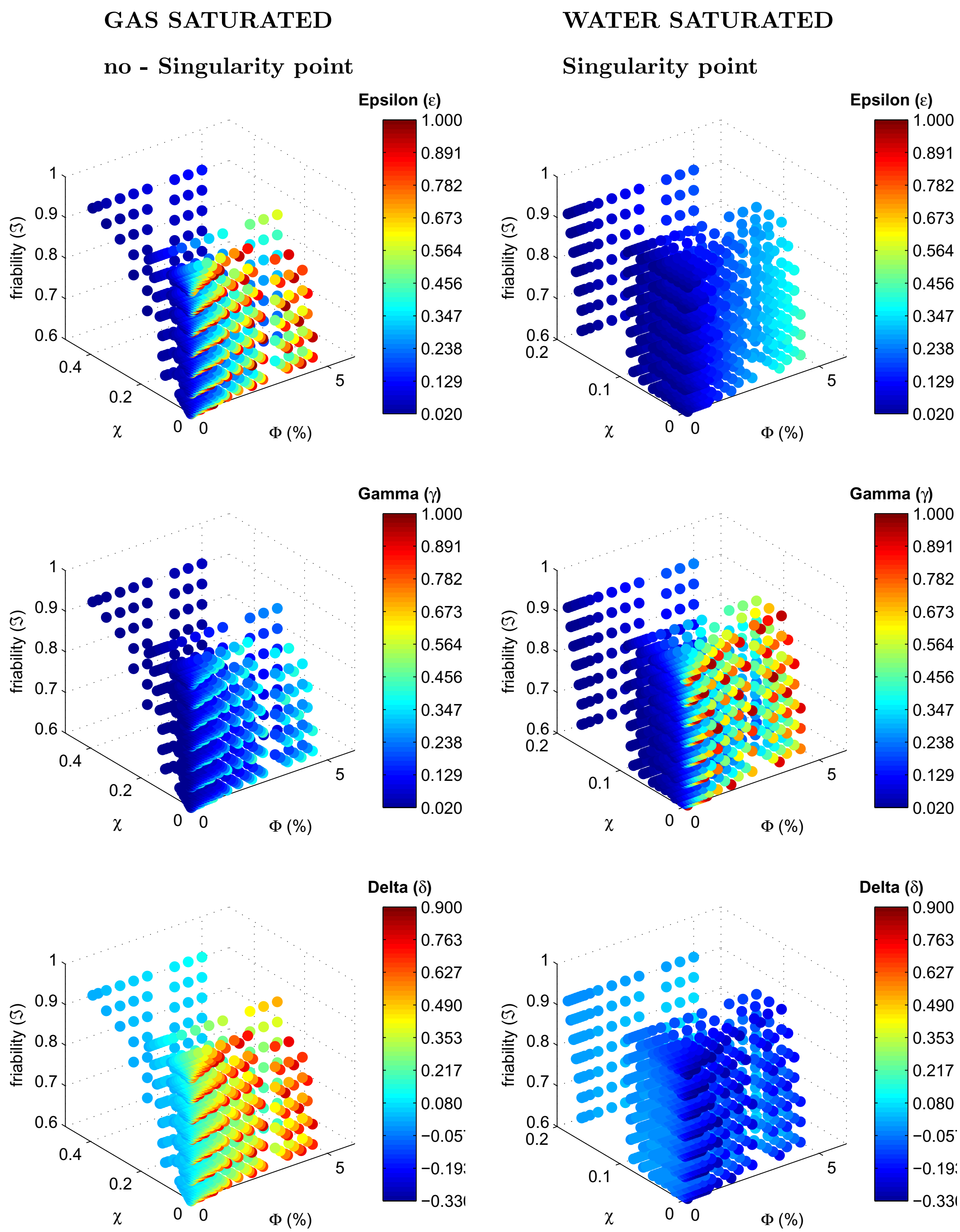

Figure 2.8: Same as Figure 2.4. but the left column shows gas-filled cracks in isotropic matric having no-singular value in their shear waves. The right column shows water-filled cracks in isotropic matrix having singular value in their shear waves.

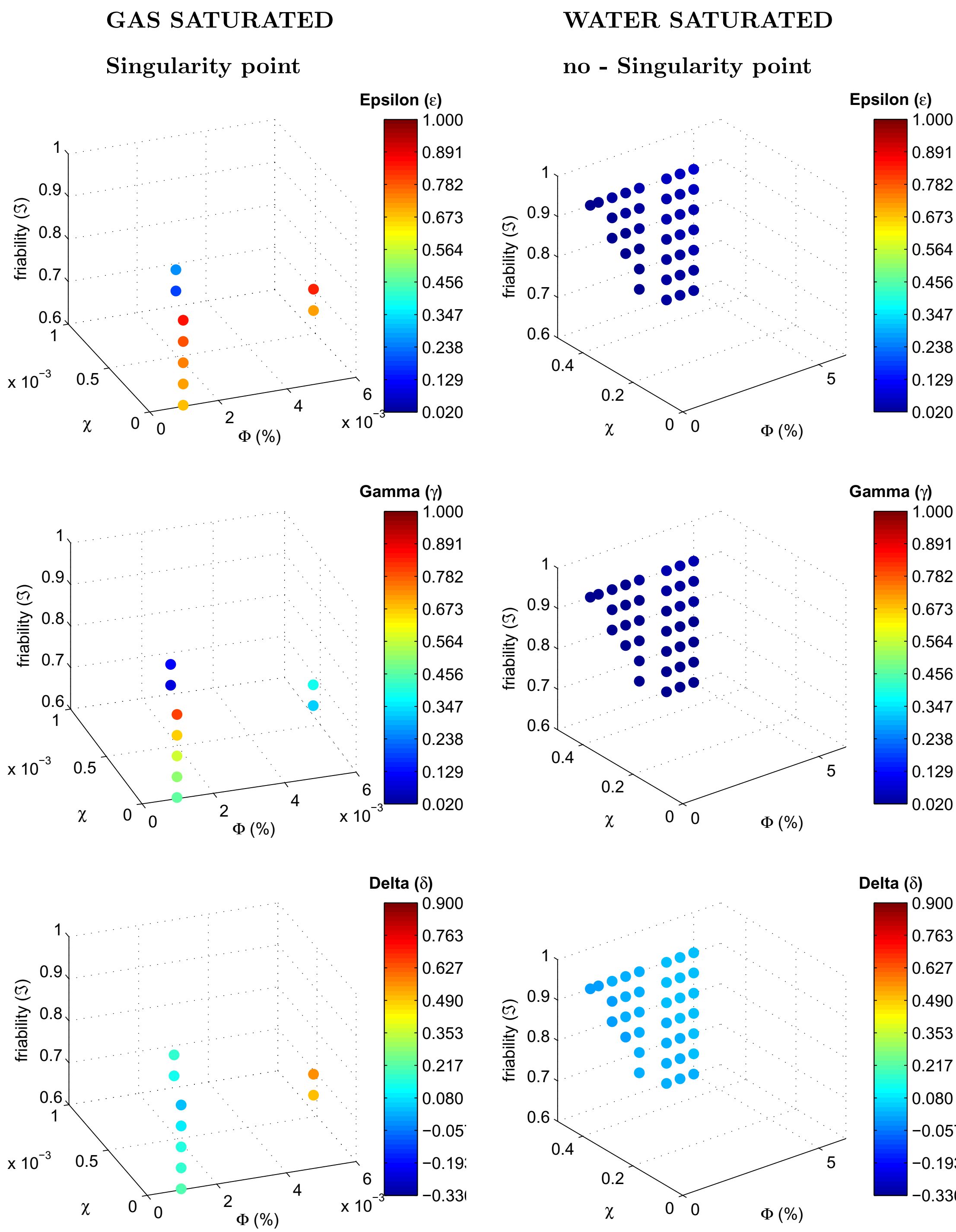

Figure 2.9: Same as Figure 2.4 but the left column shows gas-filled cracks in isotropic matric having singular value in their shear waves. The right column shows water-filled cracks in isotropic matrix having no-singular value in their shear waves.

It can be argued that if the aligned cracks are the cause of anisotropy, the distinction between gas-filled and water-filled cracks seems to exist. The singular value in shear waves is absent in the gas-filled cracks, and present in the water-filled cracks (Figure 2.10). The behavior of P-wave velocity is also different in gas-filled and water-filled cracks. The velocity of P-wave continuously increases in gas-filled cracks, but in the case of water-filled cracks such behavior does not exist. The P-wave phase velocity attains the minimum value at the same angle where qS_v becomes the maximum for the water-filled cracks embedded in isotropic matrix (Figure 2.9). This behavior of P-wave and shear waves is also observed in experimental results obtained by Vernik and Liu (1997). The characteristic of P-wave that it attains minimum value in between 0^0 and 90^0 is remarkably different than the observations in model-I and model-III, where the P-wave minimum velocity is observed along normal to the bedding plane (Figure 2.10).

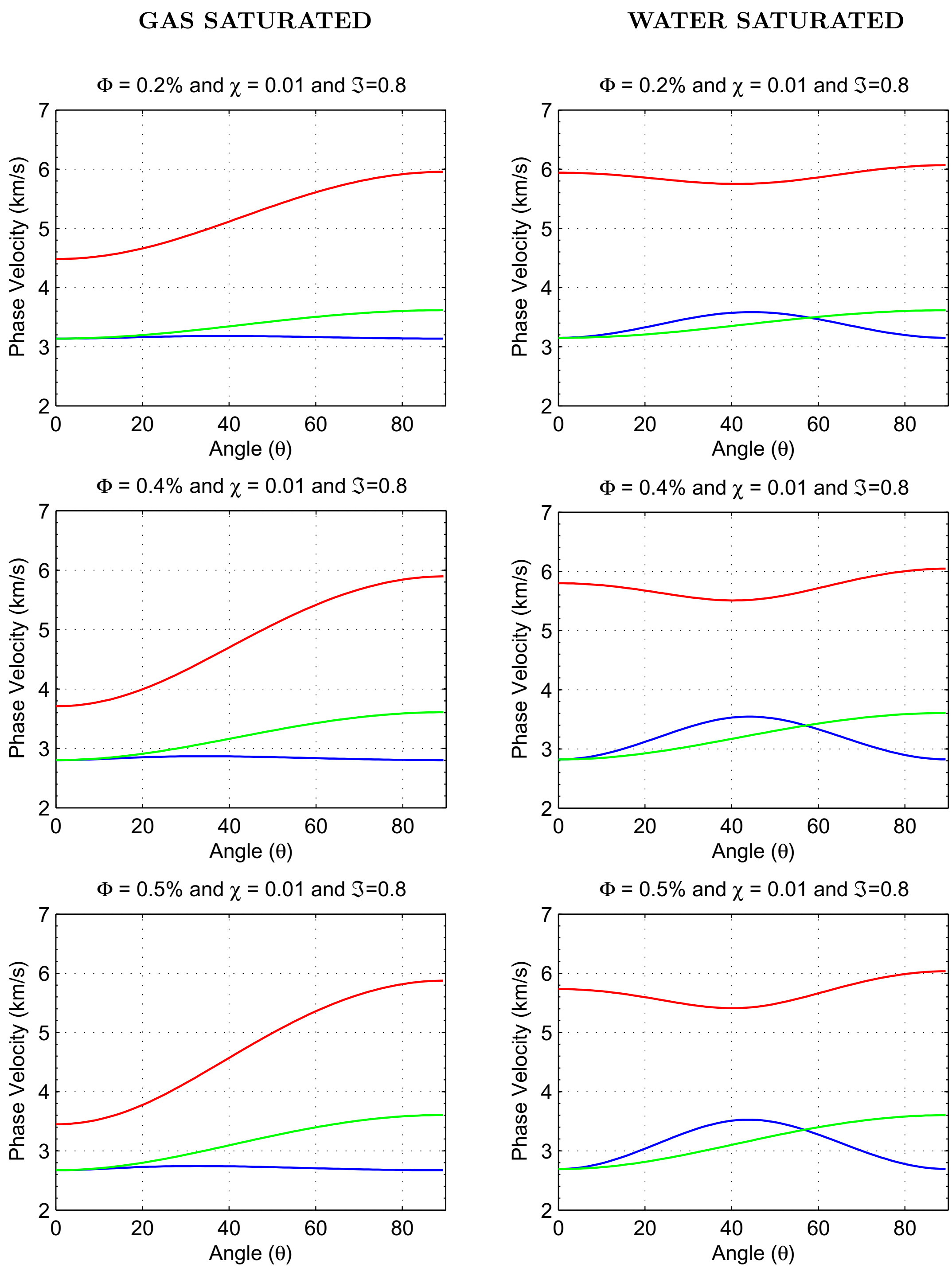

Figure 2.10: Phase velocity for three different crack-induced porosity (χ), but same aspect ratio (Φ), and friability ($\Im$) as in model-I, where aligned cracks are embedded in isotropic matrix. The singular value ($V_{S1} = V_{S2}$) is absent when the cracks are gas-filled, but present in water-filled cracks. The color red = V_p , blue = V_{S1} and green = V_{S2}.

2.9.3 Shale Model-III

In model-III (Figure 2.1) cracks are aligned in the same horizontal plane as the clay minerals. The resultant effective medium exhibits transversely isotropic symmetry with vertical axis, as was the case in model-I and model-II. The only difference in this model is that the anisotropy is contributed by both the clay mineral alignment and the alignment of the cracks because both are aligned in the same direction. Therefore, the resultant anisotropy in this case will be comparatively bigger than the anisotropy obtained for the model-I and model-II. This model is also analyzed for the same value of crack induced porosities, aspect ratio, and friability factors. So far, in all the models it is assumed that the whole volume of the clay minerals are aligned in the same direction which may not be geologically possible in every depositional environment, such as shallow marine environment where due to burrowing, the preferential alignments are disturbed (O'Brian and Slatt, 1990). In such environment only a part of clay minerals are preferentially aligned and rest are randomly distributed. This case will be studied in detail in Chapter-3 where only a proportion of the clay minerals will be aligned, with rest being randomly distributed.

When the cracks are gas-filled then for the high porosity and small aspect ratio of the crack, the effective elasticity constants give too large value of anisotropy due to strong contrast between matrix and gas-filled inclusions. But when the cracks are water-filled and the contrast is not so high then even a high porosity and small aspect ratio gives the effective elastic constant with anisotropy being in realistic range (Figure 2.11). In this model for all acceptable value of χ, $\Im$, and Φ, model

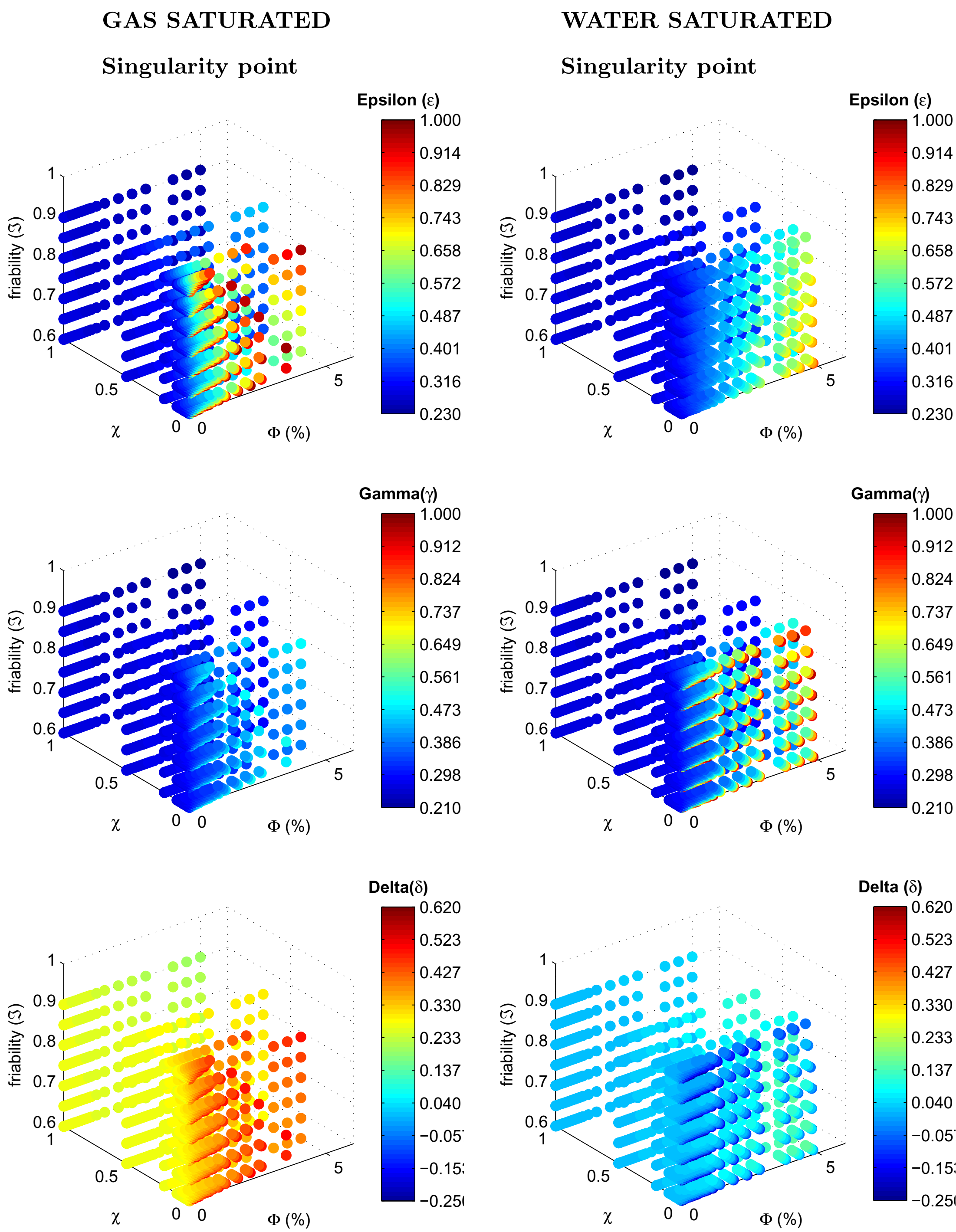

Figure 2.11: Same as Figure 2.4. but the left column shows gas-filled cracks and right column shows water-filled cracks embedded in VTI host matrix. In both cases each combinations of χ, $\Im$, and Φ shows singular value in shear waves velocity.

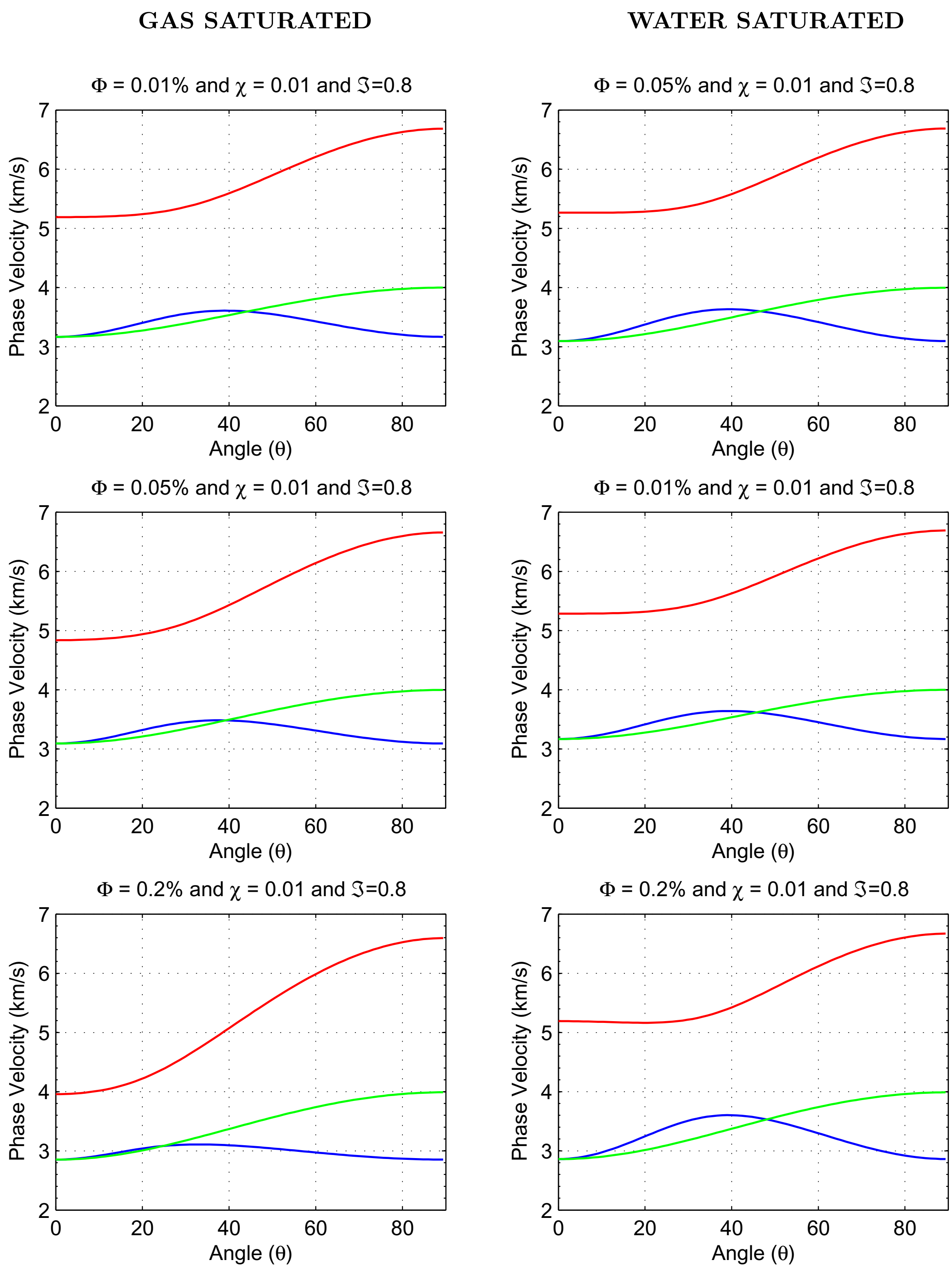

Figure 2.12: Phase velocity for three different values of crack-induced porosity (χ), but for same aspect ratio (Φ), and friability ($\Im$) as in model-I, where aligned cracks are embedded in the same direction as the clay mienrals. The singular value ($V_{S1} = V_{S2}$) appears in both cases when the cracks are gas-filled as well as water-filled. The color red = V_p , blue = V_{S1} and green = V_{S2}. The color red = V_p , blue = V_{S1} and green = V_{S2}.

shows singular value in shear waves for both cracks filled with gas and water, embedded in strong VTI matrix as considered in this case (Figure 2.12). The phase velocity plot for three different values of cracks induced porosity suggest that as the amount of crack-induced porosity increases, the angle at which shear waves attain singular value decreases in gas-filled cracks. This trend does not exist in the case of water-filled cracks. It leads to a conclusion that if the clay minerals concentration in a rock is large, as considered in this case, and have the same orientation, then the behavior of the phase velocity will be similar and singular value in shear waves will be observed in both gas-filled and water-filled crack. Since a part of anisotropy in this model is also contributed by the clay mineral alignment, the results for the gas-filled cracks confirm the experimental results obtained by Johnston and Christensen (1994).

2.9.4 Shale Model-IV

In model-IV (Figure 2.1) both clay minerals and cracks are aligned but orthogonal to each other. If the anisotropy due to clay minerals alignment in horizontal plane and due to cracks alignment in the vertical plane are equal, then the effective symmetry for this arrangement will behave as cubic (Grechka, personal communication). Since the anisotropy exhibited by clay minerals and cracks's alignment are not equal to each other, therefore the resultant effective symmetry of the system becomes orthorhombic. The presence of the vertical cracks, open or sealed, in shale is reported in many papers (Singh and Slatt, 2006; Gale et al., 2007). Recently, Gale et al. (2007) observed that most of the fractures in the Barnett Shale are calcite-filled. This model attempts to study geological formation where vertical cracks are embedded in the host VTI matrix.

This model is analyzed for the different values of Φ, χ, and $\Im$ to check the stability of the model. It is observed that when the cracks are water-filled, all acceptable combination of Φ, χ, and $\Im$ contain singular value in shear waves in Z-X plane (Z-axis is vertical) (Figure 2.12). But in gas-filled cracks some combinations show singular value and some do not (Figure 2.14). In general, no singular value in shear waves are observed when the aspect ratio of cracks are very small (Figure 2.13). The phase velocity in ZX-, YZ- and XY-plane, for three different value of Φ, keeping χ and $\Im$ constant, are shown in Figure 2.15, 2.16 and 2.17. It can be notice that in XY-plane the P-wave anisotropy in gas-filled cracks are much greater than that of water-filled cracks (Figure 2.17). This contrast is not very obvious in ZX- and YZ planes. The singularity point in the gas-filled cracks are maintained for Φ =0.05% and 0.1%. But it can be noticed that when the value of Φ increases from 0.1% to 0.5%, the singularity point in gas-filled cracks disappear, while it always appears in water-filled cracks (Figure 2.15). In this model it is also noticed that each of the Thomsen's parameters (ϵ, γ and δ) can take positive or negative value which is quite different than the rest of the three models discussed before, where only delta is seen to be negative as well as positive (Table 2.4).

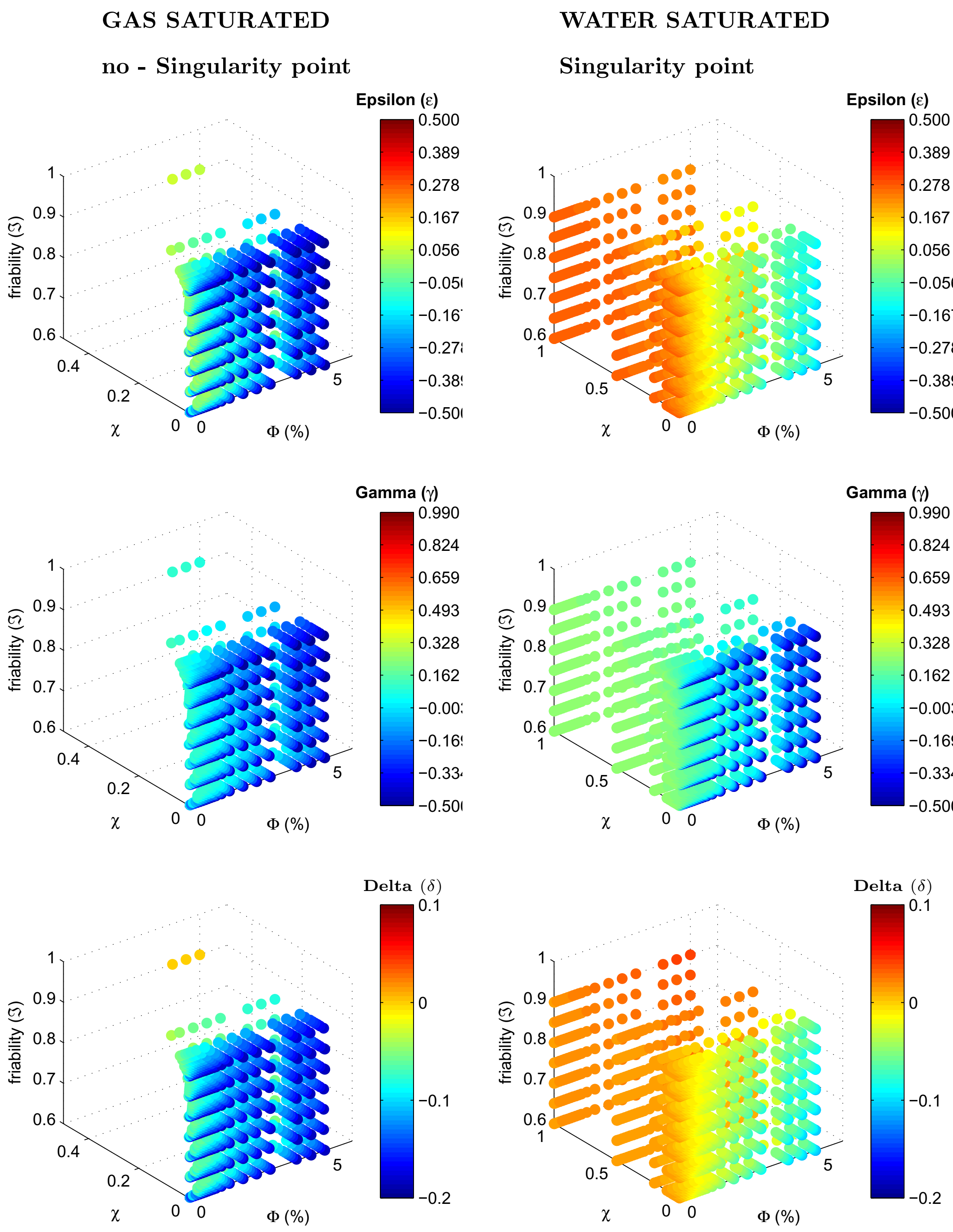

Figure 2.13: Same as Figure 2.4 but the left column shows gas-filled cracks having no singular value, and right column shows water-filled cracks having singular value in shear waves, where the cracks are embedded parallel to the axis of VTI host matrix, measured in ZX-plane.

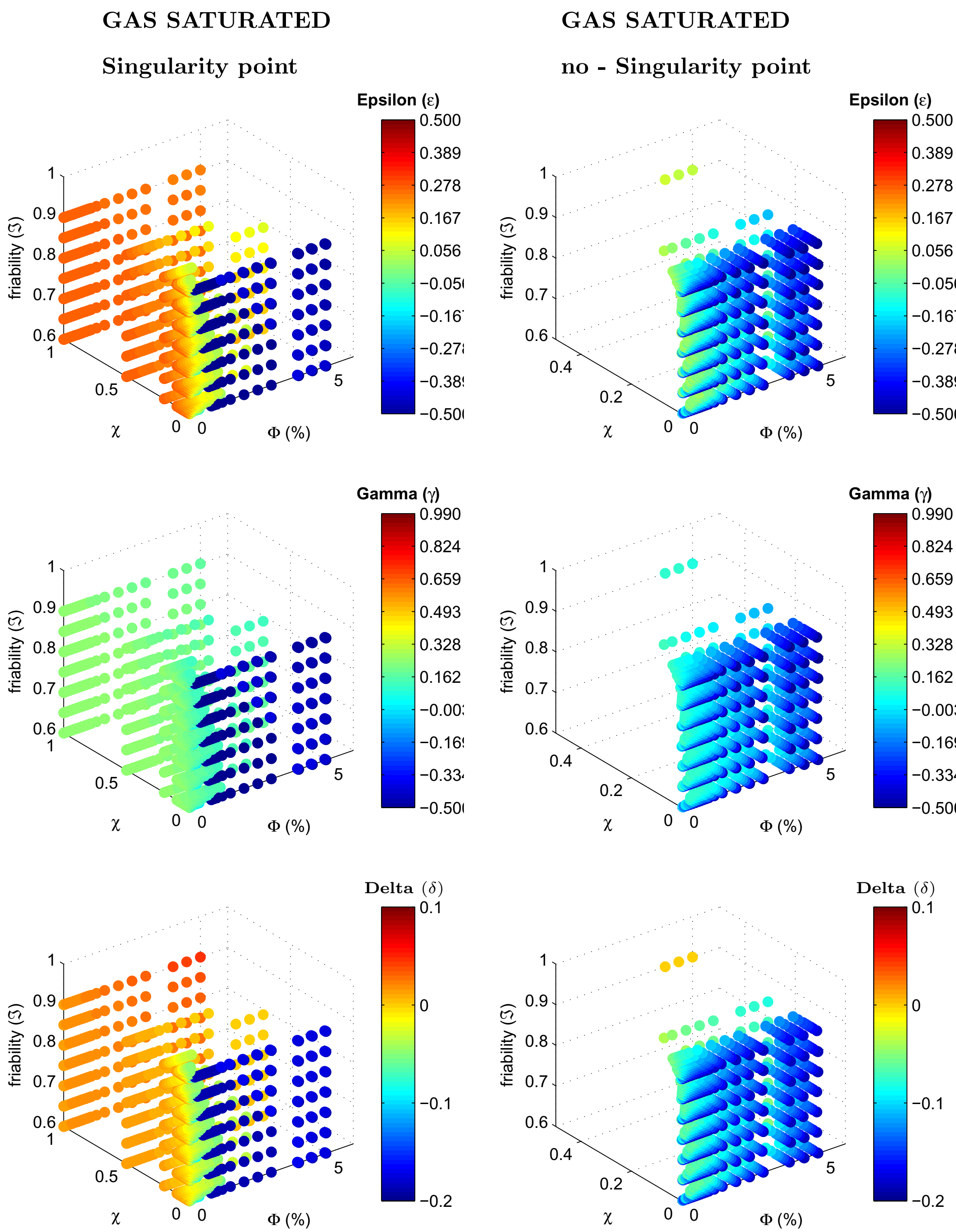

Figure 2.14: Same as Figure 2.4 but the left column shows gas-filled cracks having singular value, and right column also shows gas-filled cracks but having singular value in in shear waves, where the cracks are embedded parallel to the axis in axis of VTI host matrix, measured in ZX-plane.

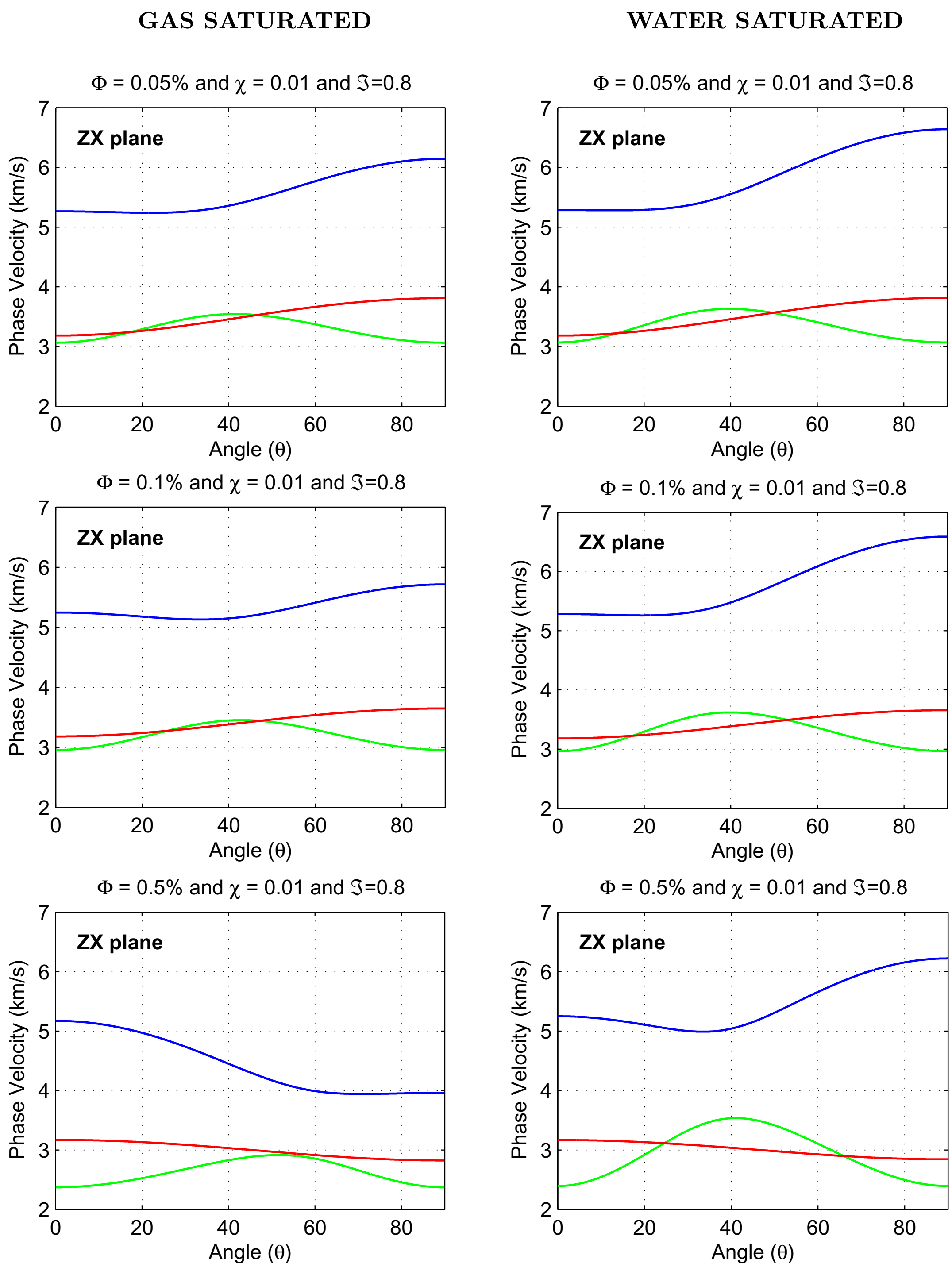

Figure 2.15: Phase velocity for three different cracks induced porosity ($\chi = 0.05\%$, 0.1% and 0.5%), but for the same aspect ratio (Φ), and friability ($\Im$) in ZX-plane. The color red = V_p , blue = V_{S1} and green = V_{S2}.

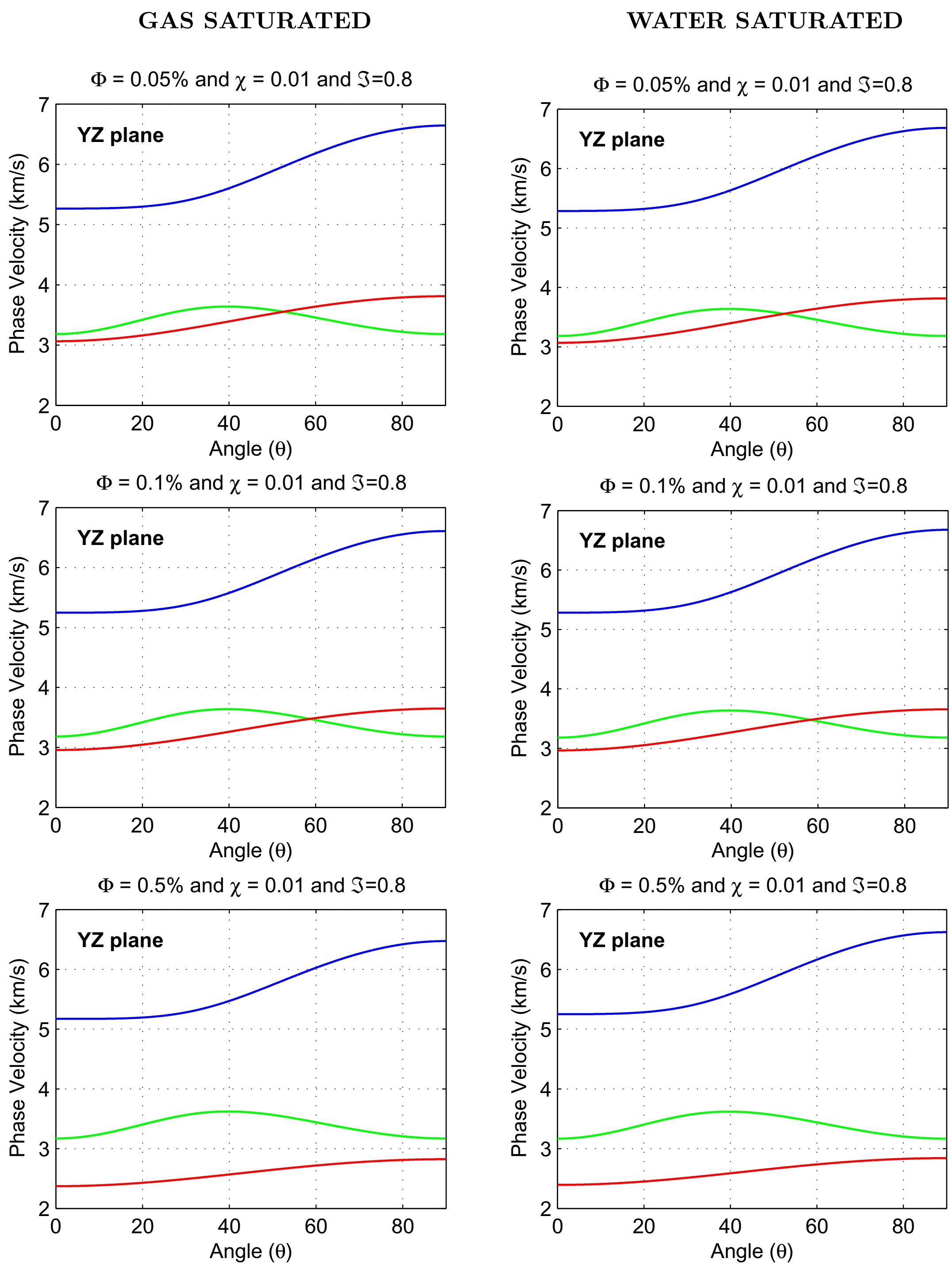

Figure 2.16: Phase velocity for three different cracks induced porosity ($\chi = 0.05\%$, 0.1% and 0.5%), but for the same aspect ratio (Φ), and friability ($\Im$) in YZ-plane. The color red = V_p , blue = V_{S1} and green = V_{S2}.

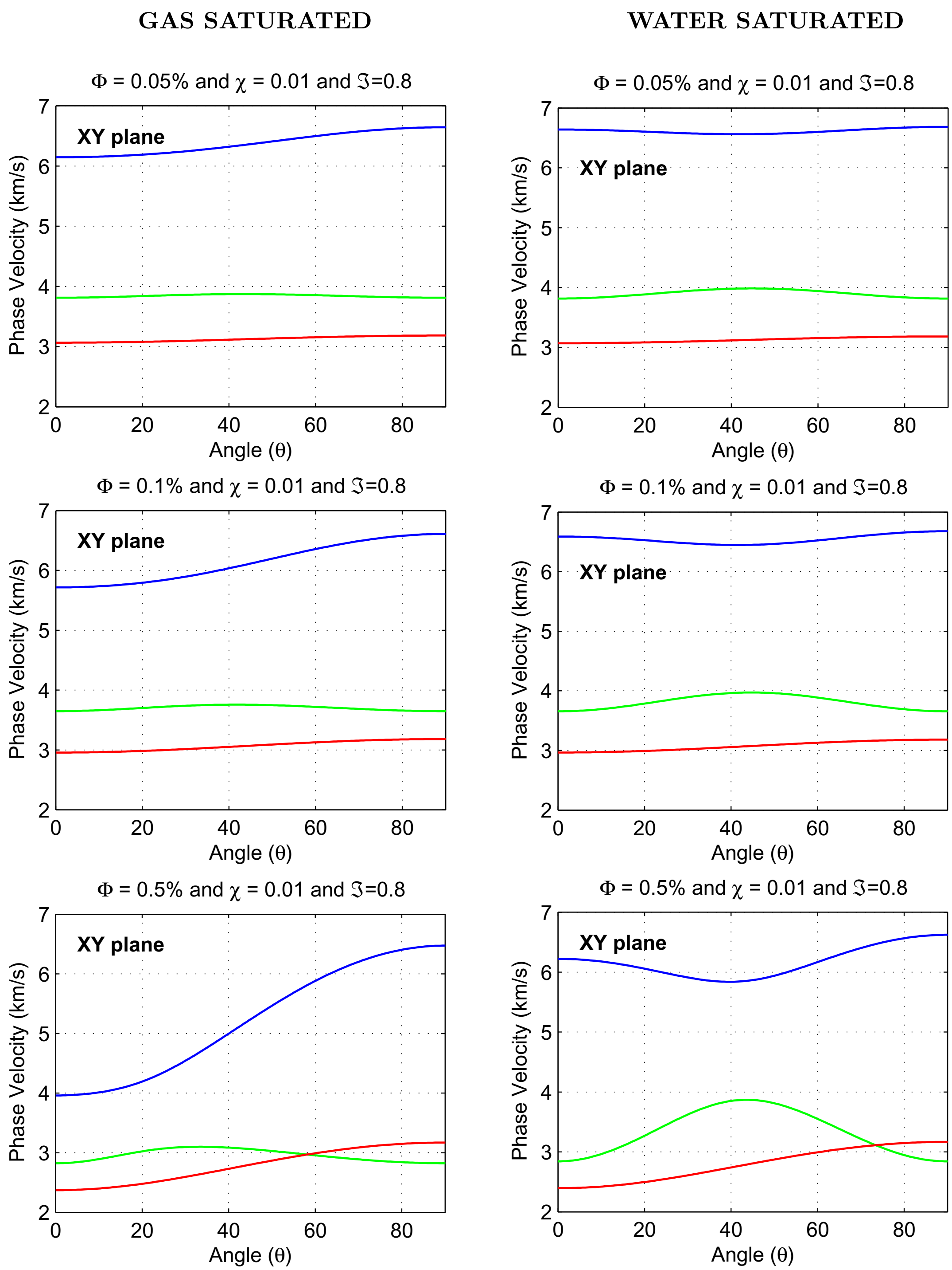

Figure 2.17: Phase velocity for three different cracks induced porosity ($\chi = 0.05\%$, 0.1% and 0.5%), but for the same aspect ratio (Φ), and friability ($\Im$) in XY-plane. The color red = V_p , blue = V_{S1} and green = V_{S2}.

2.10 Discussion Of the Thomsen's Parameters in Shale

A transversely isotropic medium is completely characterized by five independent elastic constants. Thomsen (1986) suggested that in weakly anisotropic medium three parameters (ϵ, γ, and δ), aka Thomsen's parameters, and P- and S-wave velocity along the axis of symmetry are sufficient to explain a transversely isotropic (TI) medium. Tsvankin (1997) calculated the Thomsen's parameters for orthorhombic media. The first three models studied in this chapter are effectively TI medium with vertical axis of symmetry, and the fourth model shows effectively orthorhombic symmetry. Al-Khalifah and Tsvankin (1995) outlined the importance of δ in the calculation of NMO velocity and angle dependent reflectivity. According to Thomsen (1986) the only anisotropy parameter needed to explain the difference between the small-offset NMO (normal moveout) velocity and vertical velocity, and help to interpret the small-offset AVO (amplitude variation with offset)response, is delta (δ). δ, probably the most important anisotropy parameter, can take both positive and negative value in TI and orthorhombic media.

Sayers (2005), by crossplotting ϵ, γ, and δ (data compiled from various published literature), shows that ϵ and γ are always positive, but δ can take negative as well as positive value. Sayers data collection is only for effectively VTI symmetry (confirmed by personal discussion), and his cross-plots do not have data from effectively orthorhombic symmetric medium. The Thomsen's parameters obtained for the four models are summarized in Table 2.4 for gas- and water-filled cracks embedded in

Table 2.4: Range of Thomsen's parameters for the four models analyzed. Note that ϵ and γ are positive for all range of Φ, χ, and $\Im$ when the resulting effective medium is VTI, but they can be negative if the resulting effective media is orthorhombic. C.O. = crack orientation.

MODEL-I:	**Host Matrix - VTI**,		**C.O. - Random**	
Thomsen's parameters range	*Gas-filled*		*Water-filled*	
	singular	**no-singular**	**singular**	**no-singular**
	Min-Max	Min-Max	Min-Max	Min-Max
ε	0.25 - 0.47		0.17 - 0.50	0.15 - 0.21
γ	0.19 - 0.80		0.19 - 0.95	0.19 - 0.24
δ	-0.27 - 0.06		0.20 - 0.25	0.15 - 0.20
MODEL-II:	**Host Matrix - Isotropic**,		**C.O. - Horizontal**	
ε	0.21 - 0.87	0.03 - 0.99	0.02 - 0.47	0.02 - 0.09
γ	0.10 - 0.82	0.02 - 0.43	0.02 - 0.99	0.02 - 0.07
δ		0.03 - 0.81	-0.33 - 0.11	
MODEL-III:	**Host Matrix - VTI**,		**C.O. - Horizontal**	
ε	0.25 - 1.00		0.23 - 0.84	
γ	0.21 - 0.52		0.21 - 1.00	
δ	0.02 - 0.62		-0.25 - 0.16	
MODEL-IV:	**Host Matrix - VTI**,		**C.O. - Vertical**	
ε	-0.49 - 0.49	-0.49 - 0.09	-0.19 - 0.30	
γ	-0.49 - 0.98	-0.49 - 0.16	-0.49 - 0.79	
δ	-0.18 - 0.08	-0.18 - 0.004	-0.11 - 0.05	

either isotropic or TI medium. The first three models studied are effectively TI medium with a vertical axis of symmetry and the fourth model attains orthorhombic symmetry because the vertical cracks are embedded in a TI medium. It is evident that, when the resultant effective media is VTI (models I, II, and III), ϵ and γ are positive, irrespective of the saturation properties of cracks. Also, it is observed that when the host matrix is isotropic, the δ in gas-filled cracks is always positive for all realistic values of crack-induced porosity, and mostly negative in water-filled cracks. The experimental results of Vernik and Liu (1997), whose are shown in Figure 2.18.

Vernik and Liu (1997), show that when dry cracks are embedded in isotropic matrix, δ and ϵ are positive (data points for crack-induced and dry samples are highlighted by red circles). But when the cracks are wet, δ becomes negative even though ϵ remains positive (data point for crack-induced and wet samples are highlighted by magenta circles). It is assumed that at a pressure of 70 MPa all the cracks are closed; and, hence, the anisotropy of shale is only due to clay mineral alignment (intrinsic anisotropy). This laboratory set-up simulates

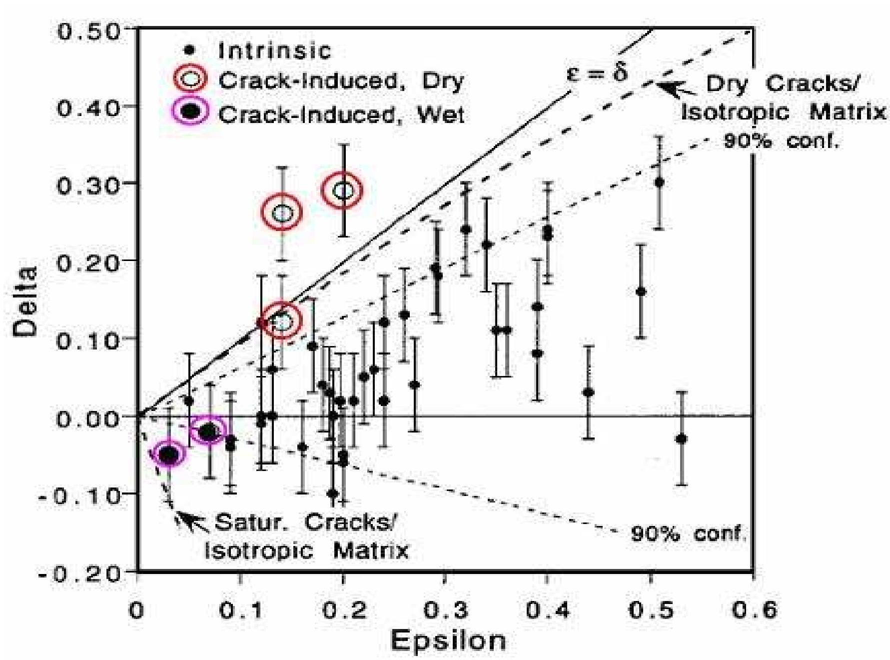

Figure 2.18: Cross-plot of anisotropy parameters ϵ versus δ showing the effect of clay minerals alignment and aligned cracks on anisotropy. Data are collected from 5 samples of black shale measured at the high pressure (70 MPa) so that all cracks are closed to measure the intrinsic anisotropy. These samples were also measured at a low confining pressure to estimate the effect of crack induced anisotropy after subtracting the effect of intrinsic anisotropy. Prediction of dry and fluid-filled cracks (big dashed line) are also shown using Hudson (1981) model. Modified from Vernik and Liu (1997).

model-I, in which the anisotropy is due to clay mineral alignment. The laboratory data of Vernik and Liu (1997) show that δ can be negative or positive when the anisotropy is due to clay mineral alignment only. The model-I results show the same behavior of δ as observed from laboratory data. When the resulting medium is orthorhombic (model IV), the value of ϵ and γ can be either positive or negative. Although, not so systematic in δ, which positive and negative, is observed for all the four models. As discussed before the negative value of ϵ and δ has never been reported in the literature to my understanding.

2.11 Summary

Four different models of shale used to study the effect of crack-induced anisotropy in the presence and absence of intrinsic shale anisotropy indicate that the anisotropy of shale with water-filled cracks generally shows the same character as observed in the case when the anisotropy is only due to matrix anisotropy, i.e., clay mineral alignments. If the cracks are distributed randomly or aligned in the anisotropic host matrix in such a way that the resultant medium is effectively transversely isotropic, the trend observed in the phase velocity of P-wave and shear waves is similar. But if the background matrix is isotropic, this trend is completely different. The significance of this is that if the host matrix has VTI symmetry, it would be difficult to distinguish randomly oriented cracks from aligned cracks because the behavior of phase velocity in both cases looks the same. But if the cracks are aligned in an isotropic host matrix the identification becomes possible because P-wave velocity attains a minimum value at an angle that corresponds to the maximum velocity of qS_v. Also, in model-I and model-III the singular value in shear waves is observed for all realistic values of porosity, aspect ratio, and friability, and hence, the distinction whether the cracks are gas-filled or water-filled does not, in fact, exist. However, there is a definite distinction between the gas-filled and the water-filled case in model-II where the singular value is only observed in water-filled cracks. The characteristic of P-wave in model-II, that it attains minimum value in between 0^0 and 90^0, is remarkably different than model-I and model-III where P-wave minimum velocity is observed along the normal to the bedding plane. In model-I and model-III, to distinguish whether the anisotropy is intrinsic, or due to water-filled cracks we should have additional information, such as electrical conductivity which would show a higher value in the presence of water.

P-wave and V_{sh} velocities measured in gas-filled shale show an increase in P-wave velocity from 0^0 to 90^0 (0^0 being normal to the bedding plane). It is also found in our modeling that when anisotropy is due to clay mineral alignment, the rate of increase in V_p and V_{sh} will be greatest between 20^0 and 70^0 which is also concluded by Johnston and Christensen (1994) from their experimental data. Johnston and Christensen (1994) reported that in dry shale the qS_v shows maximum velocity approximately between 30^0 to 45^0 from bedding normal which seem to be evident from the modeling results obtained for gas-filled cracks in model-I, and also in model-III when the crack-induced porosity is smaller. But when the crack-induced anisotropy adds up to the mineral aligned anisotropy, then the peak value in qS_v moves towards the symmetry axis.

The results illustrate that the presence of gas-filled porosity significantly modifies the anisotropy of the shale, but the behavior of the shear waves anisotropy in water-filled porosity is similar to the case in which clay minerals are aligned. The Thomsen's parameters ϵ and γ are positive if the resulting effective medium is TI, but if the resulting effective medium is orthorhombic then ϵ and γ can be positive or negative. The negative valuess of ϵ or γ directly characterize the presence of orthorhombic symmetry, or, alternatively, it indicates the presence of vertical cracks in a VTI medium.

Chapter 3

The Effect of Minerals Alignment, Aspect-ratio and Friability on Anisotropy in Shale

In the previous chapter four different models of shale were considered to understand and characterize the anisotropy of shale quantitatively. In Chapter 2, model-II and model-III represent the two end members of the clay mineral distribution: all the clay minerals are randomly distributed (model-II) and all the clay minerals are aligned (model-III). It leaves a gap in the modeling of shale considered in Chapter 2, and one can ask what will happen if just a fraction of the total clay minerals are aligned? In order to bridge the gap that exist in the model-II and model-III, several models are considered in which a proportion, starting with 5%, of the total clay minerals (63%) are considered to be aligned and the rest are randomly oriented. The proportion of aligned clay mineral is increased by 5% in each subsequent model. Note that the models associated with 0% and 63% aligned clay mineral cases are the same as model-II and model-III, respectively, of the previous chapter. The phase velocities of these models are analyzed and quantitative analysis of clay mineral alignment is establish in order to observe singularity point ($V_{s1} = V_{s2}$) in the shear waves.

3.1 Introduction

The inherent cause of anisotropy in shale is the presence of platy clay minerals in an aligned fashion (Wenk et al., 2007). The alignment of clay mineral is controlled by the geological processes through which the sediments have gone through after deposition, that is diagenesis. Diagenesis covers any physical, chemical and biological changes that occur in sediments after deposition at near normal temperature and pressure and before metamorphism (Selley, 1998). The role of depositional environment on the alignment of microfabric is shown in Figure 3.1, where the regions a, b, and c, respectively, represent randomly distributed, poorly aligned and well aligned clay minerals. O'Brian and Slatt (1990) suggest that well-developed lamination is preserved in a low energy, anaerobic depositional environment where bioturbation of the sediments by benthonic organisms does not occur due to lack of oxygen. As the flow energy increases, along with increasing aerobic condition, the lamination get poorer because of the sediments mixing. The lamination of sediments is completely destroyed due to complete reworking of the sediments due to high biogenic activities (O'Brian and Slatt, 1990; Diego and Douglas, 1999).

This chapter illustrate the behavior of elastic waves when ellipsoidal cracks are introduced into isotropic and anisotropic matrices and how the shape, friability of the cracks, and crack-induced porosity affect the elastic wave propagation. It also evaluates the effect of crack alignment on the intrinsic anisotropy due to clay minerals alignment. The difference in P-wave and the shear waves velocity are analyzed for gas-filled and water-filled cracks.

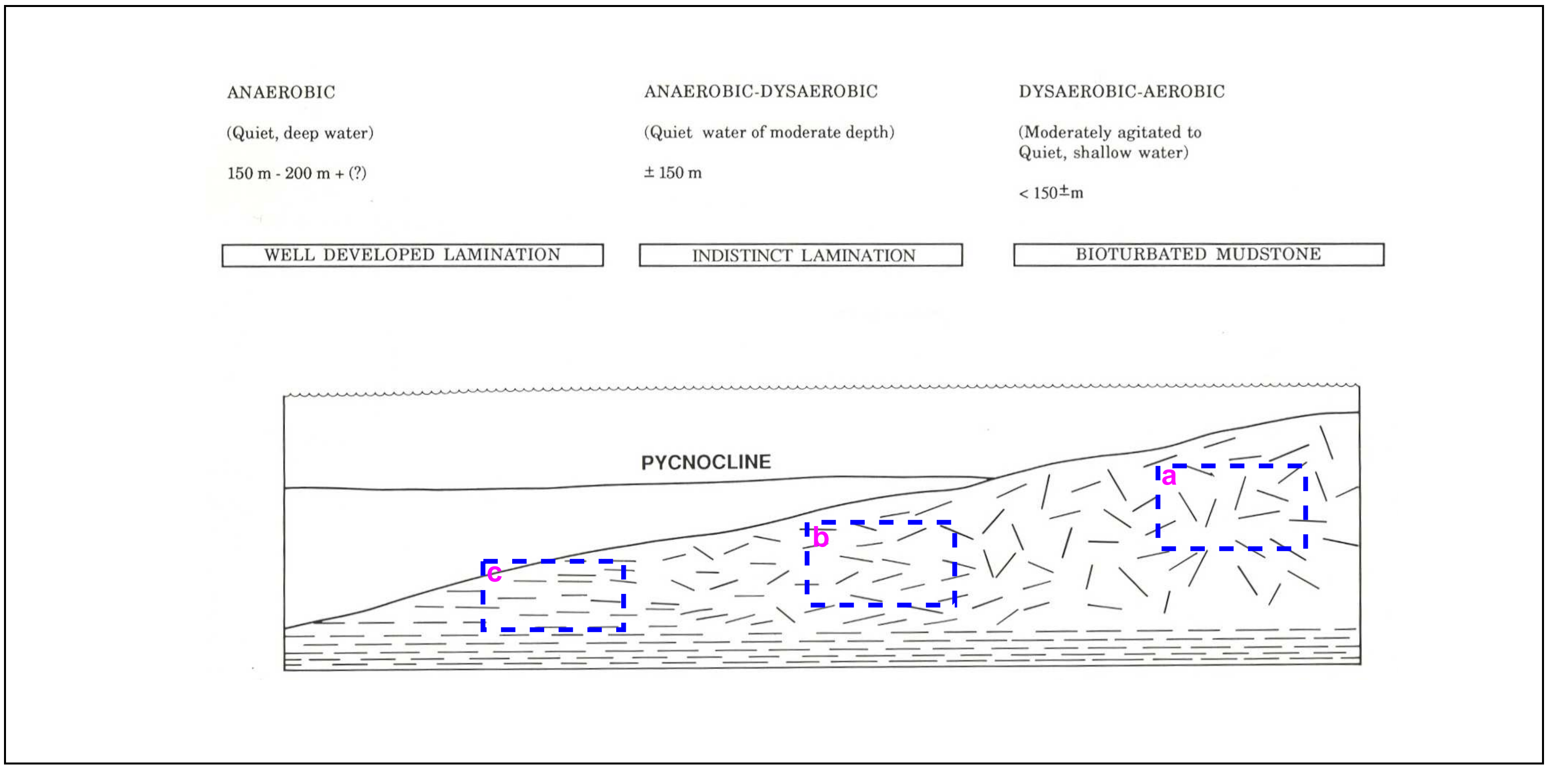

Figure 3.1: Role of sedimentary environment in development of alignment of clay minerals in shale: (a) randomly oriented microfabric, (b) poorly aligned microfabric, and (c) well aligned microfabric. Modified from O'Brian and Slatt (1990).

The mineral composition of the shale is the same as was considered in the previous chapter. This means that the volume concentration of different minerals are: clay minerals (63%), quartz (31%), albite (4%) and pyrite (2%). The clay minerals are mainly illite rich (illite = 87% and chlorite = 13%). The elastic constants of the mixture are calculated, assuming that the percentage of the clay minerals orientation is only 5%, 10%, 15%, ... 63% (Table 3.1). The clay minerals are mainly illite rich (illite = 87% and chlorite = 13%). Figure 3.2 shows the values of Thomsen's parameters for different proportions of clay mineral alignment. As the proportion of aligned clay minerals increases the anisotropy parameters, $\epsilon, \gamma, and \delta$, also increase. Isotropic elastic constants of polycrystalline aggregates of anisotropic minerals are calculated using the method in Belikov et al. (1970).

Results indicate that as the crack-induced porosity increases the P-wave and the shear waves anisotropy increases. If the host matrix is isotropic the distinction between gas-filled and water-filled cracks is indicated by a singularity point which occurs only in water-filled cracks. If the background matrix is anisotropic, the singularity point in the shear waves is observed for both gas and water-filled cracks at low values of crack-induced porosity. As the cracks stiffen the anisotropy decreases for both gas-filled and water-filled cracks, but increases with increased friability.

Table 3.1: The effective elastic constants of shale having 63% clay minerals by volume, where the percentage of aligned clay is increasing by 5% increments. When the aligned clay minerals percentage is zero, the rock exhibit isotropic properties. The anisotropic properties increases with increasing clay mineral alignment.

Clay Minerals		**Effective elastic constants** (C_{mn})				
oriented (%)	**random (%)**	C_{11}	C_{13}	C_{33}	C_{44}	C_{66}
0	63	101.19	29.53	101.19	35.83	35.83
5	58	102.85	28.98	99.21	35.18	36.45
10	53	104.51	28.42	97.24	34.53	37.06
15	48	106.17	27.87	95.27	33.89	37.68
20	43	107.84	27.32	93.30	33.24	38.30
25	38	109.50	26.77	91.32	32.59	38.92
30	33	111.16	26.21	89.35	31.94	39.53
35	28	112.83	25.66	87.38	31.30	40.15
40	23	114.49	25.11	85.41	30.65	40.77
45	18	116.15	24.56	83.44	30.00	41.39
50	13	117.81	24.00	81.46	29.35	42.00
55	8	119.48	23.45	79.49	28.71	42.60
60	3	121.14	22.90	77.52	28.06	43.24
63	0	122.14	22.57	76.34	27.67	43.61

3.2 Effect of Clay Minerals Alignment

The effect of clay mineral alignment on anisotropy will be examined in this section, keeping crack induced porosity, aspect ratio and friability constant. Also, the effect of fluid properties present in the cracks is analyzed. The experimental measurement of shale anisotropy obtained by Johnston and Christensen (1994) and Christensen and Johnston (1995) is compared with theoretical modeling results obtained in this section.

Five cases with different matrix anisotropy properties were studied. As more aligned cracks are introduced in a medium, the medium will become more anisotropic.

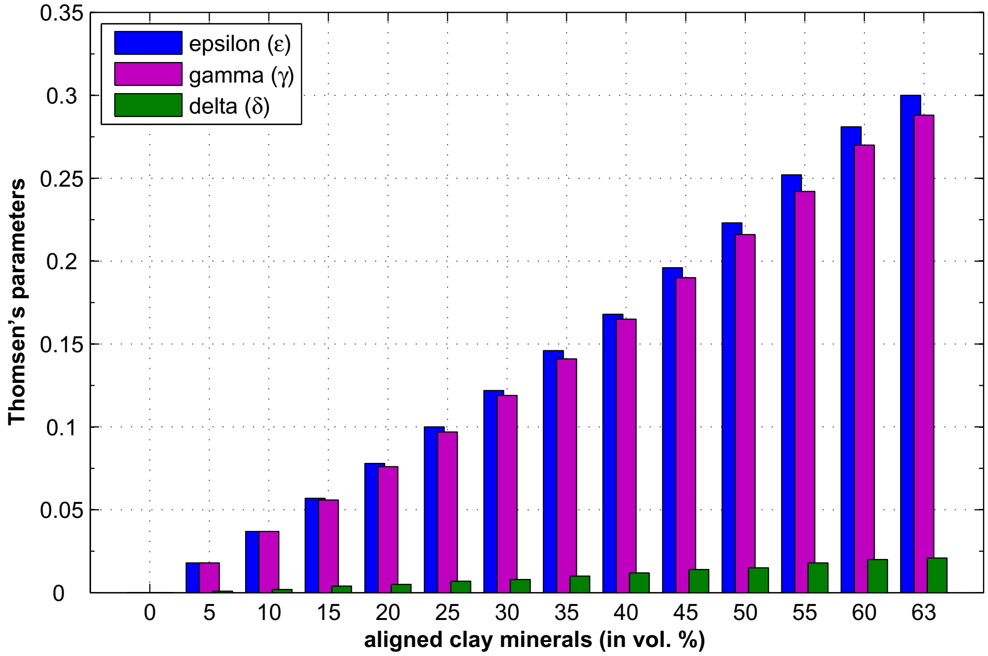

Figure 3.2: Thomsen's parameters for Table 3.1 .

Increasing the crack-induced porosity reduces the elasticity of the rocks. Wave propagation in cracked media was studied by Eshelby (1957), Hudson (1980, 1981), Bayuk and Chesnokov (1998) and Thomsen (1995) for an isotropic host matrix. However, in their study the behavior of elastic waves in cracked media when the matrix is anisotropic was not considered.

Figure 3.3 shows the behavior of elastic waves in cracked media for an isotropic host matrix with randomly oriented clay minerals and aligned cracks. The trend of P-wave and the shear waves obtained for this effective medium matches the results of Thomsen (1995) for gas-filled and water-filled case, that no singular value exists for gas-filled cracks, but does exist for water-filled cracks. This trend of elastic waves changes when the symmetry of the host matrix changes. Figures 3.4, 3.5, 3.6, and

3.7 show that an increasing proportion of aligned clay mineral, i.e, 5%, 20%, 40% and 63% produces an increase in anisotropy. If only 5% clay minerals are aligned, the resulting matrix is weakly anisotropic. At larger percentage of aligned clay minerals, the behavior of elastic waves in gas-filled cracks become very different than it is for aligned cracks in an isotropic host matrix: the singular value for the shear waves appears even in the gas-filled cracks (Figures 3.5, 3.6, and 3.7).

In general, the P-wave anisotropy increases with the increase in the concentration of aligned cracks. From all the figures it is clearly evident that the singularity point moves closer to the symmetry axis with the increases in aligned crack's concentration and clay minerals alignments. The Vp/Vs_{max} ratio increases with the increase in crack-induced porosity for water-filled cracks, but decreases for gas-filled cracks. If the matrix property is anisotropic due to clay minerals alignment then the Vp/Vs_{max} ratio is observed smaller than the isotropic matrix for the same amount of aligned crack ($\Phi = 0.1\%$) (Figure 3.3 and 3.7).

If the matrix property is isotropic then a clear distinction exist in the ratio of Vp/Vs_{max} for the gas-filled and water-filled cracks. Also, when the matrix is anisotropic then for a small amount of crack-induced porosity, the behavior of Vp/Vs_{max} in gas-filled and water-filled cracks is indistinguishable, as it is observed for the porosity = 0.001% (Figure 3.5 and 3.6) and porosity = 0.1 (Figure 3.7). The amount of porosity needed to make this behavior indistinguishable depends on the matrix property. If the matrix is strongly anisotropic, more aligned porosity is required.

The experimental results of Johnston and Christensen (1994), where the anisotropy is only due to clay mineral alignment (since the measurement was at 100 MPa) show

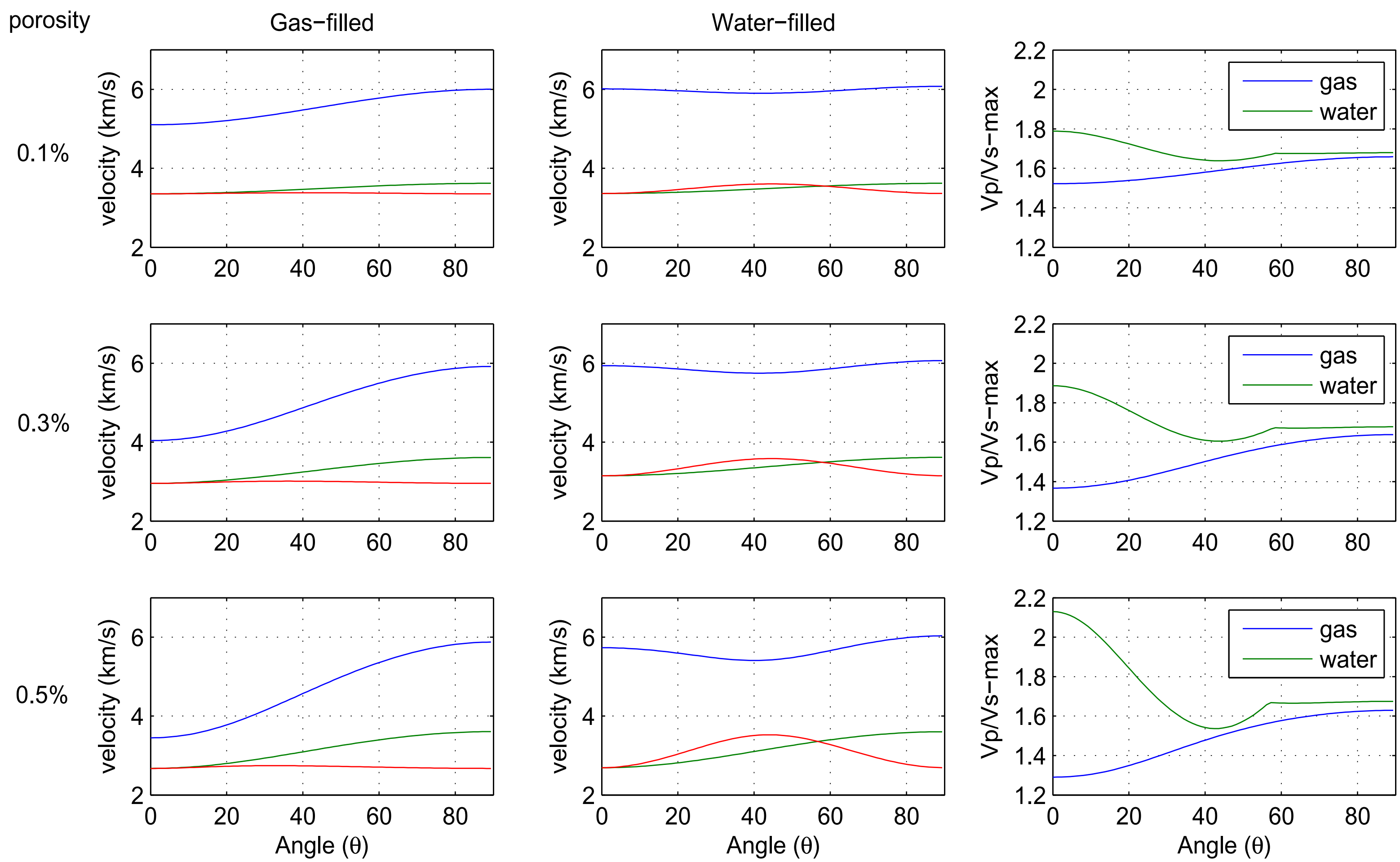

Figure 3.3: Clay minerals are randomly aligned. Anisotropy is exhibited only due to aligned cracks. The aspect ratio of the cracks and the friability factor are 0.01 and 0.8 respectively. The color coded velocity Vp - blue, Vs_1 - green and Vs_2 - red (for two leftmost columns). The singularity point is absent in gas-filled cracks and present in water-filled cracks. The kinks in the $Vp/Vs-max$ for water-filled cracks coincide with the singularity points. The kinks are evidently absent in gas-filled cracks.

singularity point in shear wave velocities. The particular behavior is observed in this study for very small values of crack-induced porosity and the anisotropy is primarily due to clay minerals alignment. This observation suggests that even at 100 MPa a small amount of the cracks were open. Though this character dies off when crack induced anisotropy increases (Figure 3.5, 3.6, 3.7). The volume fraction of the aligned clay minerals needed to produce a singularity point in the shear waves is greater than 0.1 (Figure 3.5).

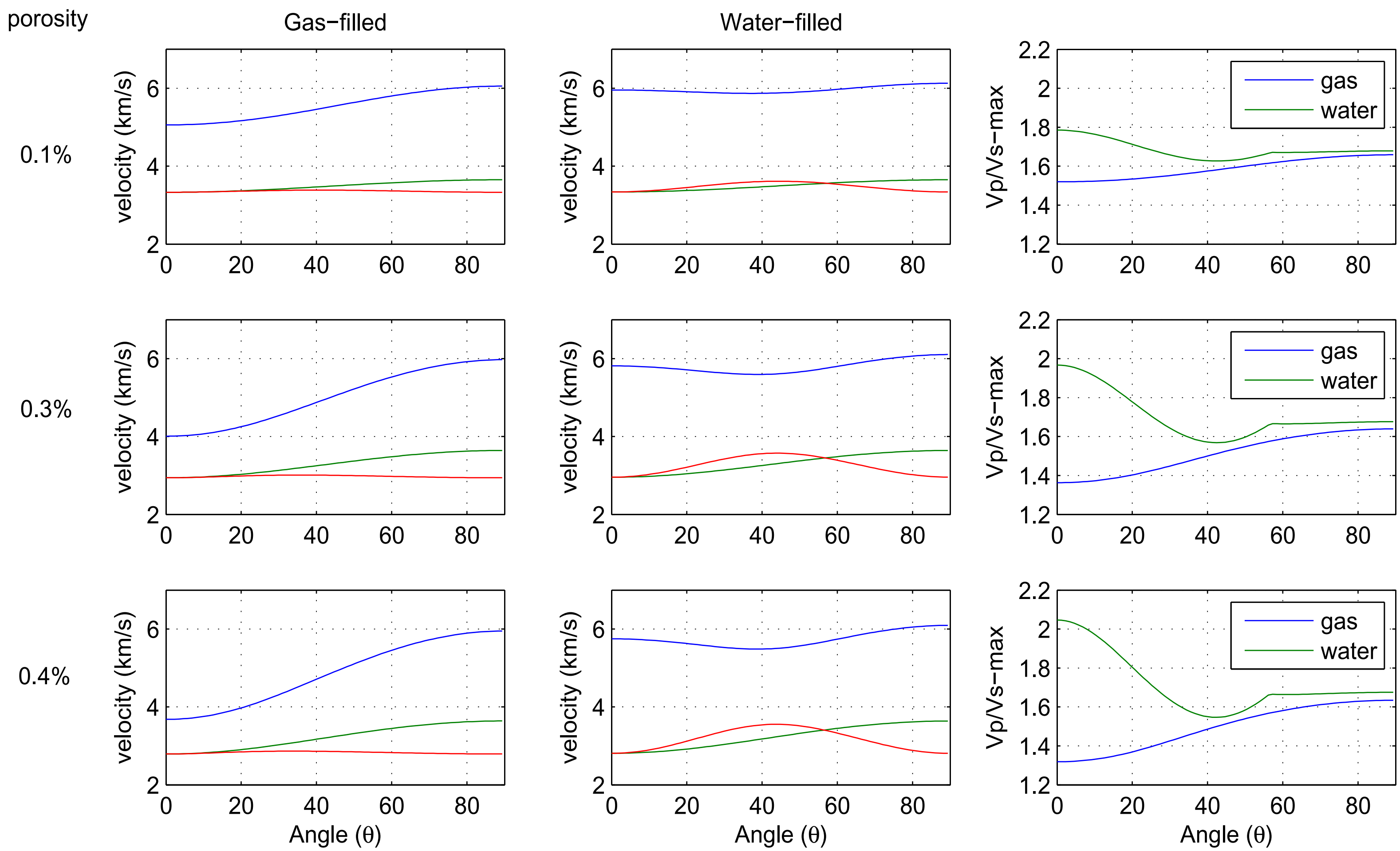

Figure 3.4: Only 5% (total = 63%) clay minerals are aligned, and rest are randomly aligned. The aspect ratio of the cracks and the friability factor are 0.01 and 0.8 respectively. The color coded velocity Vp - blue, Vs_1 - green and Vs_2 - red (for two leftmost columns). The singularity point is absent in gas-filled cracks and present in water-filled cracks. The kinks in the $Vp/Vs - max$ for water-filled cracks coincide with the singularity points. The kinks are evidently absent in gas-filled cracks.

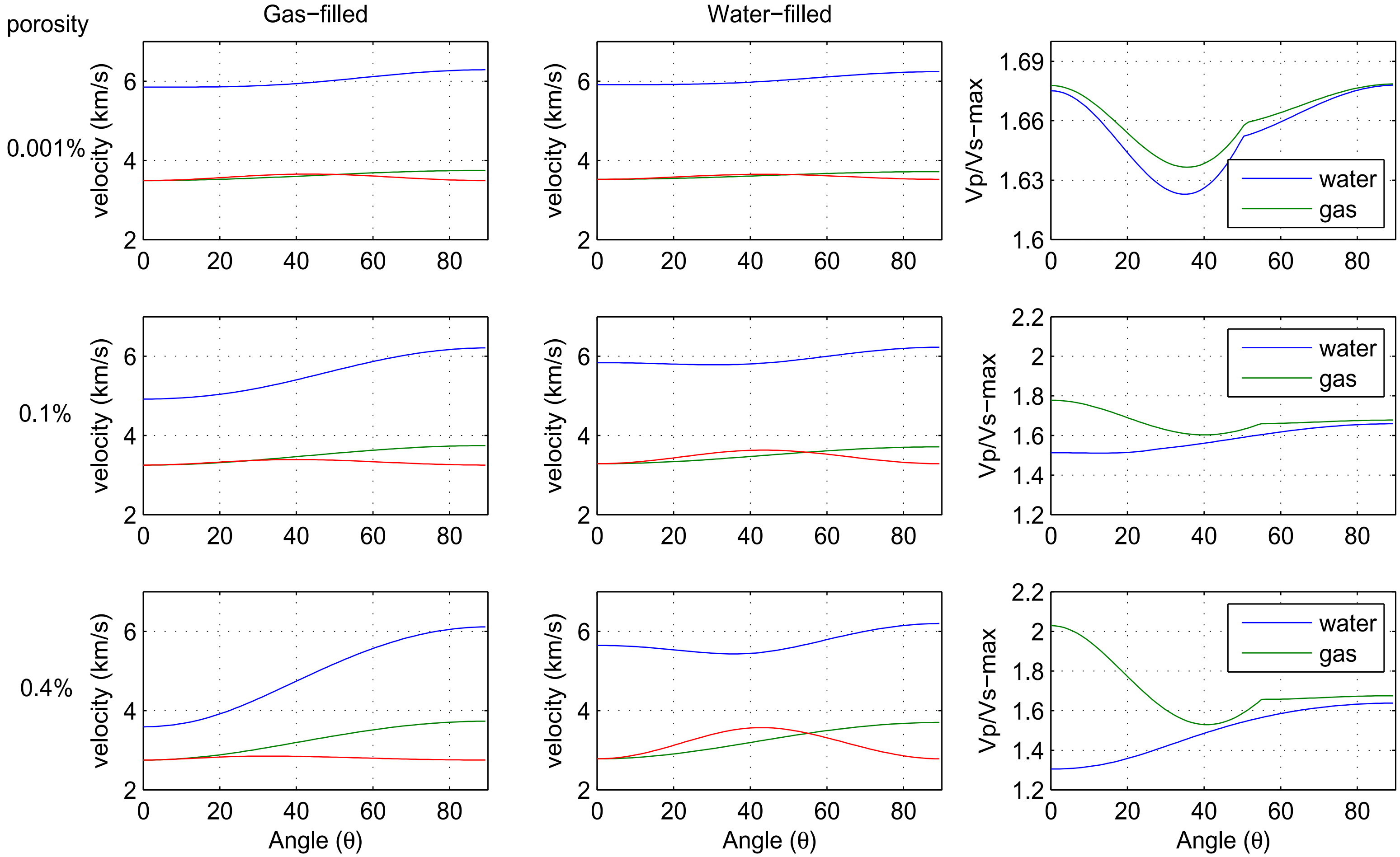

Figure 3.5: Only 20% (total = 63%) clay minerals are aligned, and rest are randomly aligned. The aspect ratio of the cracks and the friability factor are 0.01 and 0.8 respectively. The color coded velocity Vp - blue, Vs_1 - green and Vs_2 - red (for two leftmost columns). Now the singularity point appears in gas-filled cracks for the porosity = 0.001%. When the porosity increases to 0.1% the singularity point disappear. The singularity point always appears in water-filled cracks. The kinks in the $Vp/Vs - max$ for water-filled and gas-filled cracks coincide with the singularity points. In gas-filled cracks the kink is evidently present for porosity = 0.001% but absent for higher porosities.

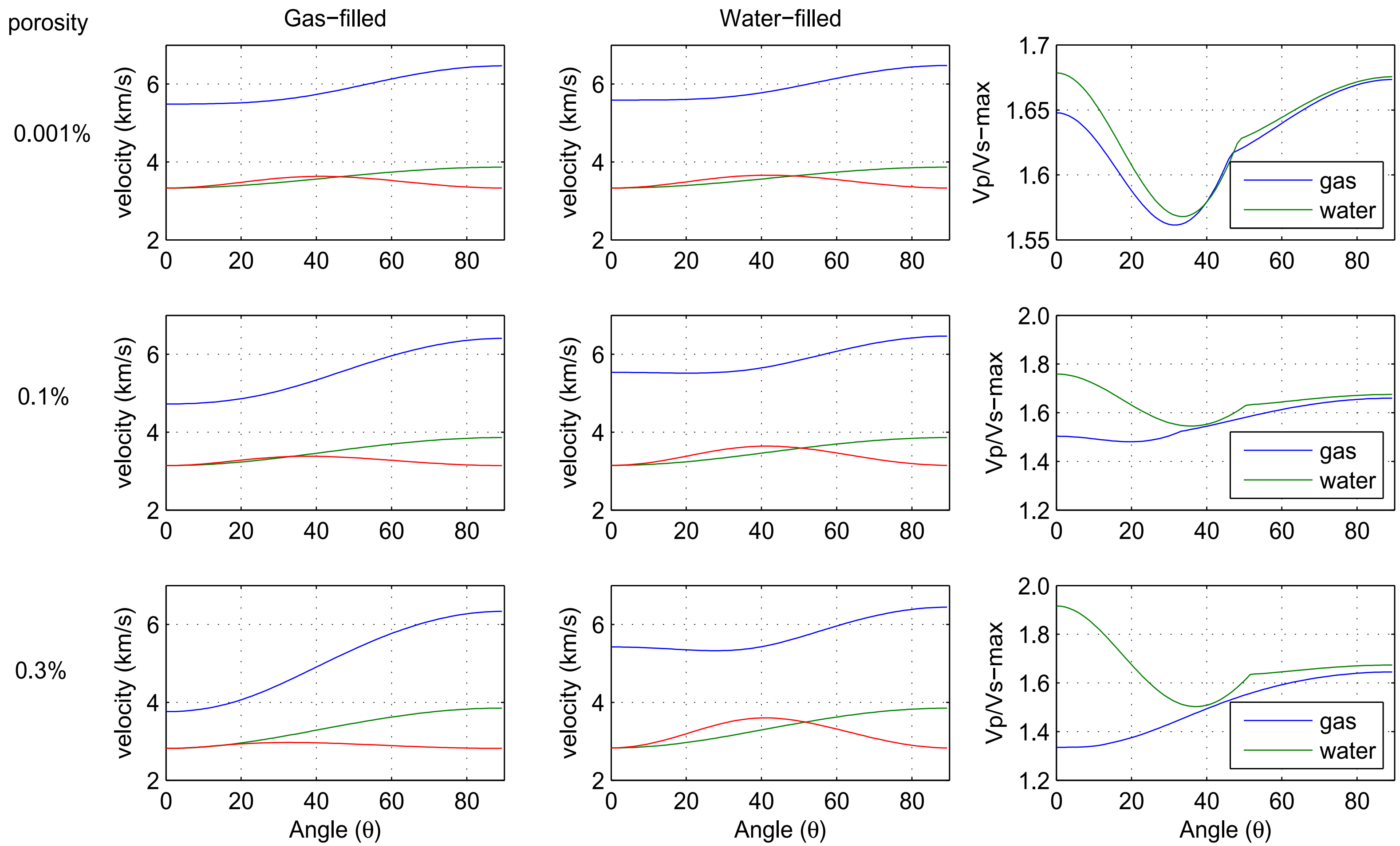

Figure 3.6: Only 40% (total = 63%) clay minerals are aligned, and rest are randomly aligned. The aspect ratio of the cracks and the friability factor are 0.01 and 0.8 respectively. The color coded velocity Vp - blue, Vs_1 - green and Vs_2 - red (for two leftmost columns). Now the singularity point appears in gas-filled cracks for the porosity = 0.001% and 0.1%. When the porosity increases to 0.3% the singularity point disappear. The singularity point always appears in water-filled cracks. The kinks in the $Vp/Vs - max$ for water-filled and gas-filled cracks coincide with the singularity points. In gas-filled cracks the kink is evidently present for porosity = 0.001% and 0.1% but absent for higher porosities.

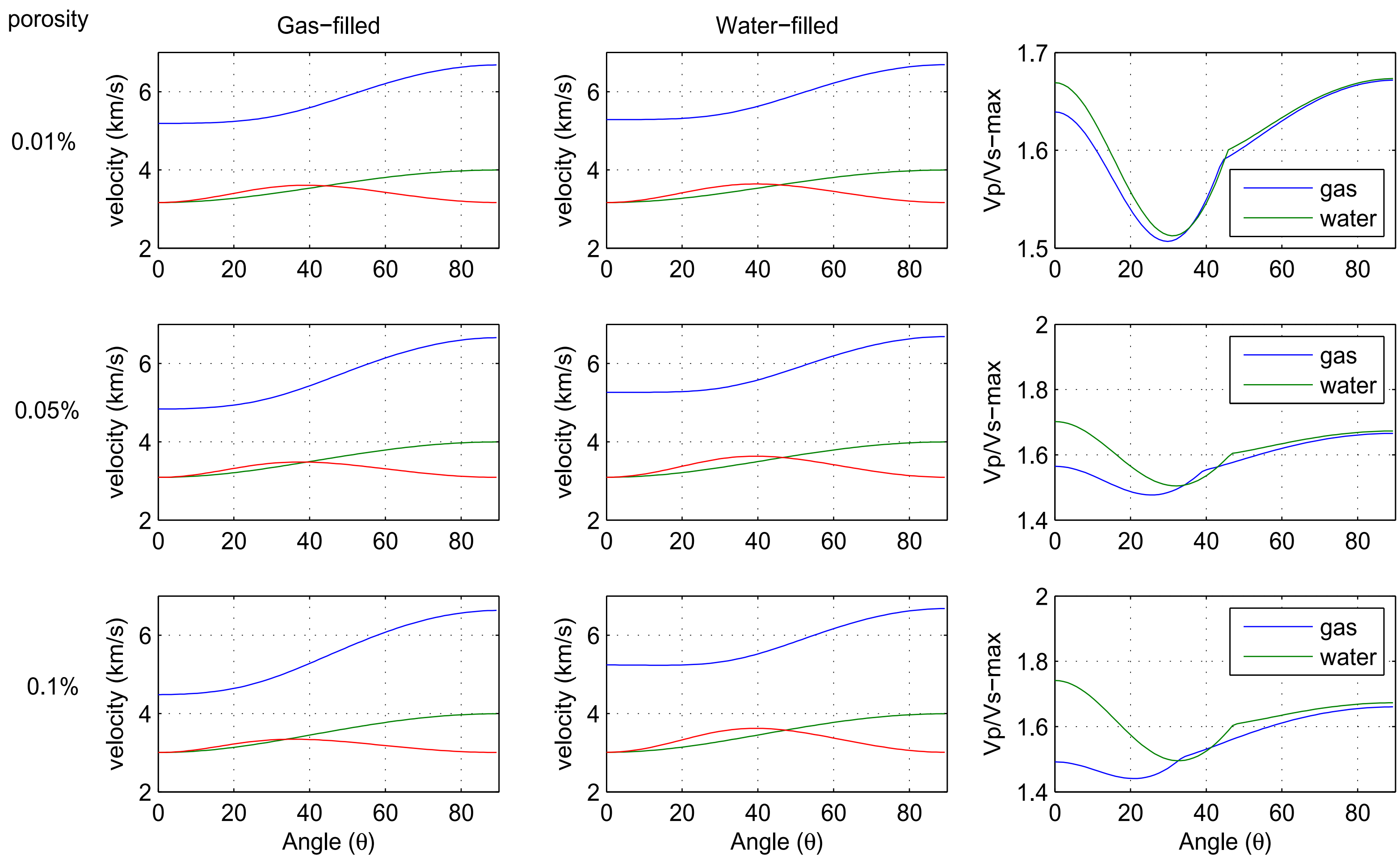

Figure 3.7: The total amount of clay minerals (63%) are aligned. The strong anisotropy is due to both, clay minerals alignment and alignment of cracks. The aspect ratio of the cracks and the friability factor are 0.01 and 0.8 respectively. The color coded velocity Vp - blue, Vs_1 - green and Vs_2 - red (for two leftmost columns). The singularity point appears in both gas-filled and water-filled cracks for all values of porosities. The kinks in the $Vp/Vs - max$ are present in all the curves.

3.3 Effect of Aspect Ratio

To identify pore fluid in rocks has always been a challenge in hydrocarbon exploration. The distinction between the types of fluid in the pores is made based on physical attributes that are sensitive to the pore-fluid. To evaluate this it important to study the behavior of the wave propagation which is produced from the coupled effect of pore fluid and the shape of the pores. The pores which house the fluid can occur in a variety of shapes. For the simplicity of mathematical derivation, cracks are consider to be either ellipsoidal, penny or needle- shape that can be represented in terms of length and breadth. Generally, the "aspect-ratio" is the ratio of the length of semi-minor axis to semi-major axis. The aspect ratio of a penny-shaped crack will range anywhere between 0 and 1. To put it in physical perspective, aspect ratio = 0 means infinitely long oblate crack and aspect ratio = 1 means spherical pores. The penny-shaped crack is the limiting case of spheroidal cracks if the third axis is very small. The aspect ratio of needle-shaped cracks may be greater than 1. The smaller the aspect ratio, the more compliant is the crack. The presence of aligned cracks in the medium results in anisotropy if there exists a contrast between the crack's filling material and the matrix in which they occur. In this section the effects of various various types of cracks and their contained fluids on wave propagation are studied in isotropic and anisotropic matrices.

In Figure 3.8 and 3.9 the effect of aspect ratio on wave propagation in cracked media is demonstrated. This study also indicates the change of P-wave and shear wave velocities resulting from changing the aspect ratio of the cracks, even though the crack-induced porosity and the connectivity of the cracks remain the same.

Increasing the aspect ratio increases the velocity of the P-wave and the S- wave, and decreases anisotropy. This phenomena is observed for cracks embedded in either an isotropic matrix (Figure 3.8) or anisotropic host matrix (Figure 3.9). It can also be noted here that the trend of Vp/Vs_{max} ratio for water-filled cracks is almost the same, irrespective of the host matrix symmetry. But for the gas-filled cracks Vp/Vs_{max} ratio shows different trend depending upon matrix symmetry, because in this case, the clay minerals alignment is partially contributing to the total anisotropy. If the host matrix is isotropic the kink in the Vp/Vs_{max} appears only in water-filled cracks. The kink indicates the presence of a singularity point in the shear waves. Because the gas-filled cracks in the isotropic host matrix do not posses a singularity point in their shear waves, the kink is absent in the Vp/Vs_{max} curve.

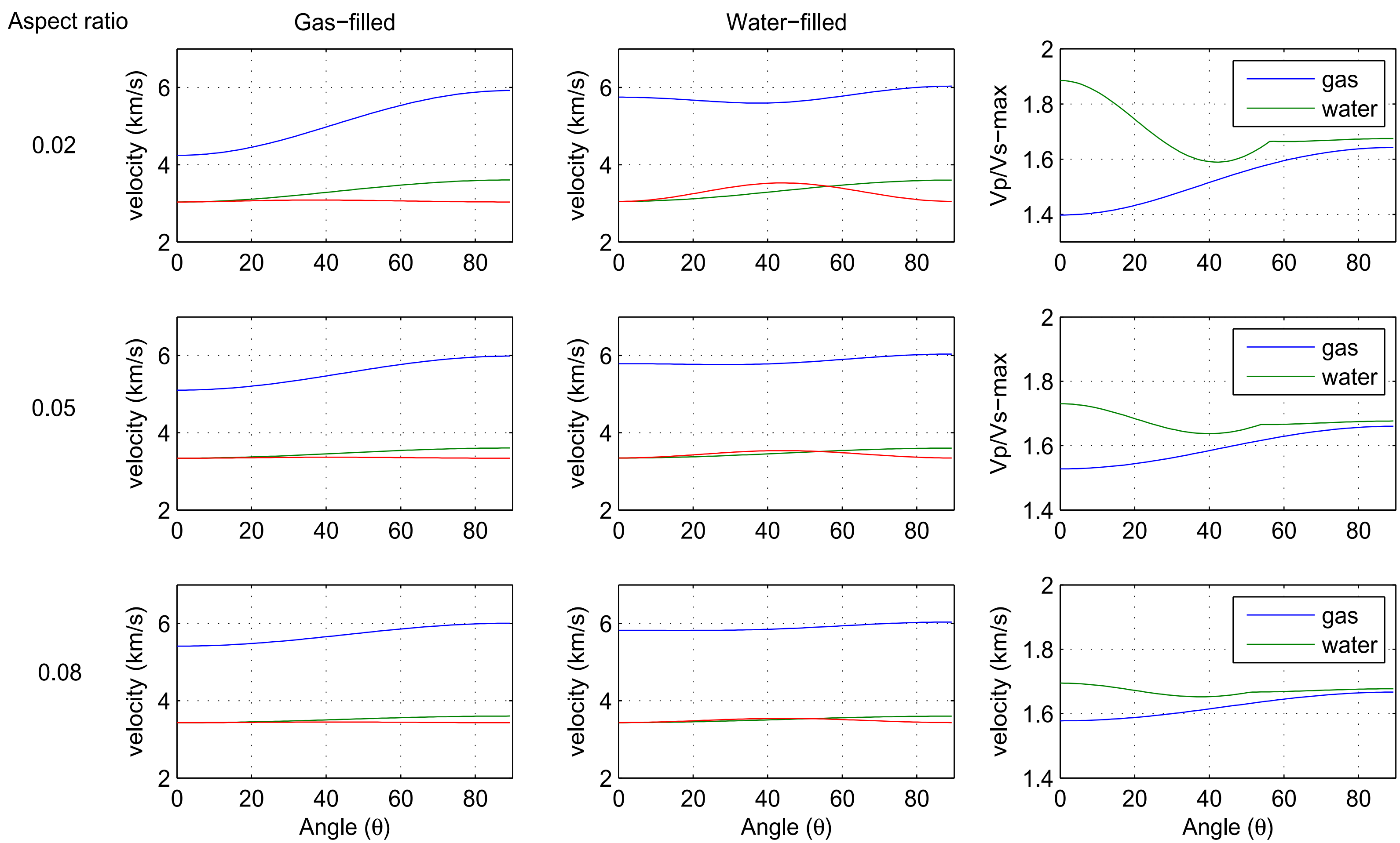

Figure 3.8: The total amount of clay minerals (63%) are randomly oriented. The anisotropy is only due to the alignment of cracks. Here, the amount of crack induced porosity (0.5%) and friability (0.8) is constant, and only aspect ratio of the cracks is variable. The color coded velocity Vp - blue, Vs_1 - green and Vs_2 - red (for two leftmost columns). The singularity point is absent in gas-filled cracks and present in water-filled cracks. The kinks in the $Vp/Vs - max$ for water-filled cracks coincide with the singularity points. The kinks are evidently absent in gas-filled cracks.

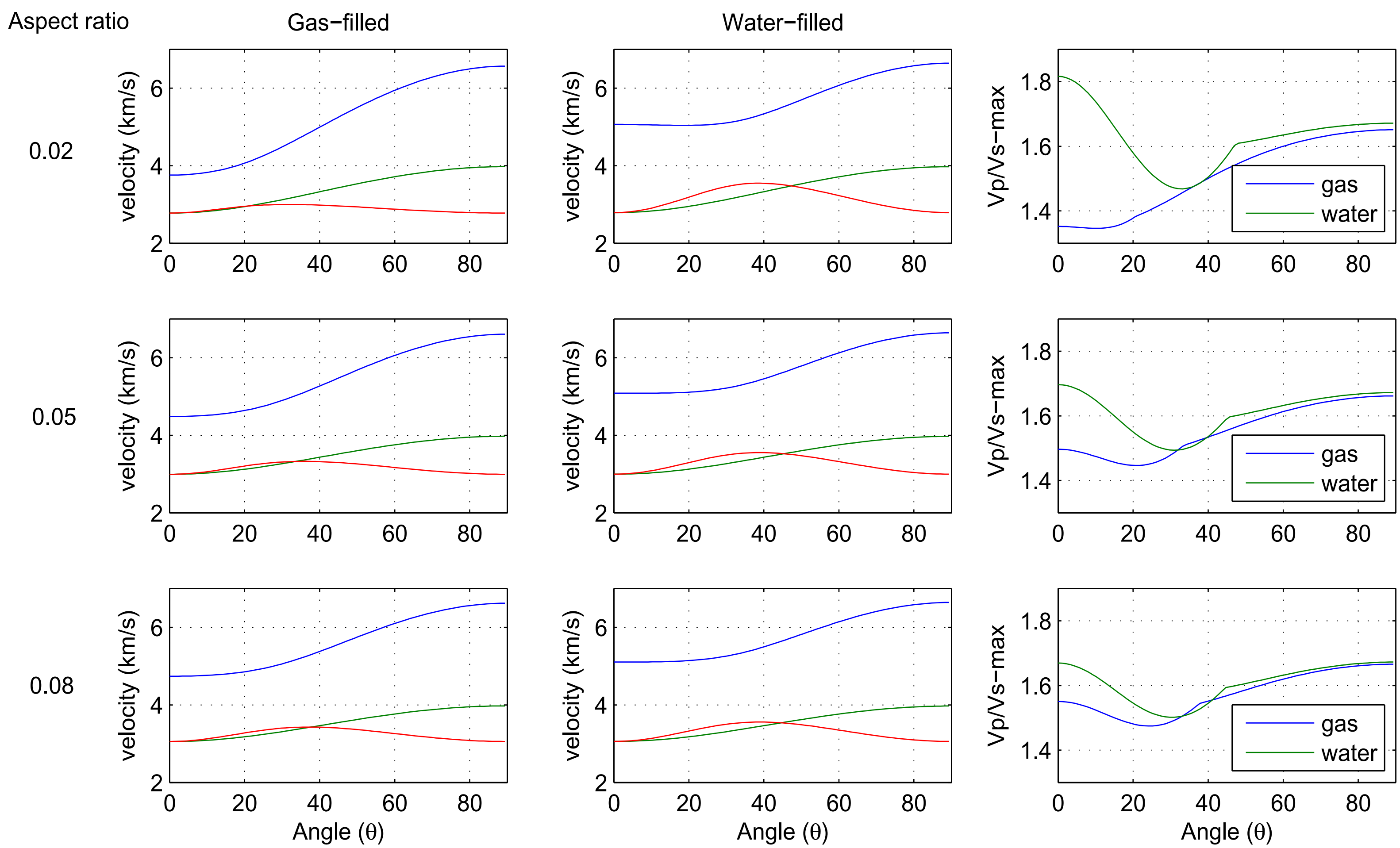

Figure 3.9: The total amount of clay minerals (63%) are aligned. The strong anisotropy is due to both, clay minerals alignment and alignment of cracks. Here, the amount of crack induced porosity (0.5%) and friability (0.8)is constant, and only aspect ratio of the cracks is variable. The color coded velocity Vp - blue, Vs_1 - green and Vs_2 - red (for two leftmost columns). The kink in the $Vp/Vs - max$ is present for both gas-filled and water-filled cracks because of the strong anisotropy of the host matrix.

3.4 Effect of Friability

This section shows quantitatively how the connectivity of the crack system affects the anisotropic properties of the media. The effect of changing the friability of the crack system embedded in an isotropic matrix and an anisotropic matrix is shown in Figure 3.10 and 3.11 respectively. To isolate the effect of friability, the aspect ratio (0.03) of the crack and the cracks induced porosity (0.5%) are kept constant. For an isotropic matrix the increase in friability increases the ratio of Vp/Vs_{max} increases in water-filled cracks, but it decreases in gas-filled cracks (Figure 3.10). Also, the singularity point in water-filled cracks moves away from the axis of symmetry with the increase in friability. In general the anisotropy increases with the increase in friability factor.

If the matrix is anisotropic (TI), and the long axis of the embedded crack is along the direction of the clay mineral alignment, the trend is the same as for Vp/Vs_{max} in an isotropic matrix. The singularity point in gas filled cracks is observed at a lower angle with the increase in friability, but it is almost constant (same angle) in water-filled cracks. It is also observed that with the increase in friability the separation of Vp/Vs_{max} between gas-filled and water-filled cracks increases, irrespective of matrix properties. When the host matrix is isotropic the kink in the $Vp/Vs-max$ is present only in water-filled cracks and absent in gas-filled cracks. But if the host matrix is anisotropic the kink appears in both gas-filled and water-filled cracks.

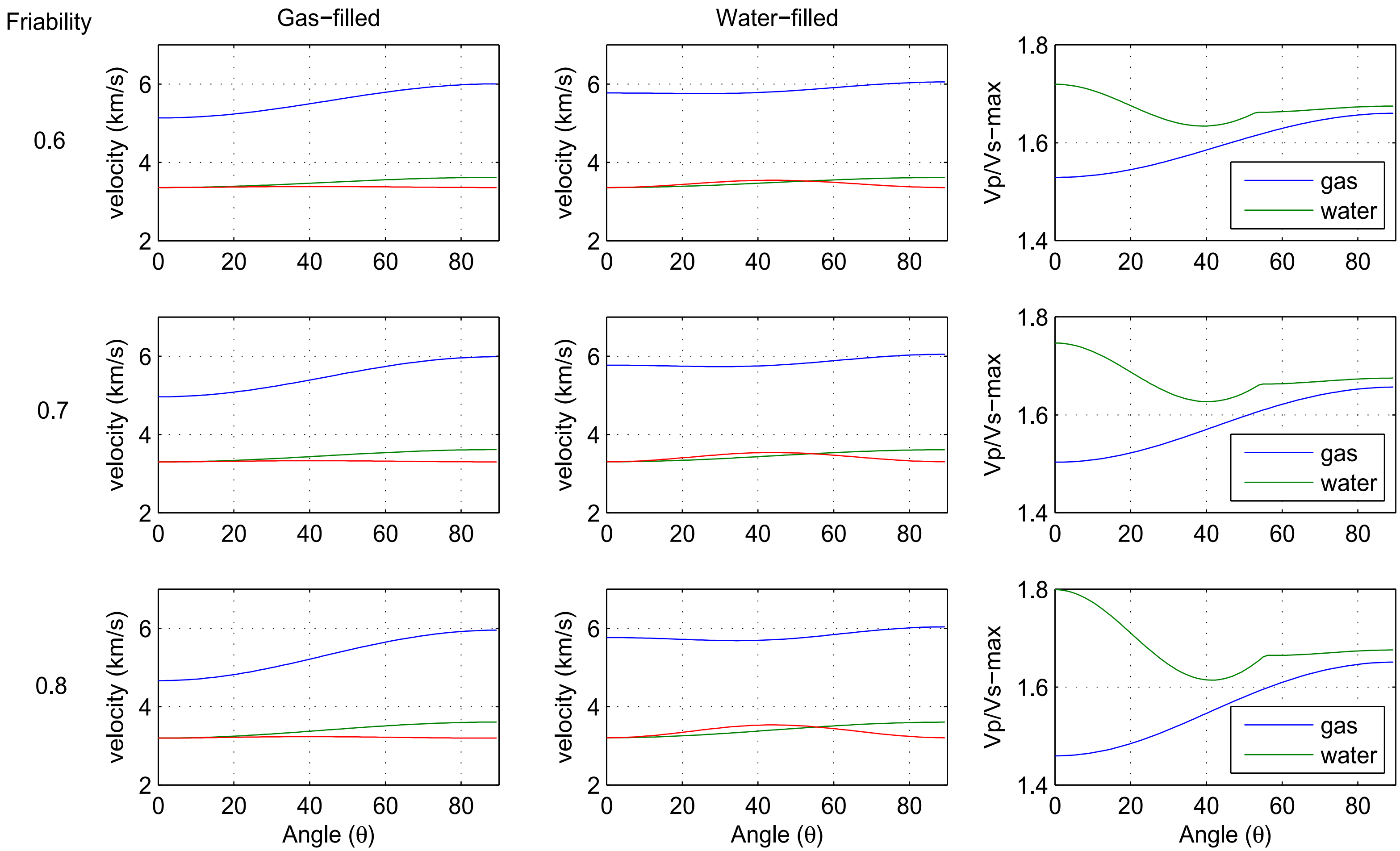

Figure 3.10: The total amount of clay minerals (63%) are randomly oriented. The anisotropy is only due to alignment of cracks. ere the amount of crack induced porosity (0.5%) and aspect ratio (0.03) is constant, and only friability is variable. The color coded velocity Vp - blue, Vs_1 - green and Vs_2 - red (for two leftmost columns). The kinks in the $Vp/Vs-max$ for water-filled cracks coincide with the singularity points. The kinks are absent in gas-filled cracks.

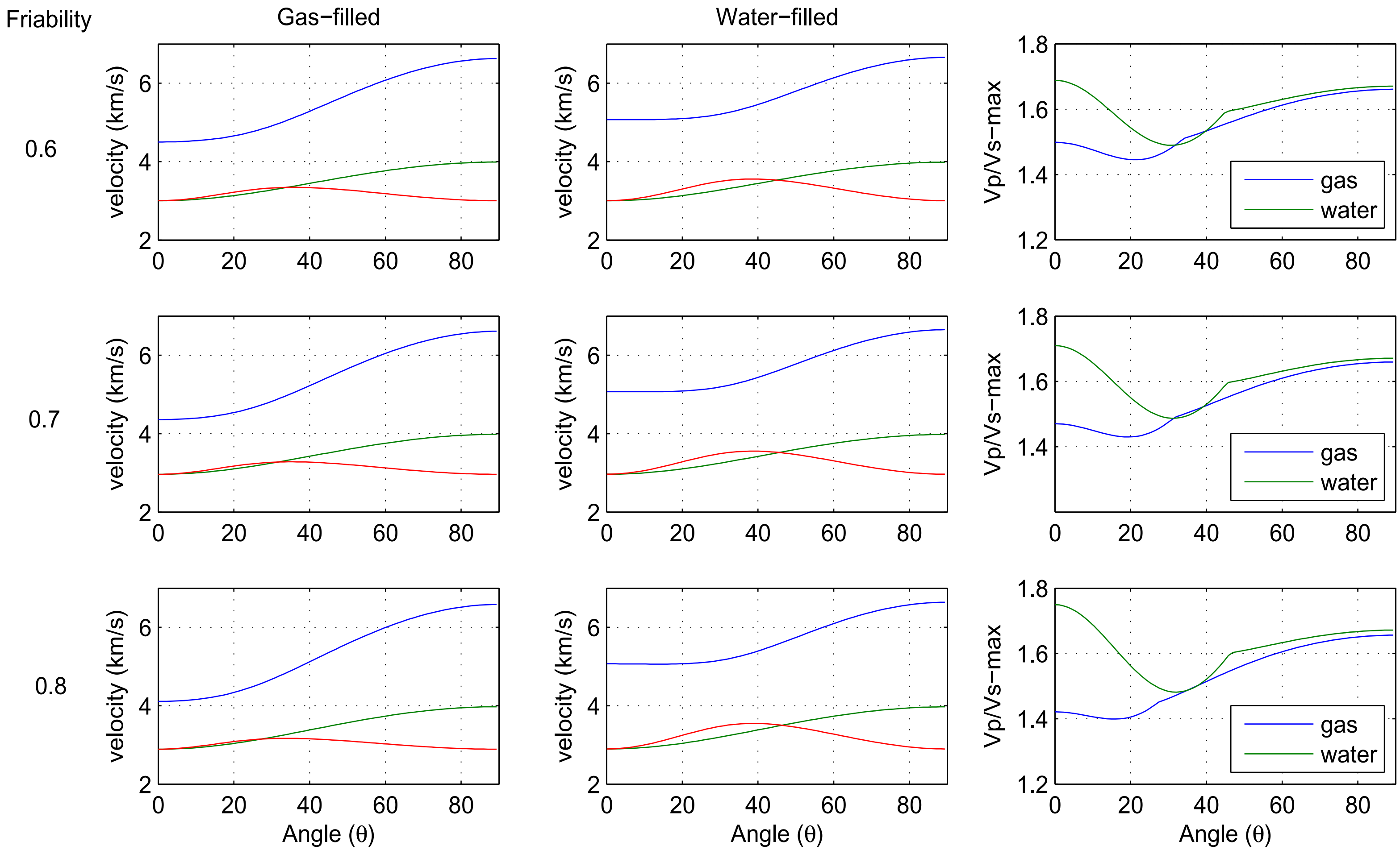

Figure 3.11: The total amount of clay minerals (63%) are aligned. The strong anisotropy is due to both, clay minerals alignment and alignment of cracks. Here the amount of crack induced porosity (0.5%) and aspect ratio (0.03) is constant, and only friability is variable. The color coded velocity Vp - blue, Vs_1 - green and Vs_2 - red (for two leftmost columns). The kink in the $Vp/Vs - max$ is present for both gas-filled and water-filled cracks because of the strong anisotropy of the host matrix.

3.5 Summary

Through detail modeling it is observed that the wave propagation in a fractured anisotropic shale depends on many variables, such as crack-induced porosity, aspect ratio of the crack, friability, and the type of fluid in present in the fractured rock. The anisotropy of the rock increases when the pores having aspect ratio less than unity, are aligned. The inherent anisotropy of the rock is significantly modified due to the presence of the aligned cracks. If the crack-induced porosity is very small then there seem to be no significant change in the behavior of Vp/Vs_{max} ratio and the kink appear in both gas-filled and water-filled cracks imbedded in the anisotropic background matrix, but it becomes distinct for a higher value of porosities. The clay-mineral alignment seems to dominate the anisotropy when the amount of crack-induced porosity is rather small. Of course, the amount of aligned porosity needed to dominate the clay-mineral-induced anisotropy will depend on how strong the clay minerals anisotropy is. The aspect ratio of the crack plays an important role in modifying the anisotropy, and so is the matrix-pore fraction of these cracks, called the friability. The increase in aspect ratio inversely affects the overall anisotropy of P-wave and the shear waves, and this effect is observed in both isotropic and anisotropic host matrix. However, the effect of increasing friability on anisotropy is positive. As the aspect ratio increases the angle at which the singularity point appears to moves towards the axis of the symmetry in both water-filled cracks in isotropic, or anisotropic matrix. But when the cracks are gas-filled the singularity point moves away from the axis of symmetry with increasing aspect ratio. The increase in the friability of a rock enhances the anisotropy, and this effect is realized for both isotropic and anisotropic matrix.

Wave propagation in the fractured reservoir is influenced by the type of pore fluid, shape of the pores, the matrix porosities, and the connectivity of these pores. Since these effects are usually coupled, this makes it hard to pin point the exact cause of anisotropy. The effect of these causes are studied here to understand their isolated effect on behavior of elastic wave. The understanding of these anisotropic rock properties are important in seismic imaging, prestack seismic analysis, and reservoir characterization.

Chapter 4

Ultrasonic Measurements of Shale Anisotropy: Forward Modeling

High resolution lithological characterization based on a core-study indicates nine different facies in the Barnett Shale which correspond to nine different depositional environment (Singh and Slatt, 2006). For each of the nine facies compressional and shear wave velocity are measured on samples at ultrasonic frequencies ($1MHz$). The velocities based on first break picking are measured at room temperature and pressure. Based on elastic properties obtained from the rock samples belonging to the different facies, the Barnett Shale can be characterized by five different groups, which are either isotropic, or VTI in nature. The volume concentration of each mineral phase is estimated using XRD and FTIR techniques. The GSA method (Chapter 2) is used to perform forward modeling to estimate the elastic constants from each samples's mineralogical assemblage. The velocities estimated using forward modeling and the ultrasonic measurements are then used to extract the crack-induced porosity, the aspect ratio of the cracks, and the friability. The extraction is based on inverse modeling applying a minimization function. The best realistic solution is chosen from a number of possible solutions obtained during inverse modeling. The microfabric analyses provided by SEM photomicrographs give qualitative information about crack's parameters (Φ, χ, and $\Im$), which in turn help to constrain the inversion solution. The maximum error in estimating between measured velocity and mineralogy-based velocity for different facies is 18% for FTIR mineralogy, and 30% for XRD. Thus mineralogy-based estimates of the velocities can be used as a tool to characterize sedimentary facies in the absence of any other sources of velocity data.

4.1 Introduction

The elastic properties of the shale have a large degree of variation. These variations reflect the depositional environment and the diagenetic processes the sediments have gone through over geological time. The high resolution sequence stratigraphy developed by Singh and Slatt (2006) for the Barnett Shale, Fort-Worth basin, divides the Barnett shale into nine different facies. This facies characterization of the Barnett Shale is primarily based on lithologic signature determined through the detailed study of core and thin-sections.

From each of the nine facies of the Barnett Shale, samples were collected and the measurements of velocity in different directions were performed to estimate the elastic constants of the rock. The difference in the velocities measured in at least two of the orthogonal directions in a horizontal plane is very small. Therefore, based on the velocity structure of the different facies, these facies behave as either isotropic, or transversely isotropic with a vertical axis of symmetry. The mineralogical assemblages of each of the samples is estimated by X-ray diffraction (XRD) technique by evaluating the XRD intensity pattern for each of the nine samples. The XRD patterns of the nine samples are shown in Figure 4.1. The 2θ values of primary shale minerals are listed in Table 4.1. The weight percentage of the minerals obtained from XRD is converted into a volume fraction to make the calculation of the effective elastic constants. The calculation of elastic constants using the GSA method is based on forward modeling where it starts from the volume fraction, elastic constants and density of each mineral phase estimated in the rock sample. The purpose of this chapter is to extract the information about physical properties of rocks, such as crack induced porosity, the friability factor, and the aspect ratio of the cracks using elastic properties obtained via forward modeling and lab measurements. Well log data and other available information about the microstructure can be used to restrict the inverse modeling solutions to realistic values.

4.2 XRD and FTIR Mineralogy

The X-ray diffraction technique uses an X-ray beam having a wavelength comparable to the distance between the atomic or molecular structure of interest. The atomic planes of a crystal cause incident X-rays to interfere with one another as they leave the crystal. This phenomenon is called X-ray diffraction. It measures the average spacing between layers or rows of atoms. This technique helps to determine the orientation of a single crystal and the crystal structure. The powdered sample is exposed to the X-ray beam, and the intensity of the diffraction obtained against 2θ for the nine samples is shown in Figure 4.1. The identification of minerals is based on the value of 2θ and the weight percentage concentration of the minerals is dependent on the intensity of the diffraction peak. The mineral concentration so obtained is shown in Table 4.2. The intensity of the diffraction pattern at $2\theta = 29.6^0$ is very high (close to 300 cps) in N4, N6 and N8, suggesting that these samples are very rich in calcareous materials. The samples N3, N5, N7 and N8 show the highest peak for $2\theta = 26.6^0$, indicating that these samples have high silica content. The weight percentage of other significant minerals present in the rock samples estimated using X-ray diffraction (XRD) are shown in Table 4.2.

Also, the mineral composition of the nine samples obtained using Fourier Transmission Infrared (FTIR) were made available by Devon Energy Inc. The mineral assemblage obtained from FTIR technique belong to the same depth of the same core, which was used for the X-ray diffraction analysis. The detection of minerals using FTIR spectroscopy is based on the detection of molecular vibrations. The mineral identification is based on the absorption band in the mid-range of the infrared (4000 to 400 cm^{-1}), the characteristic range for most of the minerals (Xu et al., 2007). The weight percentage of the minerals can be estimated from the FTIR absorption spectra based on Beer's law, which states that the absorbance of the mixture is proportional to the concentration of each mineral obtained. The FTIR estimated mineral weight percentages are shown in Table 4.3.

Table 4.1: Primary shale minerals and their 2θ values. [from Breeden and Shipman (2004)].

Minerals	Quartz	Feldspar	Calcite	Dolomite	Siderite	Pyrite	Clays		
2θ (deg)	26.6	27.5	29.6	31.0	31.8	33.1	19.9	34.6	61.9

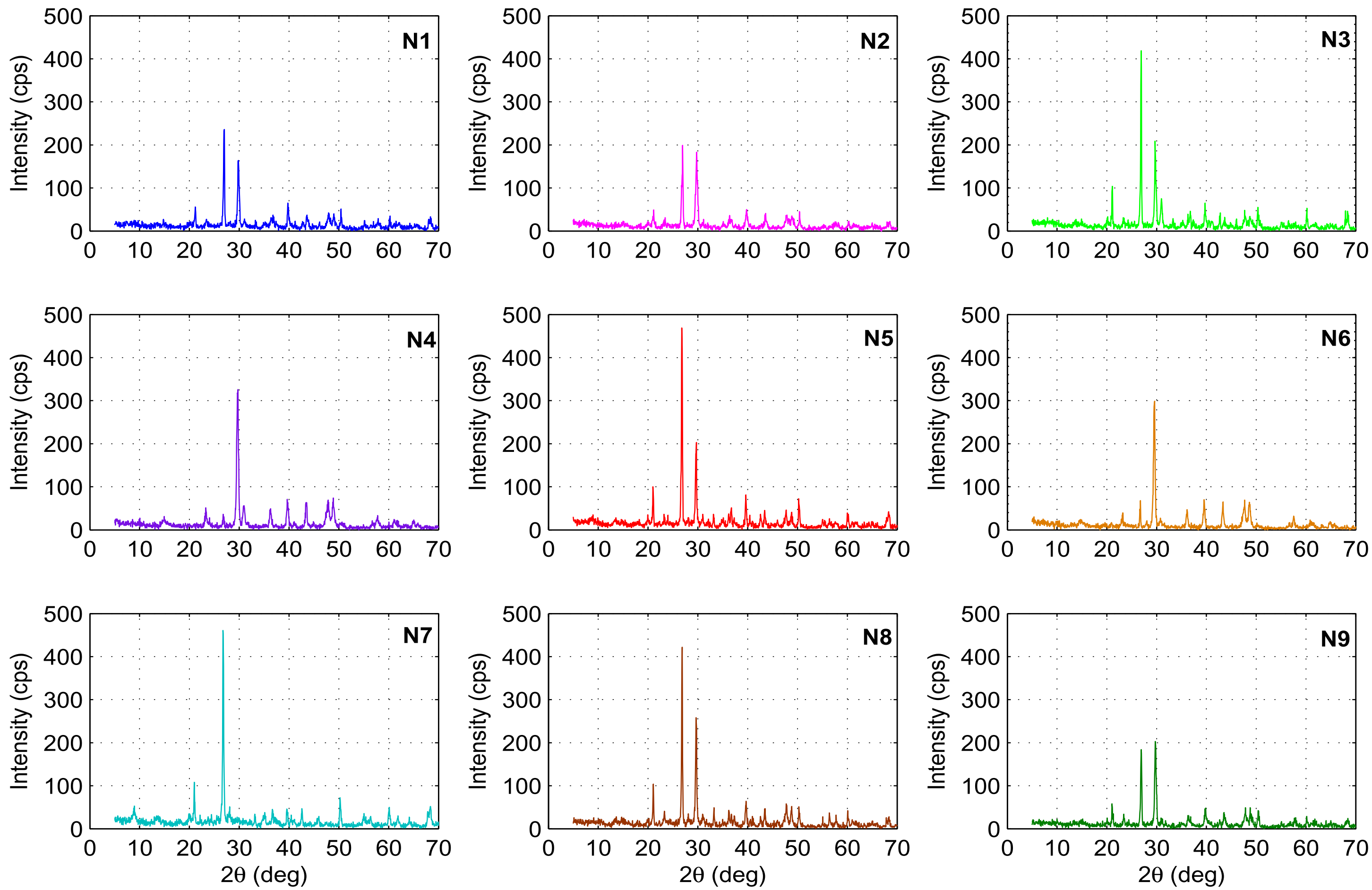

Figure 4.1: XRD pattern of nine rock samples (N1 - N9) representing different sedimentary facies of the Barnett Shale. N1=calcareous mudstone, N2=limy mudstone, N3=wavy-bed deposit, N4=dolomitic mudstone, N5=fossils-rich deposit, N6=concretion, N7=non-calcareous, N8=calcareous laminae, and N9=phosphatic deposit.

Table 4.2: Major mineralogical composition of the nine different facies of the Barnett Shale, Fort-Worth basin, in weight percentage using X-ray diffraction technique.

Facies Name	**Qua– rtz**	**Cal– cite**	**Dolo– mite**	**Feld– spar**	**Py– rite**	**Side– rite**	**Apa- tite**	**Al- bite**	**Anhy- drite**	**Total Clays**
Calcareous Mudstone	21	7	6	6	2	4	6	6	2	39
Limy Mudstone	28	16	5	5	0	3	5	7	4	28
Wavy-bed Deposit	21	7	13	3	3	1	15	7	3	26
Dolomitic Mudstone	17	11	8	5	1	5	8	6	4	37
Fossils-rich Deposit	51	8	4	3	2	2	6	6	2	18
Concretion	10	44	5	3	1	1	4	3	2	27
Non-calcareous	55	3	3	3	1	1	2	5	2	25
Calcareous Laminae	34	5	5	4	2	3	7	5	2	29
Phosphatic Deposit	17	8	8	5	1	5	8	6	4	37

Table 4.3: Major mineralogical composition of the nine different facies of the Barnett Shale, Fort-Worth basin, in weight percentage using FTIR technique. (Data courtesy of Devon Energy Inc.)

Facies Name	**Quartz**	**Calcite**	**Dolomite**	**Feldspar**	**Pyrite**	**Siderite**	**Apatite**	**Total Clays**
Calcareous Mudstone	16	22	0	13	0	8	4	37
Limy Mudstone	25	22	3	13	0	6	0	31
Wavy-bed Deposit	29	26	4	8	0	11	1	21
Dolomitic Mudstone	10	37	16	5	0	7	0	25
Fossils-rich Deposit	20	20	0	10	0	4	7	39
Concretion	13	61	0	14	2	7	0	3
Non-calcareous	23	4	0	21	0	5	4	43
Calcareous Laminae	8	50	14	9	0	3	1	15
Phosphatic Deposit	14	6	6	12	0	7	5	50

4.3 Calculation of Elastic Constants by Forward Modeling

The elastic constants of each of the nine facies are calculated using the GSA based forward modeling method and the minerals assemblage obtained from the XRD and FTIR techniques. The modeling stats with illite-rich clay mineral, which is the softest among all components. Then other minerals, such as quartz, calcite, dolomite, pyrite, feldspar, etc. are introduced as the inclusions. The effective elastic constants of the composite are estimated as a function of porosity (0 - 100%). The elastic constants at the percentage which equals the percentage of the inclusions will be further used to model cracks.

4.4 Rock Sampling

Barnett Shale rock samples were collected from the same continuous well, used for facies delineation by Singh and Slatt (2006). Each sample was designed to give cubical or parallelopiped shape with two additional parallel faces at 45^0 to the bedding plane (Figure 4.2). In order to extract all the five elastic constants that define VTI and isotropic symmetry. The opposite planes are parallel to within 1% error which will lead to a tolerable error in the final calculation of the elastic constants. It is assumed during the sampling that the core was taken from a vertical well, so that the dipping laminae in the core is reflect the true geological dip.

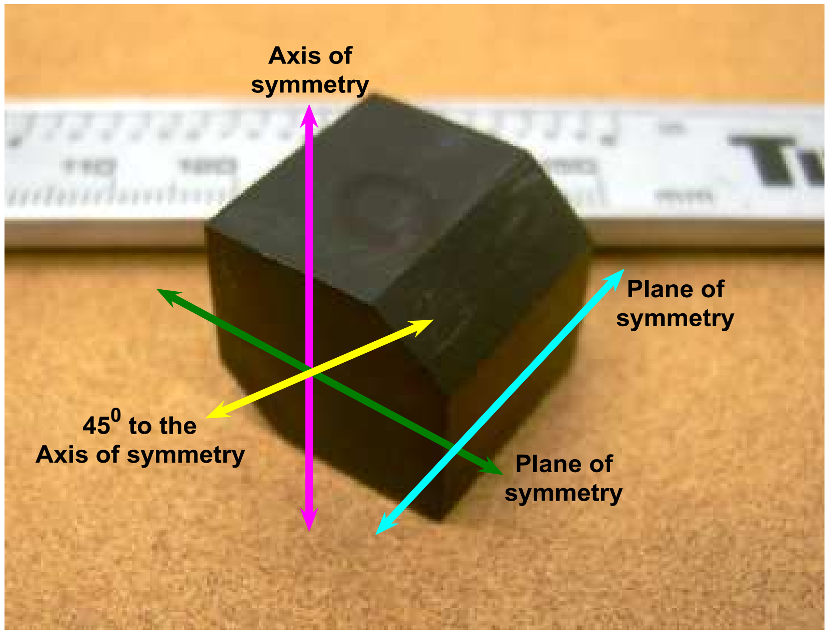

Figure 4.2: Sample designed for the ultrasonic measurements. The axis of symmetry is vertical. The value of θ will always be measured from the axis of symmetry.

4.5 Ultrasonic Measurements

P- and S-wave transducers are used to measure the P-wave and S- wave velocities, respectively, with the ultrasonic frequency (1 MHz) at room temperature and pressure. According to Auld (1973) if the width of the transducers are very small compared to the size of the sample, the group velocity is measured; otherwise the phase velocity is measured if the width of the transducers are compared to the sample size. Dellinger and Vernik (1994) conclude through numerical calculation, that if the separation between transducers is more than three times greater than the width, that "almost all pulse-transmission experiments of this kind should measure anisotropic phase velocity, not group velocity". Thus, my measurements are of phase velocity.

The time arrival of P- and S- waves is based on first break picking (Figure 4.3 and 4.4). From the measurements of P-wave, S- wave velocities, and density the elastic constants (C_{IJ}, where I and J = 1,2,...6) of each of the facies are calculated (Table 4.5).

It can be observed in Table 4.5 that the C_{11} and C_{33} values for three facies: dolomitic mudstone, concretion and calcareous laminae, are almost equal, as are the value of C_{44} and C_{66}. This behavior of C_{IJ} results in non-splitting of shear waves, and characterize isotropic facies (Figure 4.8, 4.10 and 4.12). The velocities measured in any direction are the same for the isotropic samples and the Thomsen's parameters are very small in these three facies. The other six facies can be characterized as transversely isotropic media with vertical axes of symmetry.

It can also be observed that the elastic constants (C_{IJ}) of calcareous mudstone- and limy mudstone facies (Figure 4.5 and 4.6) wavy-bed deposit and fossils-rich deposit facies (Figure 4.7 and 4.9) and non-calcareous and phosphatic deposit facies (Figure 4.11 and 4.13), are in same range. If only the elastic behavior of these facies were available it would be difficult to distinguish calcareous mudstone facies from limy mudstone facies; wavy-bed deposit facies from fossils-rich deposit facies; and non-calcareous facies from phosphatic deposit. Therefore, it can be concluded that on the basis of elastic properties, the Barnett Shale has only five "seismic" facies. In Figures 4.5, 4.7, and 4.11 the measured velocities along two orthogonal directions in the plane of symmetry are different. This implies that these three facies are nearly VTI. This can also be observed from the photomicrograph which shows slightly dipping laminae.

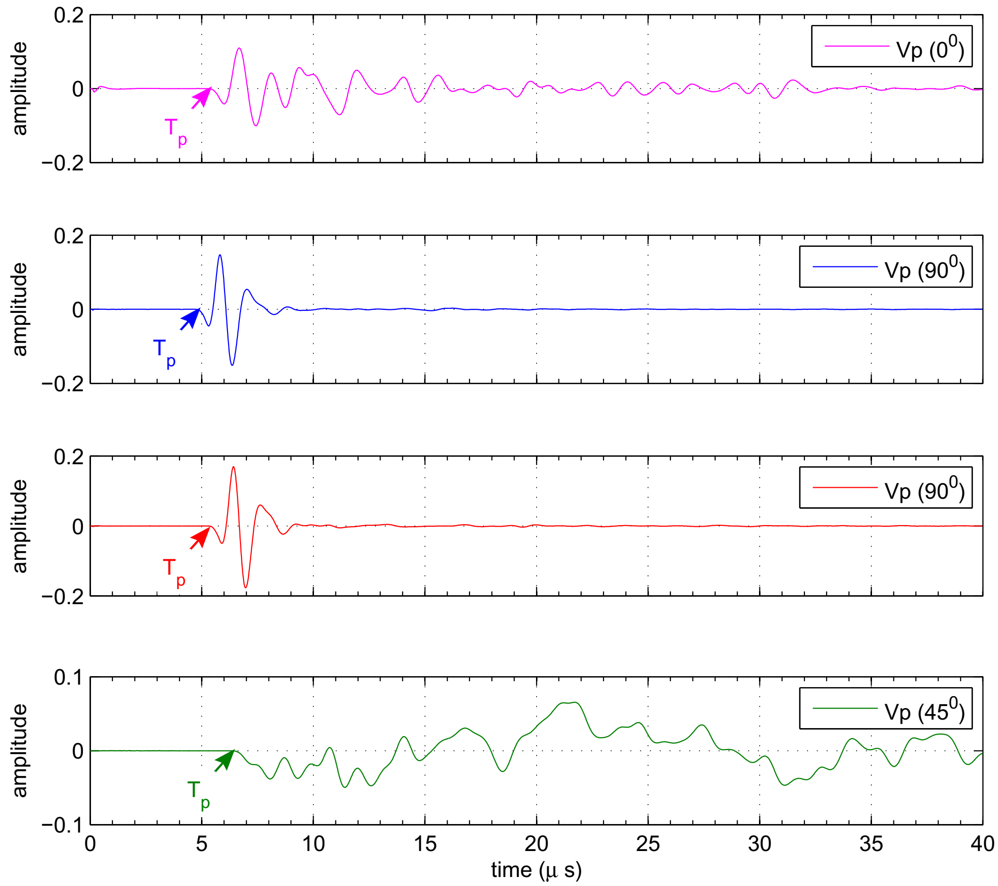

Figure 4.3: P-wave signals along 0^0, 45^0, and 90^0 to the axis of symmetry. The arrows indicate the time arrival of P-wave along these directions

The phase velocity, C_{IJ} and microphotograph for each facies, along with Thomsen's parameters, are given in Figures 4.5 - 4.13. The microfabric observed in the microphotograph of each facies can be used to explain the measured ultrasonic velocities. In all the microphotographs, wherever an order in the arrangement of minerals is observed, it results in anisotropy as observed in the microphotographs of calcareous mudstone, limy mudstone, wavy-bed deposit, fossil-rich deposit, non-calcareous, and phosphatic deposit.

Interestingly, the rest of the three rock samples: dolomitic mudstone, concretion, and calcareous laminae facies, which behave as isotropic based on ultrasonic velocity, do not exhibit any order or alignment in their microstructures. In these rock samples, velocity in every direction is essentially the same. This can also be seen by their elastic constants: $C_{11} = C_{22} = C_{33}$ and $C_{44} = C_{55} = C_{66}$ (Table 4.5).

In some of the phase velocity plots there is quite a difference between measured and predicted quasi S- wave velocity. This difference is attributed to the difficulty in delineating the shear wave arrival on the vertically polarized seismogram. Figure 4.4 shows two shear-wave seismograms with the polarization vector in-plane to the displacement vector (blue) and the polarization vector perpendicular to the plane of displacement (red). Because of the ambiguity in picking up the shear-wave arrival on the vertically polarized wave the estimated velocity, sometimes, is not correct. This is reflected on the phase velocity plot where predicted and measured quasi-shear wave do not match. This difference may be reduced significantly if the measurement is performed at high pressure which will yield a better quality seismogram due to the closure of thin cracks.

Table 4.4: Elastic constants and the Thomsen's parameters extracted from the ultrasonic (1MHz) velocity measurements of nine rock samples, each one them represents a different geological facies. Manually calculated density and sampling depths are also shown.

Facies Name	**Seismic Facies**	$\mathbf{C_{11}}$ (GPa)	$\mathbf{C_{13}}$ (GPa)	$\mathbf{C_{33}}$ (GPa)	$\mathbf{C_{44}}$ (GPa)	$\mathbf{C_{66}}$ (GPa)	ρ (g/cc)	**Thomsen's Parameters**		
								ε	γ	δ
Calcareous Mudstone	I	60.337	10.569	27.223	11.206	21.683	2.54	0.608	0.467	0.250
Limy Mudstone	I	61.323	38.939	25.862	13.23	22.101	2.53	0.693	0.335	0.062
Wavy-bed Deposit	II	75.030	31.048	45.242	18.084	26.514	2.65	0.329	0.233	0.682
Fossils-rich Deposit	II	76.379	19.811	58.109	21.600	25.903	2.64	0.157	0.100	0.090
Dolomitic Mudstone	III	84.720	35.819	84.122	25.930	26.244	2.70	0.004	0.006	0.044
Concretion	IV	96.468	47.581	94.980	28.953	29.034	2.66	0.008	0.001	0.119
Calcareous Laminae	IV	92.149	30.350	90.951	29.37	29.773	2.66	0.006	0.007	-0.020
Non-calcareous	V	54.897	12.435	21.263	11.327	21.114	2.41	0.790	0.432	1.103
Phosphatic Deposit	V	52.548	10.328	26.414	10.59	17.909	2.47	0.494	0.346	0.224

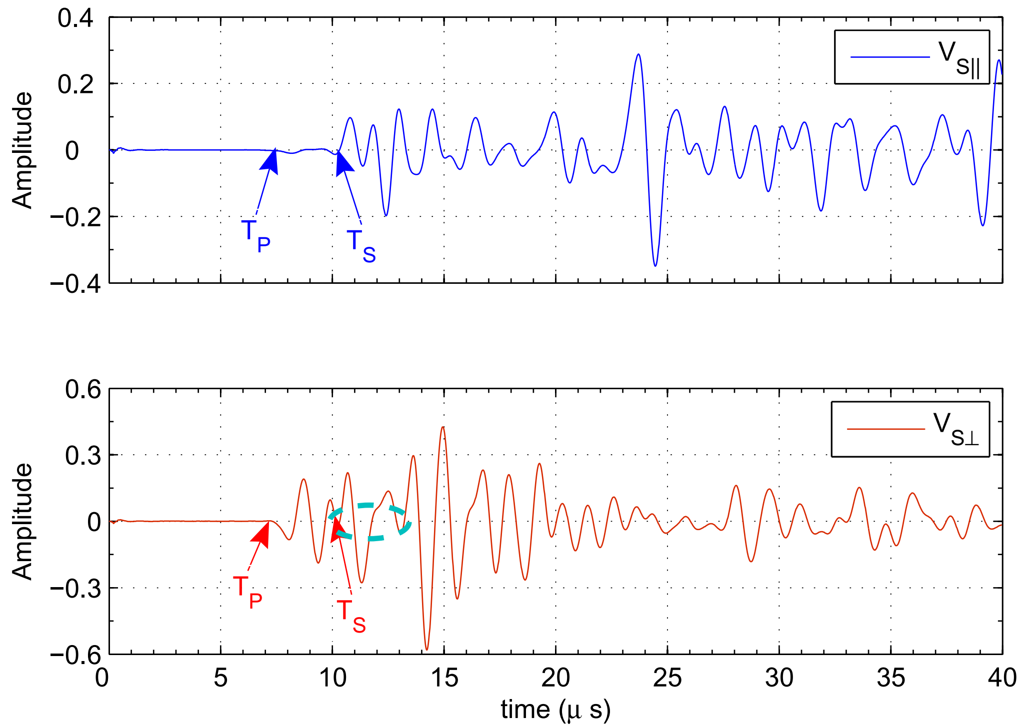

Figure 4.4: Shear wave seismograms along 45^0 to the axis of symmetry. The delineation of the shear wave arrival is comparatively easier on horizontally polarized waveform $V_{S||}$ (blue color) than on vertically polarized waveform $V_{S\perp}$ (red color). T_P and T_S indicate the P- and S- wave arrival respectively. The cyan color ellipse represents uncertainty in S- wave arrival picking.

4.6 Forward Modeling Including Cracks

Modeling starts with the host matrix (clay minerals); the other minerals are introduced as the inclusions in the host matrix. Since from thin sections and SEM photomicrographs, it it observed that the inclusions are embedded in the clay minerals host matrix. The elastic constants obtained in Section 4.3 represent "crack-free" rock. From these elastic constants the P-wave and S- wave velocities in any direction can be calculated using the Green-Christoffel equation. However, the P-wave and S-waves velocities were calculated along directions parallel, perpendicular, and at 45^0

$$C_{IJ} = \begin{pmatrix} 60.34 & 16.97 & 10.57 & 0 & 0 & 0 \\ 16.97 & 60.34 & 10.57 & 0 & 0 & 0 \\ 10.57 & 10.57 & 27.22 & 0 & 0 & 0 \\ 0 & 0 & 0 & 11.21 & 0 & 0 \\ 0 & 0 & 0 & 0 & 11.21 & 0 \\ 0 & 0 & 0 & 0 & 0 & 21.68 \end{pmatrix} \text{GPa}, \quad \begin{matrix} \varepsilon = 0.608 \\ \gamma = 0.467 \\ \delta = 0.250 \\ \rho = 2.54 \ \text{g/cc} \end{matrix}$$

(a)

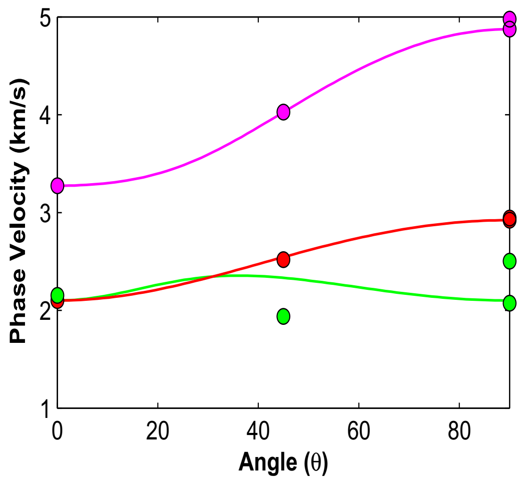

(b)

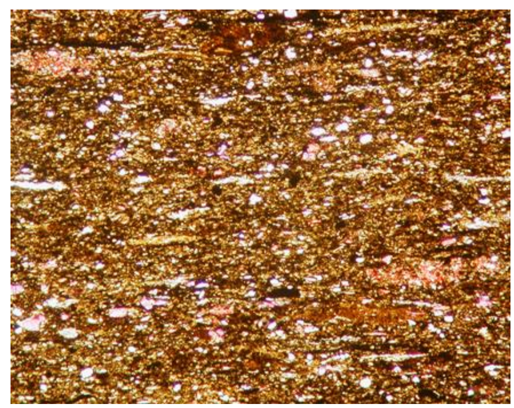

(c)

Figure 4.5: Calcareous mudstone facies: (a) Elasticity tensor with the Thomsen's parameters (b) the calculated phase velocity from elasticity tensor. Color magenta, red and green represents Vp, Vs_1 and Vs_2 respectively, and the solid colored circles are the measured data in the lab. The values Vp along two orthogonal directions in the symmetry plane are not equal. This indicates that the medium is not true VTI. (c) Photomicrograph (x10) shows that the inclusions are randomly distributed with preferred alignment in the host matrix. The anisotropy is due to the clay mineral alignment.

$$C_{IJ} = \begin{pmatrix} 61.32 & 18.83 & 10.09 & 0 & 0 & 0 \\ 18.83 & 61.32 & 10.09 & 0 & 0 & 0 \\ 10.09 & 10.09 & 36.41 & 0 & 0 & 0 \\ 0 & 0 & 0 & 14.24 & 0 & 0 \\ 0 & 0 & 0 & 0 & 14.24 & 0 \\ 0 & 0 & 0 & 0 & 0 & 21.25 \end{pmatrix} \text{GPa}, \qquad \begin{array}{c} \varepsilon = 0.342 \\ \gamma = 0.246 \\ \delta = 0.062 \\ \\ \rho = 2.53 \ \ \text{g/cc} \end{array}$$

(a)

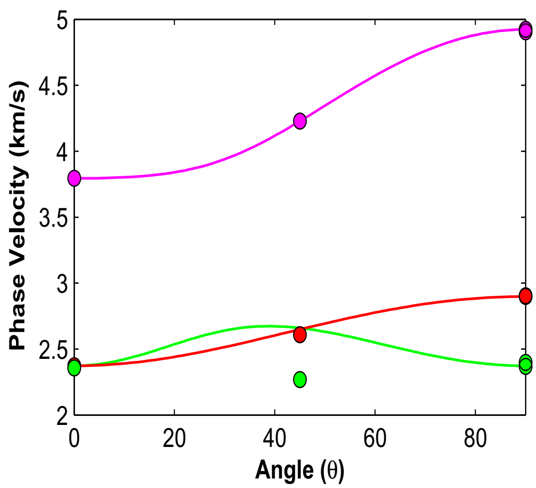

(b)

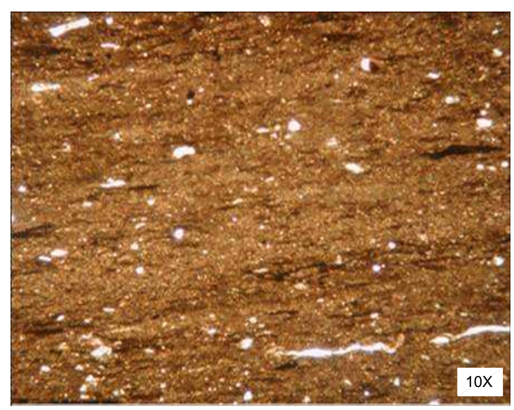

(c)

Figure 4.6: Same as Figure 4.5 but for limy mudstone facies. This facies shows slightly weaker anisotropy than calcareous mudstone facies because the clay mineral alignment is not so strong.

$$
C_{IJ} = \begin{pmatrix} 75.03 & 22.00 & 31.05 & 0 & 0 & 0 \\ 22.00 & 75.03 & 31.05 & 0 & 0 & 0 \\ 31.05 & 31.05 & 45.24 & 0 & 0 & 0 \\ 0 & 0 & 0 & 18.08 & 0 & 0 \\ 0 & 0 & 0 & 0 & 18.08 & 0 \\ 0 & 0 & 0 & 0 & 0 & 26.51 \end{pmatrix} \text{GPa}, \quad \begin{matrix} \varepsilon = 0.329 \\ \gamma = 0.233 \\ \delta = 0.682 \\ \\ \rho = 2.65 \ \ \text{g/cc} \end{matrix}
$$

(a)

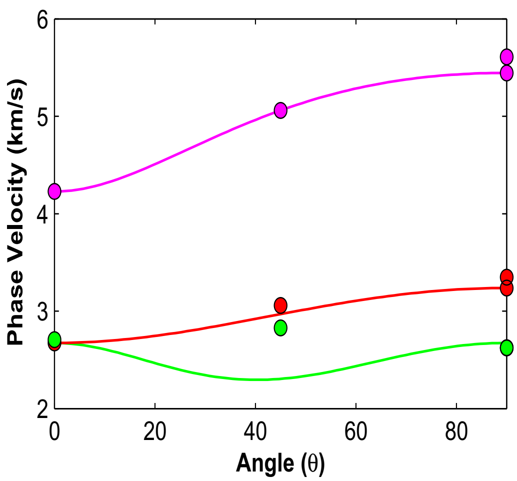

(b)

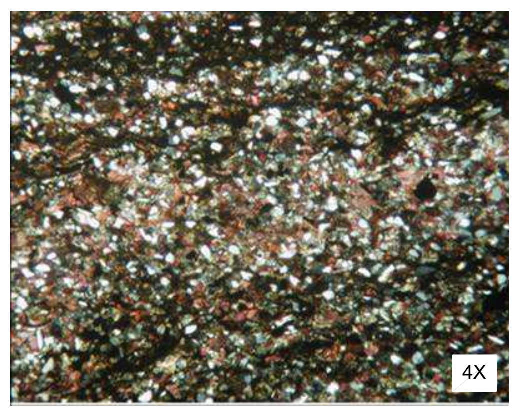

(c)

Figure 4.7: Same as Figure 4.5 but for wavy-bed deposit facies. This facies does not show preferred alignment of clay minerals.

$$C_{IJ} = \begin{pmatrix} 84.72 & 32.26 & 35.82 & 0 & 0 & 0 \\ 32.26 & 84.72 & 35.82 & 0 & 0 & 0 \\ 35.82 & 35.82 & 84.12 & 0 & 0 & 0 \\ 0 & 0 & 0 & 25.93 & 0 & 0 \\ 0 & 0 & 0 & 0 & 25.93 & 0 \\ 0 & 0 & 0 & 0 & 0 & 26.24 \end{pmatrix} \text{GPa}, \quad \begin{aligned} \varepsilon &= 0.004 \\ \gamma &= 0.006 \\ \delta &= 0.026 \\ \rho &= 2.70 \ \ \text{g/cc} \end{aligned}$$

(a)

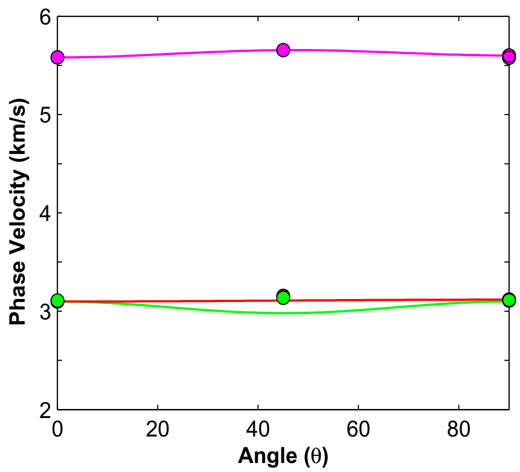

(b)

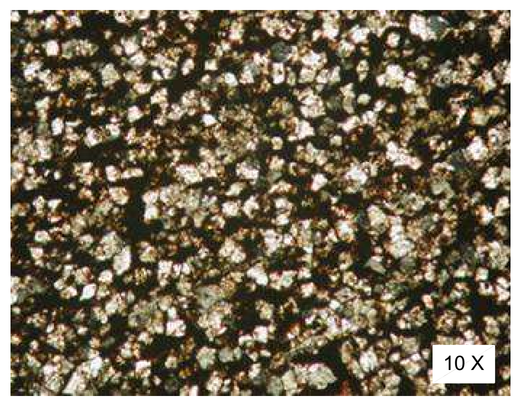

(c)

Figure 4.8: Dolomitic mudstone facies: (a) Elasticity tensor (b) Phase velocity color magenta, red and green represents Vp, Vs_1 and Vs_2 respectively, and the solid colored circles are the measured data in the lab. (c) Photomicrograph (10X) showing that inclusions are randomly distributed with no preferred alignment in the host matrix. This facies is characterized by isotropic behavior of P- and S- waves.

$$C_{IJ} = \begin{pmatrix} 76.38 & 24.57 & 19.81 & 0 & 0 & 0 \\ 24.57 & 76.38 & 19.81 & 0 & 0 & 0 \\ 19.81 & 19.81 & 58.11 & 0 & 0 & 0 \\ 0 & 0 & 0 & 21.60 & 0 & 0 \\ 0 & 0 & 0 & 0 & 21.60 & 0 \\ 0 & 0 & 0 & 0 & 0 & 25.90 \end{pmatrix} \text{GPa}, \qquad \begin{array}{l} \varepsilon = 0.157 \\ \gamma = 0.100 \\ \delta = 0.090 \\ \\ \rho = 2.64 \ \ \text{g/cc} \end{array}$$

(a)

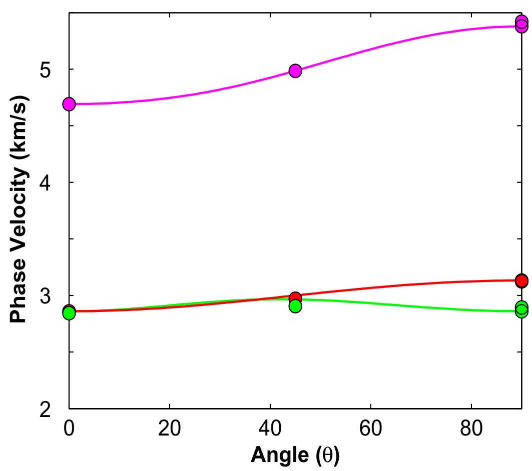

(b)

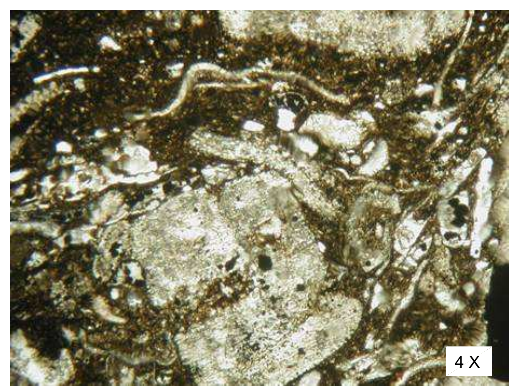

(c)

Figure 4.9: Fossils-rich deposit facies: (a) Elasticity tensor (b) Phase velocity color magenta, red and green represents Vp, Vs_1 and Vs_2 respectively, and the solid colored circles are the measured data in the lab. (c) Photomicrograph (4X) shows that the inclusions are randomly distributed with preferred alignment in the host matrix. This facies is weakly anisotropic, which is reflected by the small values of the Thomsen's parameters.

$$C_{IJ} = \begin{pmatrix} 96.46 & 38.40 & 47.58 & 0 & 0 & 0 \\ 37.07 & 96.46 & 47.58 & 0 & 0 & 0 \\ 47.58 & 47.58 & 94.98 & 0 & 0 & 0 \\ 0 & 0 & 0 & 28.95 & 0 & 0 \\ 0 & 0 & 0 & 0 & 28.95 & 0 \\ 0 & 0 & 0 & 0 & 0 & 29.03 \end{pmatrix} \text{GPa}, \quad \begin{array}{c} \varepsilon = 0.008 \\ \gamma = 0.001 \\ \delta = 0.119 \\ \\ \rho = 2.66 \ \ \text{g/cc} \end{array}$$

(a)

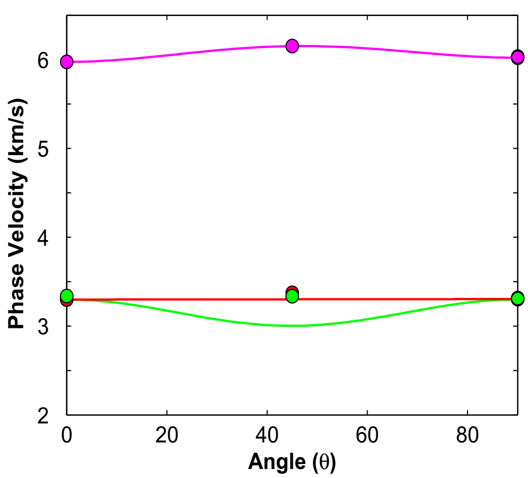

(b)

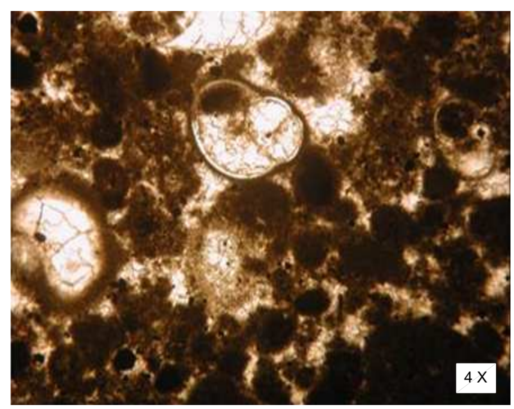

(c)

Figure 4.10: Concretion facies: (a) Elasticity tensor (b) Phase velocity color magenta, red and green represents Vp, Vs_1 and Vs_2 respectively, and the solid colored circles are the measured data in the lab. (c) Photomicrograph (4X) shows that inclusions are randomly distributed with no preferred alignment in the host matrix. This facies is characterized by isotropic behavior of P- and S- waves, and high P- and S- wave velocities.

$$C_{IJ} = \begin{pmatrix} 54.89 & 12.67 & 12.43 & 0 & 0 & 0 \\ 12.67 & 54.89 & 12.43 & 0 & 0 & 0 \\ 12.43 & 12.43 & 21.26 & 0 & 0 & 0 \\ 0 & 0 & 0 & 11.32 & 0 & 0 \\ 0 & 0 & 0 & 0 & 11.32 & 0 \\ 0 & 0 & 0 & 0 & 0 & 21.11 \end{pmatrix} \text{GPa}, \quad \begin{array}{c} \varepsilon = 0.790 \\ \gamma = 0.432 \\ \delta = 1.103 \\ \\ \rho = 2.41 \ \ \text{g/cc} \end{array}$$

(a)

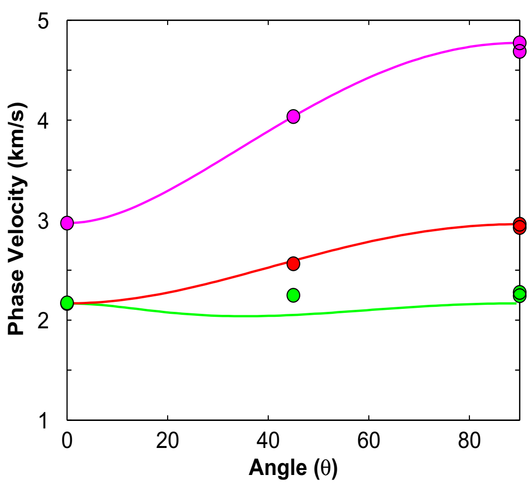

(b)

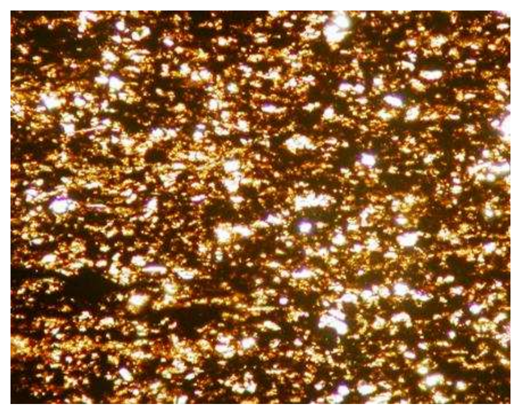

(c)

Figure 4.11: Non-calcareous facies: (a) Elasticity tensor (b) Phase velocity color magenta, red and green represents Vp, Vs_1 and Vs_2 respectively, and the solid colored circles are the measured data in the lab. (c) Photomicrograph shows that the inclusions are randomly distributed with no preferred alignment in the host matrix.

$$C_{IJ} = \begin{pmatrix} 92.15 & 32.60 & 30.35 & 0 & 0 & 0 \\ 32.60 & 92.15 & 30.35 & 0 & 0 & 0 \\ 30.35 & 30.35 & 90.95 & 0 & 0 & 0 \\ 0 & 0 & 0 & 29.37 & 0 & 0 \\ 0 & 0 & 0 & 0 & 29.37 & 0 \\ 0 & 0 & 0 & 0 & 0 & 29.77 \end{pmatrix} \text{GPa}, \qquad \begin{array}{l} \varepsilon = 0.007 \\ \gamma = 0.007 \\ \delta = -0.020 \\ \\ \rho = 2.66 \ \ \text{g/cc} \end{array}$$

(a)

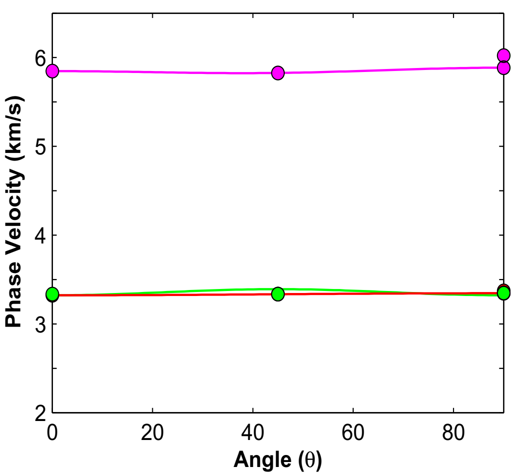

(b)

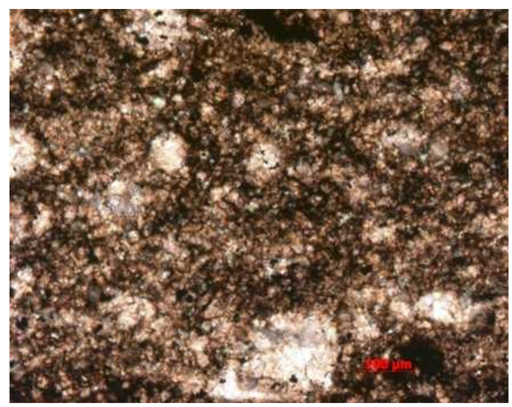

(c)

Figure 4.12: Calcareous laminae facies: (a) Elasticity tensor (b) Phase velocity color magenta, red and green represents Vp, Vs_1 and Vs_2 respectively, and the solid colored circles are the measured data in the lab. (c) Photomicrograph shows that the inclusions are randomly distributed with no preferred alignment in the host matrix. This facies is characterized by isotropic behavior of P- and S- waves, and high P- and S- wave velocities.

$$C_{IJ} = \begin{pmatrix} 52.55 & 16.73 & 10.33 & 0 & 0 & 0 \\ 18.83 & 52.55 & 10.33 & 0 & 0 & 0 \\ 10.33 & 10.33 & 26.41 & 0 & 0 & 0 \\ 0 & 0 & 0 & 10.59 & 0 & 0 \\ 0 & 0 & 0 & 0 & 10.59 & 0 \\ 0 & 0 & 0 & 0 & 0 & 17.91 \end{pmatrix} \text{GPa}, \quad \begin{array}{c} \varepsilon = 0.494 \\ \gamma = 0.346 \\ \delta = 0.224 \\ \\ \rho = 2.47 \ \ \text{g/cc} \end{array}$$

(a)

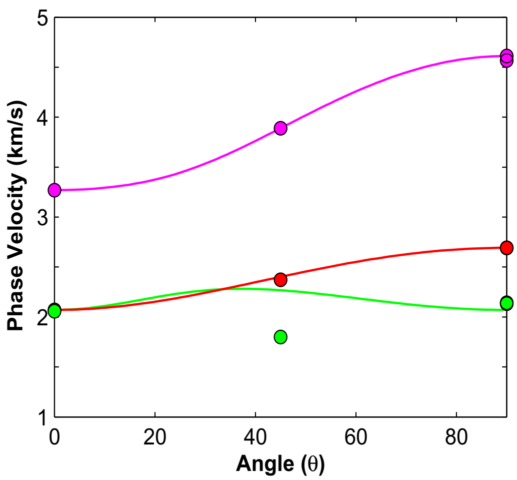

(b)

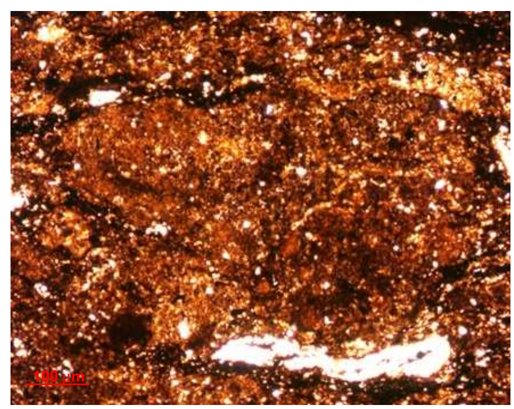

(c)

Figure 4.13: Phosphatic deposit facies: (a) Elasticity tensor (b) Phase velocity color magenta, red and green represents Vp, Vs_1 and Vs_2 respectively, and the solid colored circles are the measured data in the lab. (c) Photomicrograph shows that the inclusions are randomly distributed with weak alignment in the host matrix.

to the axis of the effective symmetry. These velocities are then used to estimate the microstructure of the rocks.

4.7 Inversion for Crack Parameters

The crack-free elastic constants estimated using forward modeling are now set as the background matrix into which cracks having different aspect ratios are introduced. The model will be evaluated for different concentrations of cracks (crack-induced porosity) and friability factor. The main purpose is to extract that combination of aspect ratio (χ), crack-induced porosity (Φ) and friability ($\Im$) which can provide the best fit to the measured ultrasonic velocity. This is achieved by applying a minimization function to every point in χ-Φ -$\Im$ space. The minimization function is defined as

$$L = \sum_{i=1}^{3} \left[\left| \frac{V^t_{p_{(i)}} - V^m_{p_{(i)}}}{V^m_{p_{(i)}}} \right| + \left| \frac{V^t_{s1_{(i)}} - V^m_{s1_{(i)}}}{V^m_{s1_{(i)}}} \right| + \left| \frac{V^t_{s2_{(i)}} - V^m_{s2_{(i)}}}{V^m_{s2_{(i)}}} \right| \right] \times 100\%, \tag{4.1}$$

where, L is the percentage error to be minimized as a function of χ, Φ, and $\Im$, superscripts t and m represent the theoretical and measured value of the velocities, and i=1, 2 and 3 represent the velocity measurements at angle 0^0, 45^0 and 90^0 respectively.

Figure 4.14 shows all the points in 3D space in which every point represents a fixed value of the aspect ratio (χ), crack induced porosity (Φ) and friability ($\Im$). The velocities for each point are calculated and compared with the lab measured velocities. Let's assume that at any one grid point, L_1 is the error in V_p, Vs_1 and

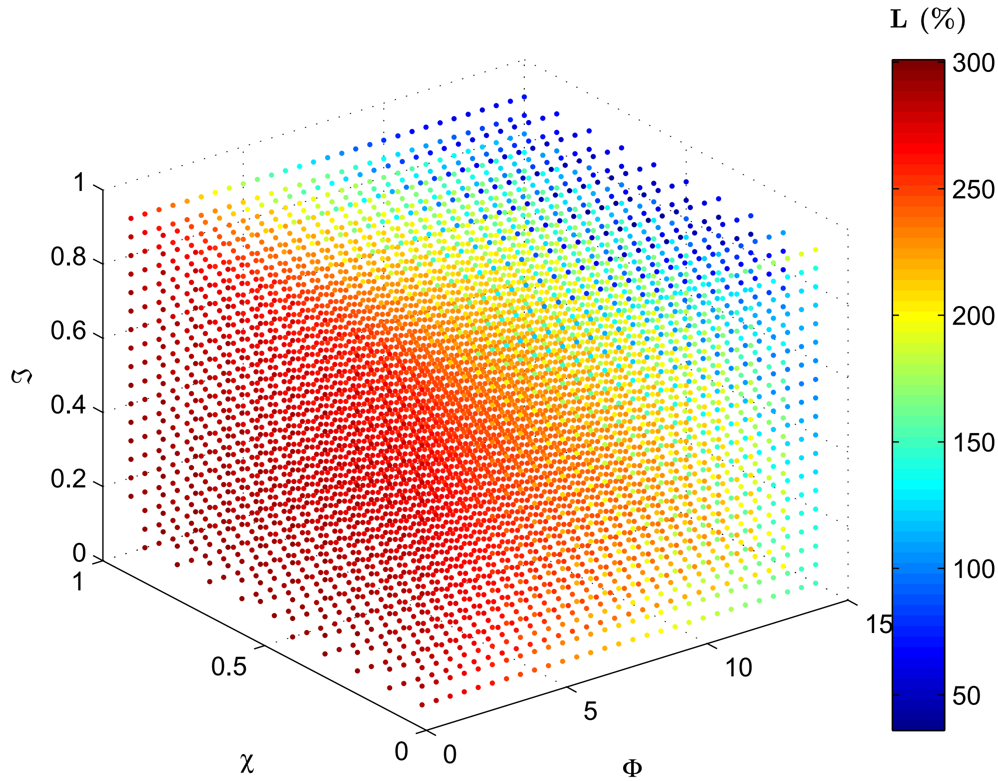

Figure 4.14: Schematic representation of the solution space in 3D. For each grid point represents a fix value of χ, Φ and $\Im$ for which the error L is estimated. The minimum value of L is chosen as the best solution, which gives best fit to the measured velocities.

Vs_2. The same procedure is applied to the neighboring grid point and the error in V_p, Vs_1 and Vs_2 is estimated. Once again, let's assume that the error in Vp, Vs_1 and Vs_2 for this neighboring grid point is L_2. If the error at the neighboring grid point L_2 is less than the error at the first point (L_1), then L_2 becomes the reference error for the further calculation. But if L_2 is larger than the L_1 then the reference error does not change and the calculation proceeds to the next neighboring grid point, ignoring the first neighboring grid point (L_2). The minimum value of L is found after an exhaustive search.

Because the inverse modeling solutions are non-unique, many solutions may result in the same error estimate. Information about the microfabric helps to constrain the modeling parameters. For example the examination of microfabrics of the shale

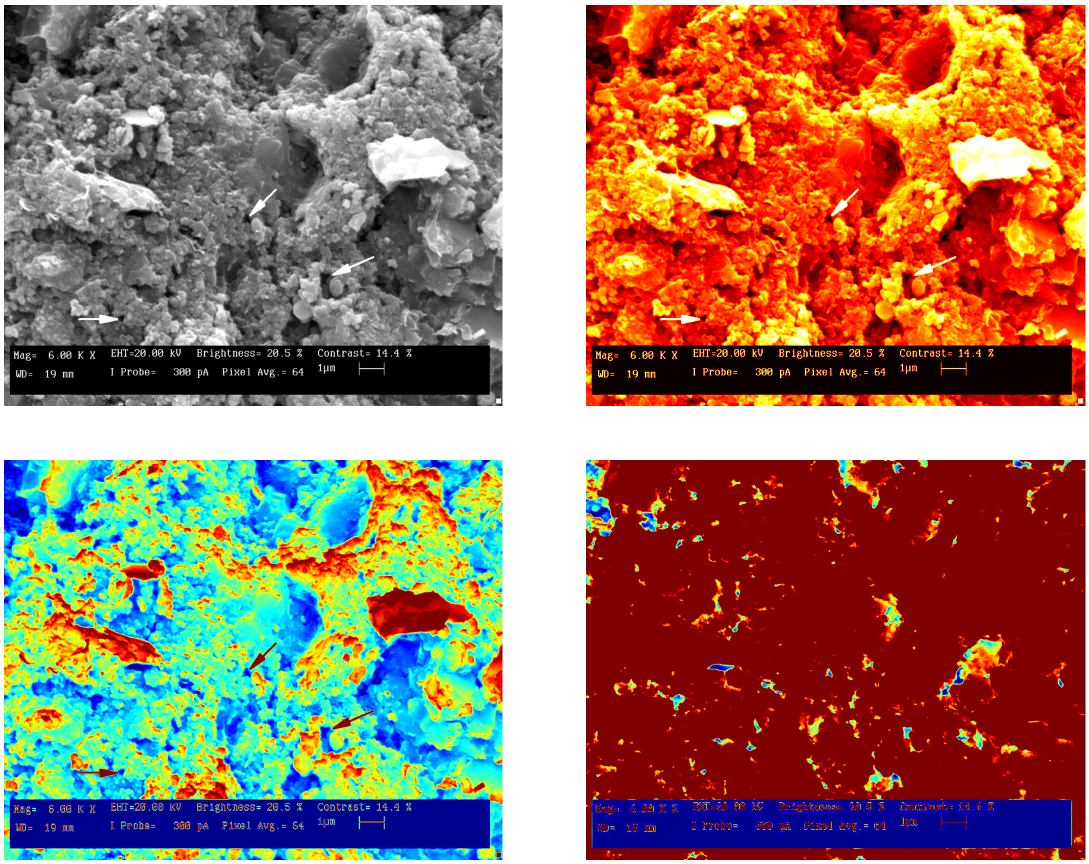

Figure 4.15: SEM microphotograph and its processed image highlight the microstructure of shale. The arrows are pointing to the shape of pores and their random distribution. A preferred alignment in cracks and minerals is not observed.

that in SEM photomicrographs shown in Figures 4.13 and 4.14 shows that cracks in Figure 4.13 have comparatively a larger aspect ratio than those in Figure 4.14. Also, it can be noticed that the cracks in Figure 4.13 are randomly distributed while in Figure 4.13 they are aligned. A rough estimate of porosity can also be estimated by analyzing the surface area of the pores. The pore surface area in shale in Figure 4.13 is clearly larger than in Figure 4.14. This information about the microstructure of shale is used to constrain the inverse modeling solutions.

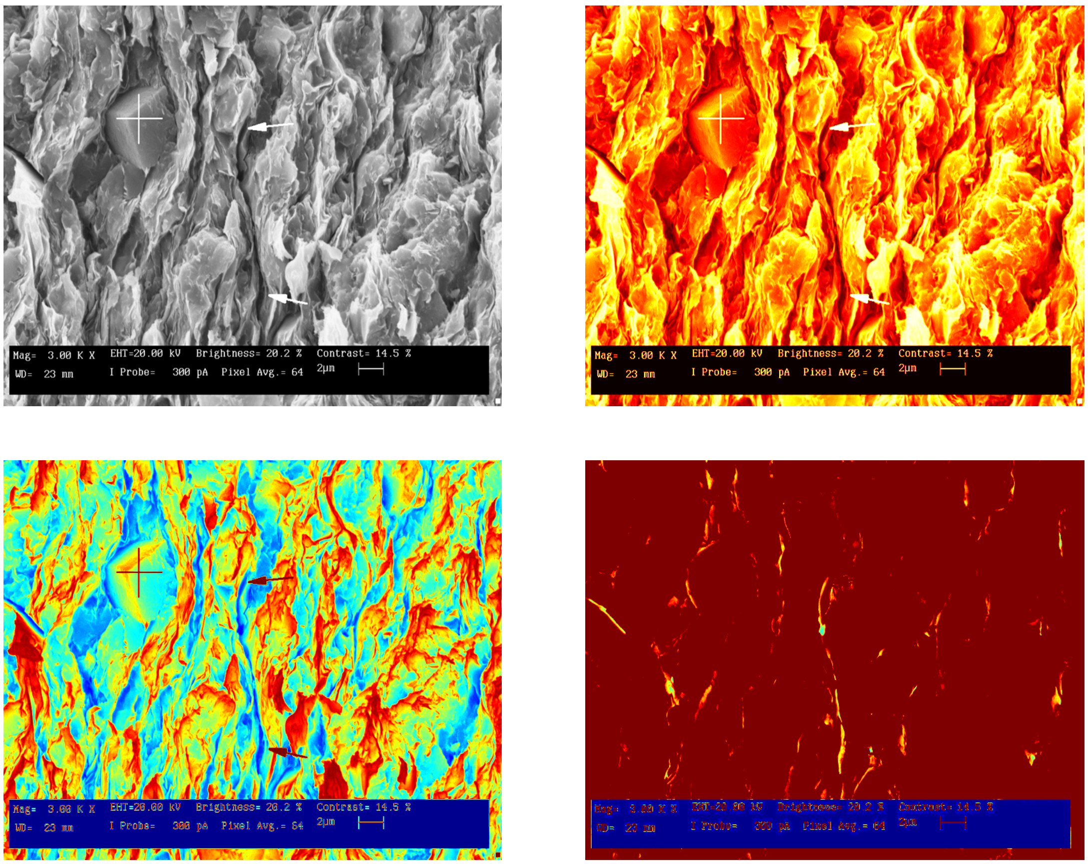

Figure 4.16: SEM microphotograph and its processed image highlight the microstructure of shale. The arrows are pointing to thin cracks and their orientation. A preferred alignment in cracks and minerals is observed.

A summary of the best solution, with information about aspect ratio of the crack, crack-induced porosity, and friability for each of the nine facies, is shown in Table

4.5 and 4.6. These tables also summarize the error estimate in the velocities in the theoretical and measured results. The percentage error shown in Table 4.5 and 4.6 are for the mineral assemblages, estimated using XRD and FTIR respectively. The FTIR based mineral assemblage give, overall, a better estimate of the velocities compared to the XRD. The maximum error in measured velocities and theoretical velocities is 22% for the FTIR-based mineral assemblage. But for most of the facies this error is even less than 8% in most of the directions, except Vs_v along 45^0, which is relatively more difficult to measure in the lab at room temperature and pressure. The largest error is observed in the shale sample from phosphatic deposit facies. For the calcareous mudstone, limy mudstone and wavy-bed deposit facies XRD-based mineral assemblage gives a better estimate of velocities than FTIR, but in the rest of the facies FTIR prevails. This can be attributed to the differences in the determination of weight percentage of quartz and clay minerals in the samples.

4.8 Sources of Error

There are many sources of error that can magnify the total estimate of percentage error in both lab-measured and theoretically-estimated elastic velocities. The theory assumes single aspect ratio and ellipsoidal cracks in the shale, which is obviously not true in nature. Other than the theoretical assumptions, some of the obvious sources of error are possible during:

- the estimation of the mineral assemblage of the rock sample,
- ultrasonic velocity measurement in the lab,

Table 4.5: Error estimate (in percentage) between velocity estimated from minerals assemblage using forward modeling and the velocity measured in laboratory at ultrasonic frequency (1 MHz). The information of the shale microstructure, such as crack induced porosity (Φ), the aspect ratio of cracks (χ) and the friability ($\Im$) is calculated using inverse modeling. The cracks filled by water (w) and gas (g) are indicated. Mineralogy from X-ray Diffraction.

Facies Name	V_p			Vs_h			Vs_v			$\Phi(\%)$	χ	$\Im$	
	0^0	45^0	90^0	0^0	45^0	90^0	0^0	45^0	90^0				
Calcareous Mudstone	5.96	7.81	8.49	1.45	7.55	8.30	1.45	21.24	5.96	12	0.2	0.8	w
Limy Mudstone	1.93	5.60	4.72	7.66	8.65	7.34	7.67	15.40	6.69	12	0.5	0.8	g
Wavy-bed Deposit	0.18	0.27	0.80	1.13	1.22	0.08	1.13	1.92	3.70	8	0.5	0.8	g
Dolomitic Mudstone	14.06	8.18	4.68	9.89	0.21	9.72	9.89	1.20	8.85	5.5	1.0	0.7	g
Fossils-rich Deposit	6.64	3.45	1.56	8.99	9.47	8.71	8.99	11.73	8.20	6.5	1.0	0.79	g
Concretion	17.88	15.20	3.11	11.55	6.04	2.86	11.55	4.18	12.06	5	1.0	0.77	g
Non-calcareous	8.90	10.04	14.12	12.57	15.53	15.73	12.57	11.57	8.95	10	0.2	0.8	g
Calcareous Laminae	13.15	8.03	0.63	6.64	1.11	6.80	6.64	1.68	7.12	4	1.0	0.73	g
Phosphatic Deposit	10.42	13.92	17.02	7.99	15.19	17.31	7.99	29.68	4.88	10	0.2	0.8	w

Table 4.6: Error estimate (in percentage) between velocity estimated from minerals assemblage using forward modeling and the velocity measured in laboratory at ultrasonic frequency (1 MHz). The information of the shale microstructure, such as crack induced porosity (Φ), the aspect ratio of cracks (χ) and the friability ($\Im$) is calculated using inverse modeling. The cracks filled by water (w) and gas (g) are indicated. Mineralogy from FTIR.

Facies Name	V_p			Vs_h			Vs_v			$\Phi(\%)$	χ	$\Im$	
	0^0	45^0	90^0	0^0	45^0	90^0	0^0	45^0	90^0				
Calcareous Mudstone	7.13	8.74	9.36	1.73	7.62	8.29	1.73	21.67	5.66	12	0.2	0.8	w
Limy Mudstone	2.38	6.06	5.09	7.72	8.87	7.54	7.72	15.63	6.94	12	0.5	0.8	g
Wavy-bed Deposit	0.56	5.41	1.80	2.65	0.65	0.02	2.65	2.34	5.18	9	0.5	0.8	g
Dolomitic Mudstone	6.54	3.55	5.14	2.40	2.53	8.94	2.40	4.36	2.56	5.5	1.0	0.7	g
Fossils-rich Deposit	0.38	0.39	3.25	2.13	3.14	5.84	2.13	5.34	3.03	6.5	1.0	0.79	g
Concretion	6.1	7.67	3.44	0.36	0.51	3.03	0.37	1.49	0.07	5	1.0	0.77	g
Non-calcareous	2.37	8.30	14.16	5.33	10.74	12.0	5.33	5.36	1.40	10	0.2	0.8	g
Calcareous Laminae	4.55	2.0	0.69	3.47	0.27	2.87	3.47	0.59	4.09	4	1.0	0.73	g
Phosphatic Deposit	8.46	13.63	17.54	5.03	14.38	17.37	5.03	16.44	1.81	10	0.2	0.8	w

- sample preparation, and
- theoretical modeling due to unavailability of elastic constants for each minerals present in the rock, i.e., for various types of quartz.

4.9 Summary

The quantitative analysis of the shale microstructure is extremely helpful for reservoir characterization because the aspect ratio of the cracks and the total porosity would be asset for reservoir expoitation. Based on ultrasonic velocity measurement the Barnett Shale can be classified into five distinct seismic facies. The information about pore geometry is the average over a wide range of crack aspect ratios. The mineralogy-based estimate of elastic constants provides good results for most of the groups, which can be used to estimate velocities when they are not directly measured. If information about the microstructure is available, such as from thin section and SEM microphotograph analysis, to constrain the inverse modeling results, the mineralogy based velocity estimate can be very close to the measured velocity.

Chapter 5

Comparison of Upscaling Sonic to Seismic Velocity Methods

In contrast to the new contributions in modeling and measurements presented in Chapter 2 through 4, the present chapter uses established methods to compare differences in upscaling of seismic wave sonic log to surface seismic frequencies. The elastic properties of heterogeneous media are frequency dependent because of multiple scattering during seismic wave propagation (Mavko et al., 1998; Mukerji et al., 1995). Three different methods of upscaling to upscale the reservoir properties are analyzed involving wave propagation in heterogeneous media. The theoretical formulations to estimate effective elastic constants at a lower frequency from high frequency data are based on the solution of the wave equation in heterogeneous media. simple averaging (static), Backus averaging (quasi-static), and averaging based on pair-correlation (dynamic) are compared. A variable-size running window approach is adopted to estimate the elastic properties at a smaller scale. The size of the window is a function of velocity and frequency, and it is assumed that the medium inside the window is statistically homogeneous. The difference in the results obtained by three theoretical models in surface seismic frequency bandwidth (50-100 Hz) will be shown to be ~2000 ft/s for P-wave and ~800 ft/s for S- wave velocity.

5.1 Introduction

Upscaling of the Earth's heterogeneous properties is a mathematical process of obtaining, or predicting, the elastic properties of the rock at lower frequencies, from available measurements at higher frequencies. Upscaling of heterogeneous media generally simplify the Earth's model without changing the overall seismic wavefield during wave propagation (Gold et al., 2000). Generally, there are two types of data available to geoscientists to carry out reservoir characterization: dynamic and static. In the dynamic case we obtain data via ultrasonic lab measurements, wireline log, VSP (vertical seismic profiling), crosswell seismic, and surface seismic, with each of these measurements operating in a different frequency range. Calculations of components of the elasticity tensors using the mineralogical assemblage and elastic moduli using microindentation technique are called static measurements. In dynamic measurements, when the wavelength is comparable to the size of the heterogeneity, one can observe different values of any physical property at different frequencies (i.e., Vp at ultrasonic and seismic frequencies), and therefore, we need a rigorous procedure of upscaling to predict rock elastic properties at frequencies lower than the measured frequency. According to Grubb and Walden (1995) upscaling of the random heterogeneous media basically smooths the elastic properties and is often needed for seismic imaging or forward modeling. Because of high frequency approximation, the application of ray tracing can be valid only for media in which the spatial fluctuation in properties is larger than the wavelength (Cerveny et al., 1977). In a practical sense, upscaling means the replacement of a heterogeneous volume with a homogeneous volume with effectively equivalent elastic constants. Heterogeneity

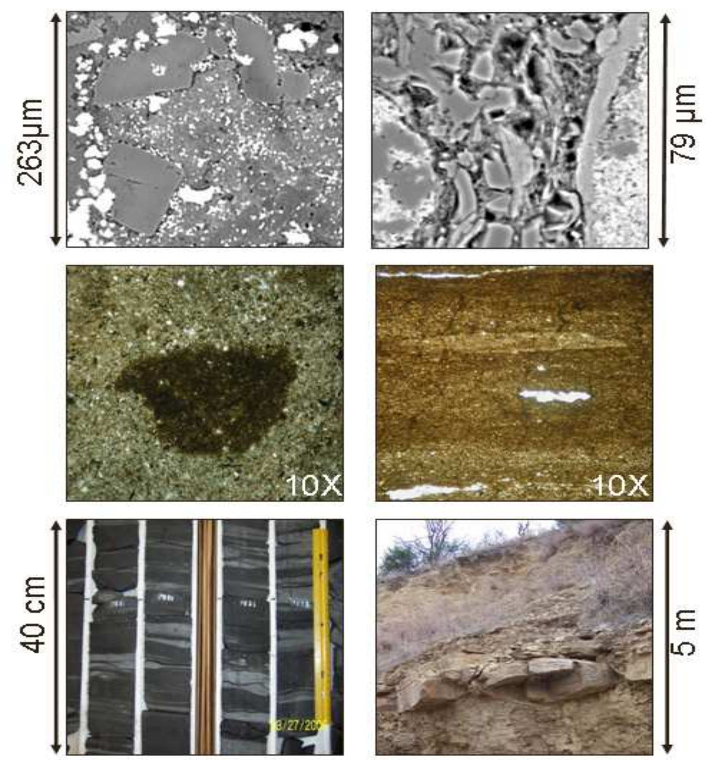

Figure 5.1: Random heterogeneous media with the size of heterogeneities ranging from a micro-scale to outcrop scale. Electron microprobe photo (top row), transmitted light microphotograph (middle row), and core and outcrop photograph (bottom row, left to right, respectively).

occurs at many scales, from pore scale to reservoir scale (Figure 5.1). The fine scale variation in the model's parameters significantly affects the coarse scale properties of the solution (Moulton et al., 1998). Geophysicists focus on coarse scale; hence, upscaling of the fine scale media is required in order to give the effective medium properties on a coarse scale that capture the influence of fine scale structures.

Theoretical estimation of effective moduli of elastic or viscoelastic material generally requires information about (1) elastic moduli of each component of material, (2) volume fraction of each component, (3) spatial distribution function of each component, (4) porosity of material, (5) geometrical orientation of each component, (6) viscosity of the fluid, and (7) measurement frequency (Mavko et al., 1998; Vikhorev et al., 2006). Of all these types of information, estimation of the exact volume fraction and geometrical details of each component is the most difficult. If we do not have information about the geometrical details of how the components are arranged relative to each other, the best we can do is to predict the upper and lower bounds of a composites (Mavko et al., 1998). The most famous bounds are the Voigt, Reuss, and Hashin-Shtrikman bounds. Though the Hashin-Shtrikman bounds are initially formulated for isotropic elastic composite, they can be generalized to include the anisotropic phase and may incorporate some porosity dependence (Hasin and Shtrikman, 1962). The Voigt (1928) average represents the upper bound of elastic properties and is based on the concept of isostrain. When a stress is applied to a stack of materials, all materials deform by the same amount. The displacement in one material is exactly equal to the displacement in another material and can be expressed mathematically by the arithmetic mean [$\varepsilon(x) = \langle\varepsilon\rangle = constant$]. The Voight average means the strain in each component is equal to the average volumetric strain. The Reuss (1929) average represents the lower bound and is based on the isostress concept that states that if all the stresses are equal then the strains can not be equal. This can be expressed mathematically by arithmetic the mean

$[\sigma(x) = \langle\sigma\rangle = constant]$ In this case the effective compliance will be equal to the average compliance, $S^* = \langle S\rangle$.

The Brown (1955) model calculates the effective dielectric constant in a macroscopically homogeneous and isotropic composite having only two types of material, where the volume fraction and the material's property of each individual are known. Hasin and Shtrikman (1962) extended this study to calculate effective permeability of a multiphase composite in the form of upper and lower bounds if the volume fraction and the material properties of each phase are known. The Wood (1955) formulation provides the estimate of effective velocity in the case of a fluid mixture in which the heterogeneities are small compared to the wavelength. A different class of models that requires detailed information on pore structure and micro geometry is discussed by O'Connell and Budiansky (1974), Kuster and Toksoz (1974), and Xu and White (1995). In the self-consistent approximation (O'Connell and Budiansky, 1974), the first step is to calculate the property of the material with no inclusion, and then in the second step calculate the effective material with one inclusion. In the case of higher concentrations, the calculation of effective properties takes place in steps. The effective properties obtained after the first step become the starting media for the second step, and so on. Therefore, this theory does not account for the interaction among the inclusions. Kuster and Toksoz (1974) used a long wavelength first-order scattering theory to estimate P- and S- wave velocities. Their formulation takes into account a two-phase material with a single type of inclusion imbedded within the groundmass, where a separate term in the summation should be included for the inclusion different from the first one. The Xu and White (1995) sand-clay model uses a differential effective medium (DEM) scheme to avoid the dilute concentration restriction by adding a small concentration of pores and cracks.

There are several approaches, analytical as well as numerical, to upscale heterogeneous elastic and viscoelastic media. I will only focus on the upscaling methods of elastic media. These different approaches result in different physical properties of the media. Tiwary et al. (2007a) compare four upscaling methods based on completely different physical considerations. The results show large variation in upscaled properties estimates for P- and S-wave.

5.2 Causes of Frequency Dependence

The causes for frequency-dependent reservoir properties can be classified into the following three main categories:

(a) Static scale effect: The physical properties of the medium depends on the scale of investigation. A change in the scale of measurement would lead to a change in the intrinsic reservoir properties (Figure 5.2 a).

(b) Elastic scattering: Due to the presence of heterogeneities, or change in the contrast of the medium, some wave energy bounces off in other directions and does not reach the receiver resulting in lowering the transmitted amplitude (Figure 5.2 b). When the seismic wavelength is comparable to the size of the heterogeneity, medium, it reflects back and forth losing energy at each bounce. The greater the contrast between the host rock and the heterogeneities, the more energy is scattered and thus lost.

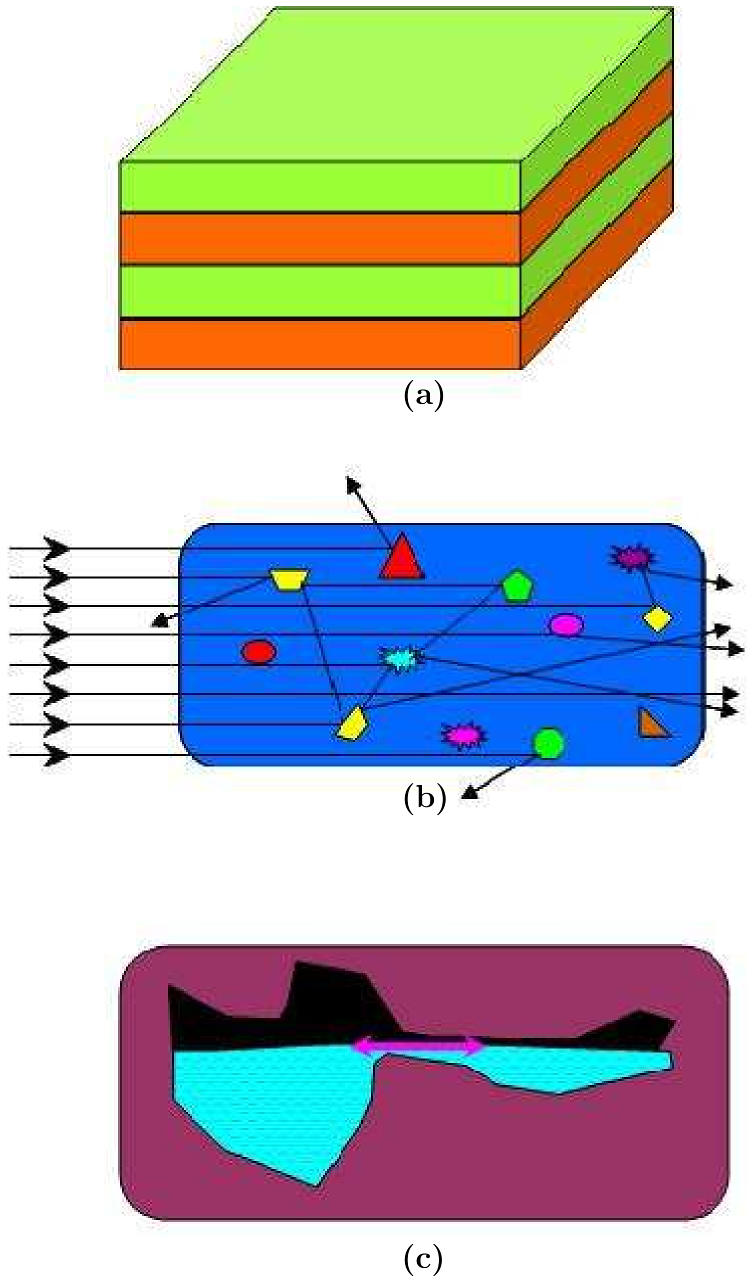

Figure 5.2: Seismic scale phenomena responsible for changing the seismic response at different frequencies: (a) static scale effect, (b) elastic scattering, and (c) intrinsic attenuation.

(c) Intrinsic attenuation: In a porous medium, where the pores are partially- or fully saturated, the propagation of the seismic wave creates a pressure disequilibrium in the rock. This pressure disequilibrium initiates a relative displacement between the grain framework and the pore fluid. If the time period of the seismic wave is not sufficient to let the pressure equilibrate, the seismic waves loses energy (Figure 5.2c). Also, some of the energy is lost due to conversion of seismic energy into heat energy.

These processes of attenuation are often coupled, and therefore the quantitative estimation of their isolated effect on attenuation can be extremely difficult. In this chapter, it will be assumed that the elastic scattering is the only cause of frequency dependence.

The three upscaling methods compared in this chapter are shown in Figure 5.3. These methods consider the following frequency dependence causes:

- **simple Averaging** includes the Static scale effect,
- **Backus Averaging**: includes both static scale effect and the interaction among the layers, and
- **Pair correlation function Averaging** includes the static scale effect, interaction, and the scattering.

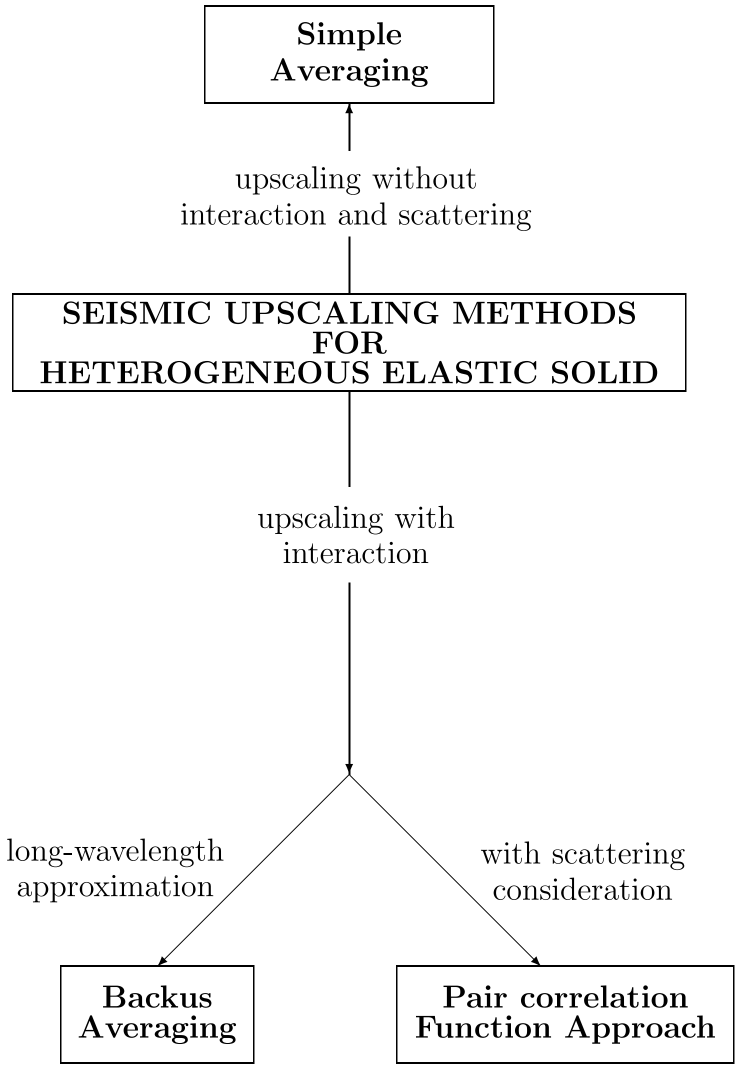

Figure 5.3: Flowchart of the physical consideration involved in mathematical formulation of different upscaling methods.

5.3 Upscaling of Thin Layered Media

5.3.1 Backus Averaging

Thin layered media[1] (Figure 5.4) has been studied widely in different branches of science (Postma, 1955; Backus, 1962; Shermergor, 1977; Berryman, 1979). A stack of thin isotropic layers will give rise to the medium called transversely isotropic vertical axis of symmetry (VTI). Backus (1962) obtained the exact solution to calculate the effective properties for the VTI medium using the assumptions that all constituents

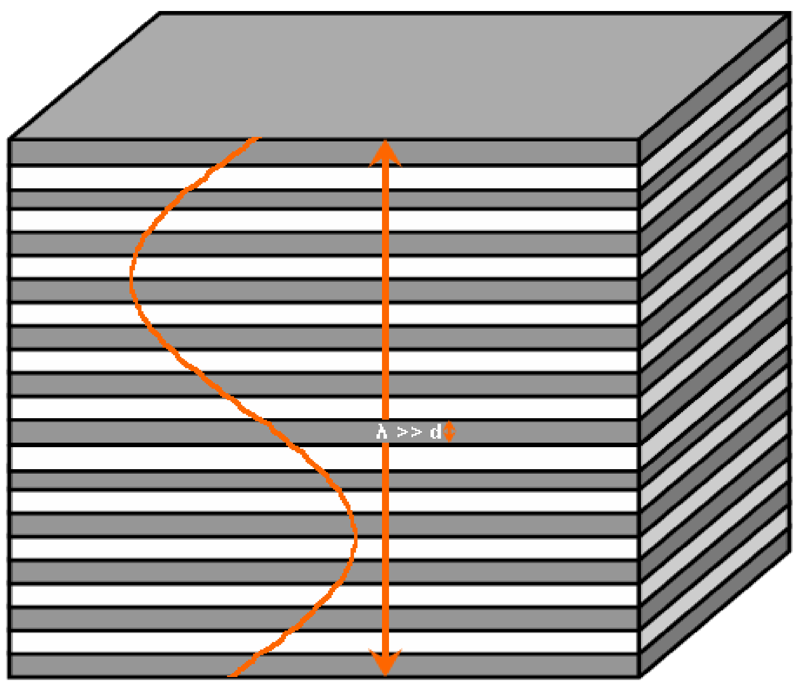

Figure 5.4: Layered medium in which the thickness of the layer (d) is much smaller than the wavelength of the seismic wave (λ).

[1] Means that the thickness of each layer is much smaller than the wavelength of the seismic waves.

of the medium are linearly elastic and there is no source of energy dissipation due to friction or viscosity. The Shermergor (1977) formulation, as expressed in equation 2.4, is valid for the more general symmetry class (orthorhombic: characterized by nine independent elastic constants), and it can be used to calculate the effective elastic constant in thin layered media even if the layers are anisotropic. If these anisotropic layers are replaced by isotropic layers, Shermergor's (1977) formulation reduces to the formulae derived by Backus (1962) and Rytov (1956) for thin layered media with isotropic layers. The resulting medium exhibits transversely isotropic properties with a vertical axis of symmetry.

$$
\begin{aligned}
C_{11}^{*} &= \langle C_{11}\rangle + \left\langle \frac{C_{13}}{C_{33}} \right\rangle^{2} \left\langle C_{33}^{-1} \right\rangle^{-1} - \left\langle \frac{C_{13}^{2}}{C_{33}} \right\rangle, \\
C_{12}^{*} &= \langle C_{12}\rangle + \left\langle \frac{C_{13}}{C_{33}} \right\rangle \left\langle \frac{C_{23}}{C_{33}} \right\rangle \left\langle C_{33}^{-1} \right\rangle^{-1} - \left\langle \frac{C_{13}C_{23}}{C_{33}} \right\rangle \\
C_{13}^{*} &= \left\langle \frac{C_{13}}{C_{33}} \right\rangle \left\langle C_{33}^{-1} \right\rangle^{-1}, \\
C_{22}^{*} &= \langle C_{22}\rangle + \left\langle \frac{C_{23}}{C_{33}} \right\rangle^{2} \left\langle C_{33}^{-1} \right\rangle^{-1} - \left\langle \frac{C_{23}^{2}}{C_{33}} \right\rangle, \\
C_{23}^{*} &= \left\langle \frac{C_{13}}{C_{33}} \right\rangle \left\langle C_{33}^{-1} \right\rangle^{-1}, \\
C_{33}^{*} &= \left\langle C_{33}^{-1} \right\rangle^{-1}, \\
C_{44}^{*} &= \left\langle C_{44}^{-1} \right\rangle^{-1}, \\
C_{55}^{*} &= \left\langle C_{55}^{-1} \right\rangle^{-1}, \\
C_{66}^{*} &= \left\langle C_{66} \right\rangle, \qquad (5.1)
\end{aligned}
$$

where $C_{ij}(i, j = 1, 2, 3, ...6)$ represent the effective elastic constants in two-index Voigt notation and C_{ij}^{*} represent the effective elastic constants over the scale of the averaging window length. The angular bracket, $\langle\ \rangle$, is an integral over the size of the window (Liner and Fei, 2007).

The Rytov (1956) solution of the wave equation to estimate effective behavior of the long wave in periodic layered media is based on the Floquet theorem (Floquet, 1883). Equation 5.1 can be considered to be a generalization of the widely Backus approach for anisotropic (orthotropic [1]) layers. Attenuation and dispersion are the results of multiple scattering at the layer interfaces as well as at the heterogeneities present in the medium. Friendly multiples cause large transmission loss while a wave travels through thin layered medium due to stratigraphic filtering (Anstey and O'Doherty, 2002). Backus (1962) long wavelength approximation does not the effect of multiple scattering. The upscaling results of Backus averaging for P-wave and S-wave are shown in Figures 5.5 and 5.6, respectively. The sonic log data show a large fluctuation in P- wave and S- wave velocities. These fluctuation decreases at the lower frequencies. At $50Hz$ the P- wave and S- wave velocity log show the minimum fluctuation. Beyond this point the upscaled velocity log losses resolution.

[1] includes orthorhombic, hexagonal, cubic, and isotropic symmetry

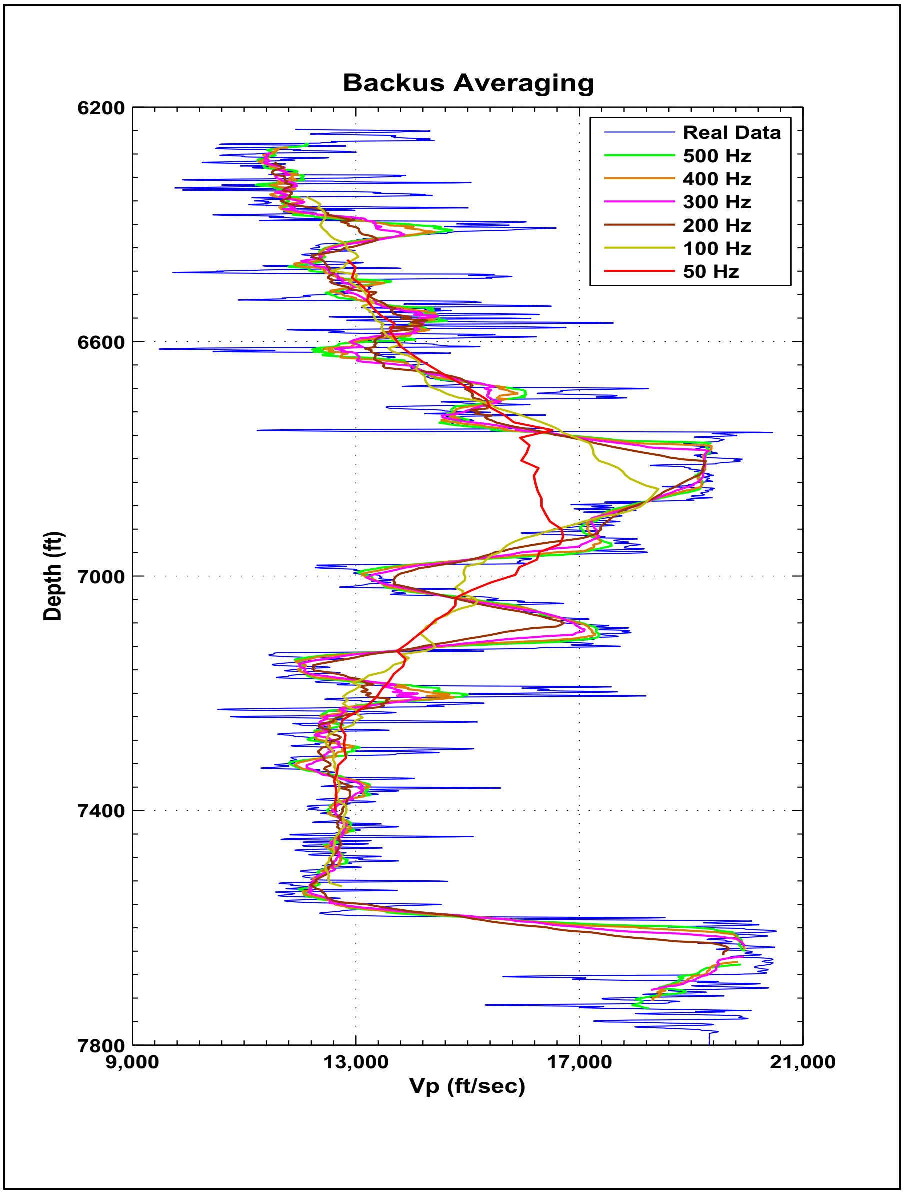

Figure 5.5: Color coded upscaling results of P-wave at various frequencies using the Backus averaging method. P-wave velocity from the sonic log is used for upscaling. The high frequency real data show large fluctuation of velocity with depth. The upscaling result shows smoothing of the fluctuations.

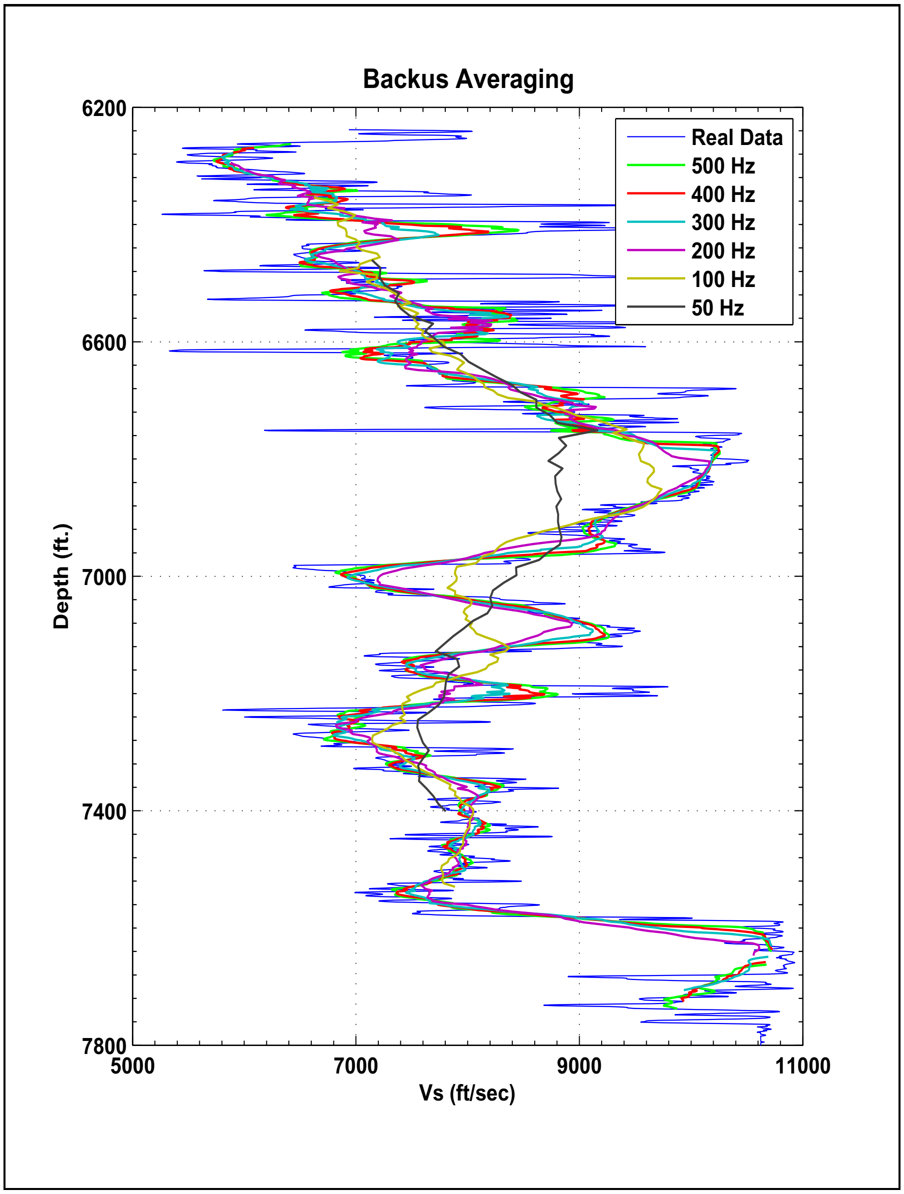

Figure 5.6: Color coded upscaling results of shear wave at various frequencies using the Backus averaging method. S-wave velocity from the sonic log is used for upscaling. The high frequency real data show large fluctuation of velocity along the depth. The upscaling result shows smoothing of the fluctuations.

5.4 Simple Running Averaging

In simple averaging, the reservoir properties are averaged over a window for which the length is equal to the size of the wavelength at a given frequency, since the velocity at a higher frequency is known from the well log. It is assumed that the property of the medium inside the window is statistically homogeneous, thin layered, and either isotropic or anisotropic. The window is applied through the sonic or density log and the arithmetic average of all the data points falling inside the window is computed and assigned to the window center. As the window moves down, the process continues as shown in Figure 5.7. This process results in a continuous lower frequency curve with the output frequency dependent on the window size. The calculation of effective elastic constants (C_{ij}) is performed using equation 5.2. The two-index Voigt notation is used for the stiffness tensors C_{ij}. The averaging of stiffness tensors is estimated, and then the V_p, V_s, and density are calculated using equation 5.2 and 5.4.

$$C^*_{ij}(H) = \Big\langle C_{ij} \Big\rangle \Big|_L, \qquad and \qquad \rho^*(H) = \langle \rho \rangle \Big|_L \tag{5.2}$$

where, L is the length of the averaging window, H is any subsurface point representing the depth at which the effective value has been calculated, and C^*_{ij} $(i, j = 1, 2, 3, ...6)$ represents the components stiffness tensor of effective elastic constant [in two-index Voigt notation (Musgrave, 1970)].

For example, the average value of C_{11} is

$$\langle C_{11} \rangle = \frac{1}{N_L} \sum_{i=1}^{N_L} C_{11}^{(i)} \ , \tag{5.3}$$

where, $\frac{1}{N_L}$ is the number of measured points that fall within the chosen window of size, L.

Once the value of the components of the stiffness tensor are known, the elastic properties of the medium can be estimated using as

$$V_p^* = \sqrt{\frac{C_{33}^*}{\rho^*}} \ , \qquad V_{S1}^* = \sqrt{\frac{C_{44}^*}{\rho^*}} \ , \quad \mathit{and} \quad V_{S2}^* = \sqrt{\frac{C_{55}^*}{\rho^*}} \ . \tag{5.4}$$

The calculated V_p, V_s, and density using simple averaging is shown in Figures (5.8, 5.9, and 5.10).

Simple averaging take the arithmetic mean of C_{ij} and ρ while making calculation of the effective elastic media. Like Backus averaging, simple averaging does not take into account the scattering attenuation that can take place due to heterogeneities of different sizes present in the medium. The difference between Backus averaging and simple averaging is that Backus averaging accounts for the interactions, while simple averaging is just the arithmetic mean.

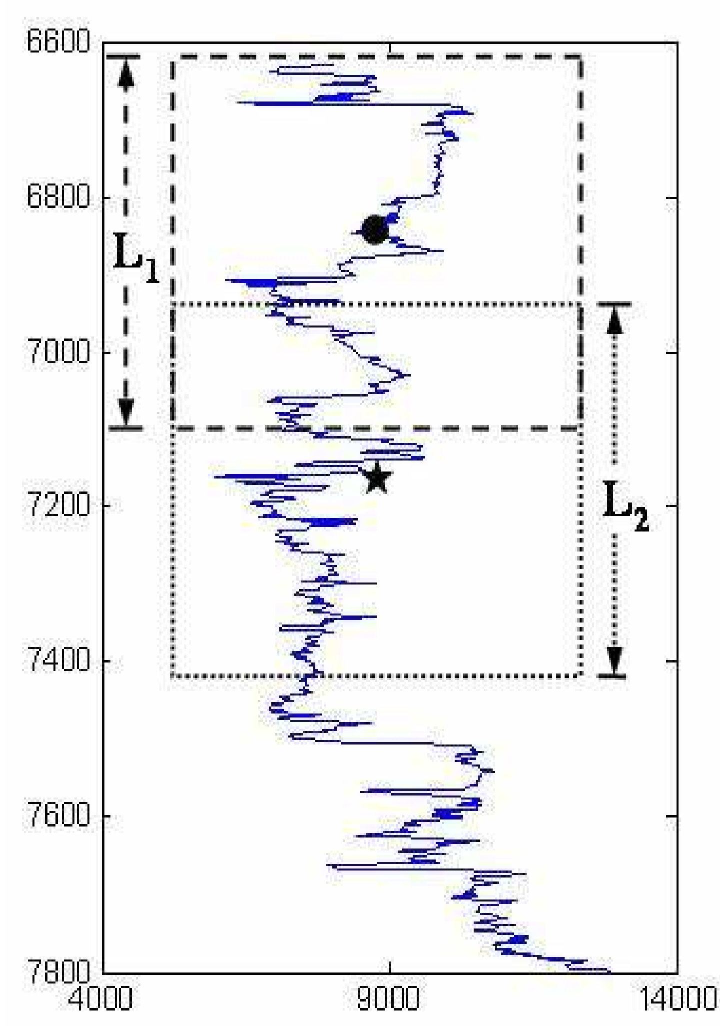

Figure 5.7: Schematic representation of running window concept: the averaged property inside the dashed window of length L1 is shown by dark solid circle. Then the window moves downward to next location represented by dotted window where the length of the window is L2 and the averaged property inside this window is shown by dark star.

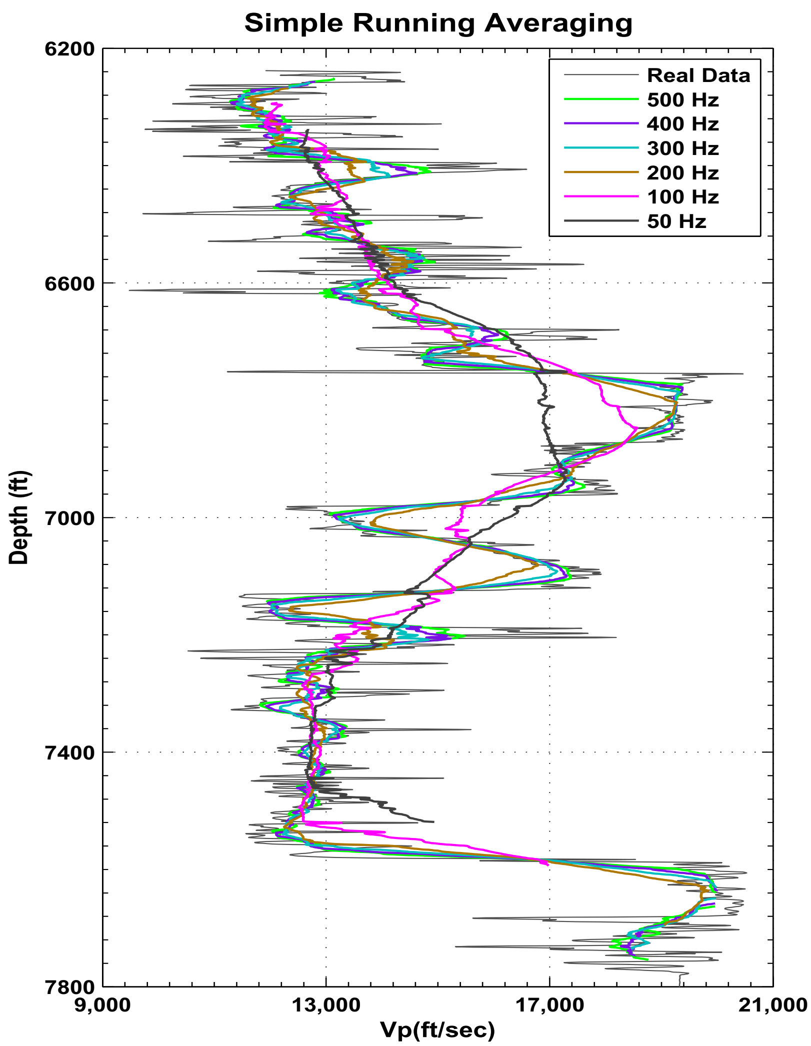

Figure 5.8: Color coded upscaling results of P-wave at various frequencies using simple averaging method. P-wave velocity from the sonic log is used for upscaling. The high frequency real data show large fluctuation of velocity with depth. The upscaling result shows smoothing of the fluctuations.

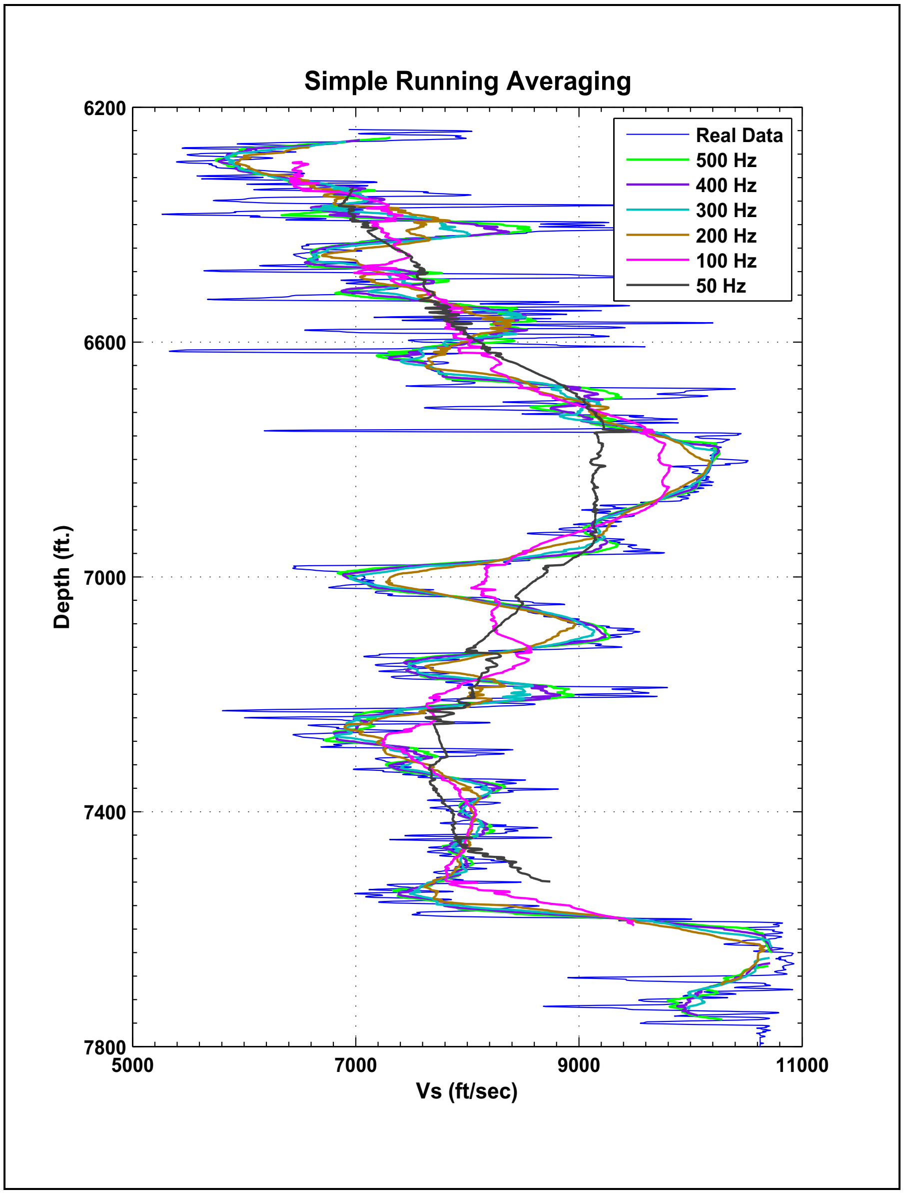

Figure 5.9: Color coded upscaling results of shear wave at various frequencies using simple averaging method. S-wave velocity from the sonic log is used for upscaling. The high frequency real data show large fluctuation of velocity along the depth. The upscaling result shows smoothing of the fluctuations and decreasing velocity at a lower frequencies.

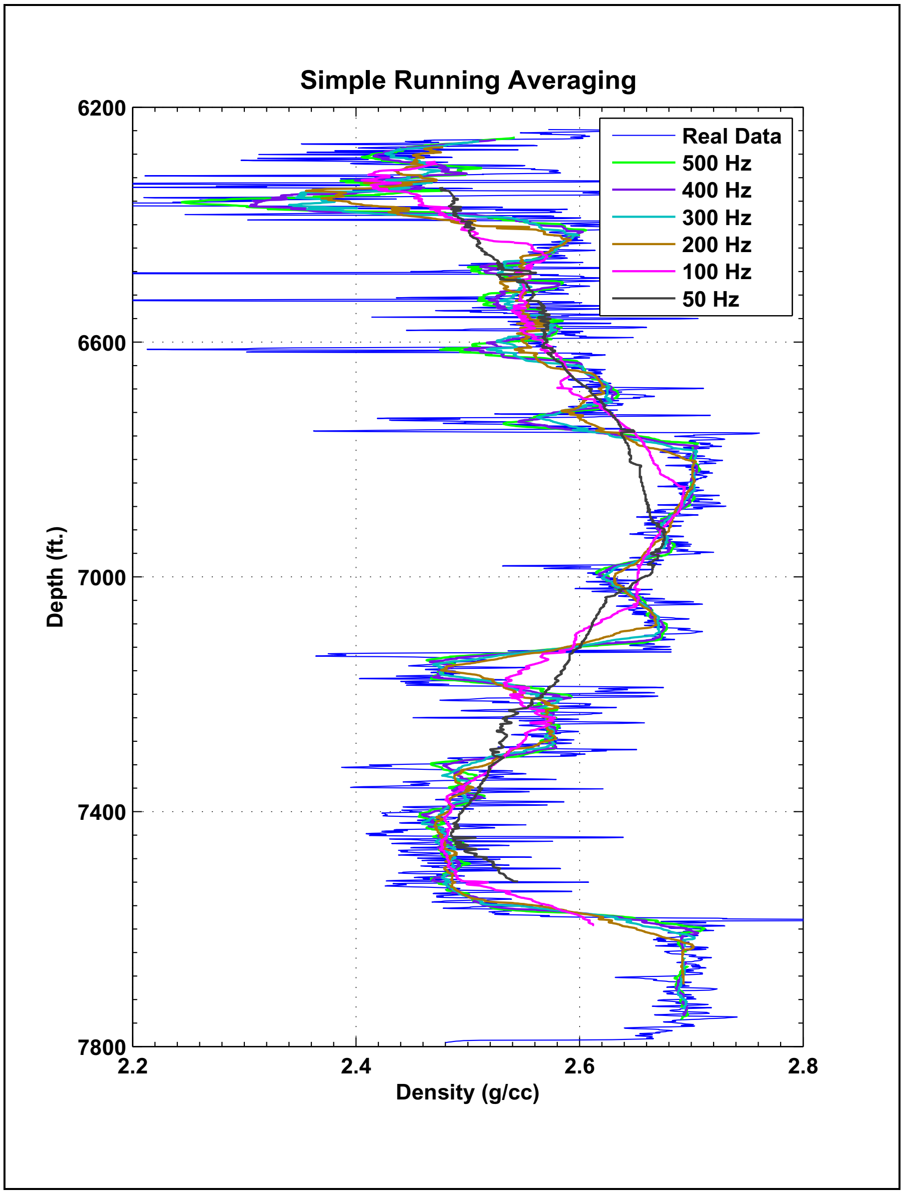

Figure 5.10: Color coded upscaling results of density at various frequencies using simple averaging method. The real high frequency density log is used for upscaling. The high frequency real data show large fluctuation of velocity along the depth. The upscaling result shows smoothing of the fluctuations and decreasing velocity at a lower frequencies.

5.5 Many Body Problem

> "It would indeed be remarkable if Nature fortified herself against further advances in knowledge behind the analytical difficulties of the many-body problem." — Max Born (1960)

In multi-scale heterogeneous media (Figure 5.1), seismic waves can be multiply scattered. Seismic waves at a frequency bandwidth commonly used for hydrocarbon exploration attenuate because of both intrinsic and elastic scattering. The phenomena of elastic scattering in a heterogeneous medium can be simulated as a many-body system developed for quantum wave field theory (Joachian, 1975). Green's function in a multiple scattering system can be estimated using the Dyson series. Green's function techniques are powerful tools for studying many-body systems in which the main wave field will be affected by the interaction of strain field due to heterogeneities during wave propagation. The central point in this method is the Dyson's equation which determines, through an approximation of the self-energy, the Green's function of a heterogeneous medium.

Chesnokov et al. (1995) considered first order interactions to calculate the Green's function by summing the first two terms (pair correlation) of the Dyson series. The dyson series contains infinite terms which summation is not trivial. The higher order terms are considered small enough to be ignored. The Vikhorev (2005) calculation of the Green's function in heterogeneous media accounts for higher orders of interactions called multi point correlation. Figures 5.11a and b, respectively, show the physical model that explain the interactions considered in pair correlation and multi point correlation formulation. Upscaling methods based on pair- and multi-correlation function approximation account for scattering phenomena that can take place in a many-body system. Tiwary et al. (2007a) compare four different upscaling methods and show for surface seismic frequencies that the method based on multi correlation function approximation gives higher values of the elastic properties than the method based on pair correlation function approximation. The upscaling method based on pair correlation functions is relatively new and, needs to be compared with the well-known Backus averaging.

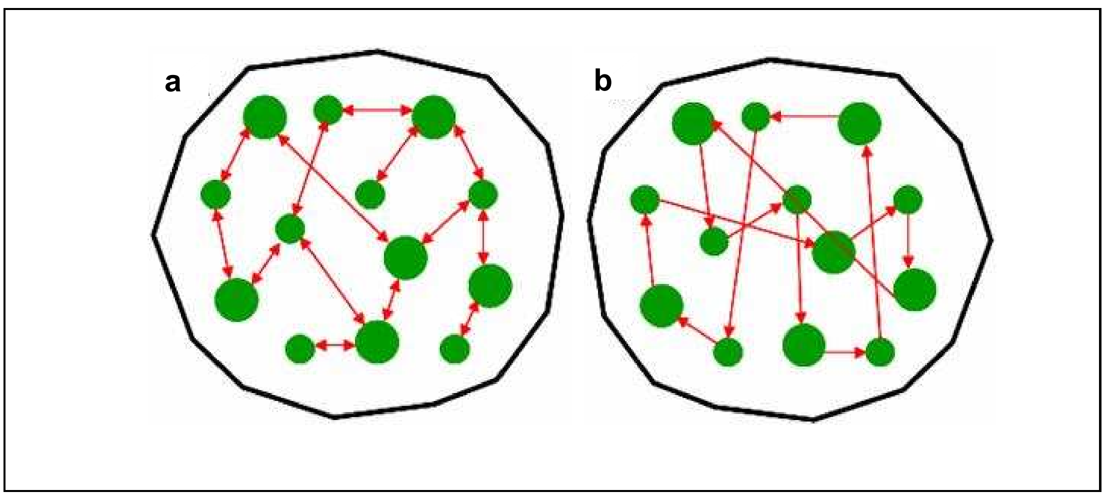

Figure 5.11: Schematic representations of random heterogeneous media, in which the green solid circles are the inclusions in the white background matrix. (a) The double ended red arrows indicate that the interaction between all pair of points in the space, and (b) the single end arrow indicates that the interactions between all the points in the space.

5.6 Correlation Function Averaging

5.6.1 Correlation Function

In a random heterogeneous media, the elastic properties of the medium varies spatially. In this case stiffness tensors, C_{ijkl}), stress, σ_{ij}, strain, ε_{kl}, and density, ρ are not constant but depend on the co-ordinate, $\mathbf{x}$. Therefore, the stiffness tensor stress, strain, and density can be expressed in terms of the average and the fluctuation:

$$C_{ijkl} = \langle C_{ijkl} \rangle + C^{'}_{ijkl} \ , \tag{5.5}$$

$$\sigma_{ij} = \langle \sigma_{ij} \rangle + \sigma^{'}_{ij} \ , \tag{5.6}$$

$$\varepsilon_{kl} = \langle \varepsilon_{kl} \rangle + \varepsilon^{'}_{kl} \ , \tag{5.7}$$

and

$$\rho = \langle \rho \rangle + \rho^{'} \ . \tag{5.8}$$

$\langle C_{ijkl} \rangle$, $\langle \sigma_{ij} \rangle$, $\langle \varepsilon_{kl} \rangle$ and $\langle \rho \rangle$ are the average value of stiffness tensor, stress, strain, and density respectively. $C^{'}_{ijkl}$, $\sigma^{'}_{ij}$, $\varepsilon^{'}_{kl}$, and $\rho^{'}$ represent, the fluctuation in stiffness tensor, stress, strain, and density.

It is assumed here that, at any point in space, $\mathbf{x}$, that the fluctuation of any elastic property of the medium is always smaller than its average value. Let's assume that $C^{'}_{ijkl}(\mathbf{x}_1)$ and $C^{'}_{ijkl}(\mathbf{x}_2)$ are the fluctuation in the elastic stiffness tensors at points $\mathbf{x}_1$

and $\mathbf{x}_2$ respectively. Then, the pair correlation function ($\mathbb{B}$) of the elasticity tensor components for the statistically homogeneous case can be expressed as:

$$\overset{(cc)}{\mathbb{B}}{}^{pqmn}_{ijkl}(\mathbf{x}_1 - \mathbf{x}_2) = \langle C^{'}_{ijkl}(\mathbf{x}_1) C^{'}_{pqmn}(\mathbf{x}_2)\rangle \ . \tag{5.9}$$

By the same token, if $\rho^{'}(\mathbf{x}_1)$ and $\rho^{'}(\mathbf{x}_2)$ are the fluctuation in the density at points $\mathbf{x}_1$ and $\mathbf{x}_2$ from its mean density value, then

$$\overset{(\rho\rho)}{\mathbb{B}}(\mathbf{x}_1 - \mathbf{x}_2) = \langle \rho^{'}(x_1) \rho^{'}(\mathbf{x}_2)\rangle \ . \tag{5.10}$$

The fluctuation in stiffness, $C^{'}_{ijkl}$, and density, $\rho^{'}$ is determined as the difference between the actual value at any point, $\mathbf{x}$, and the mean value averaged over a given length scale, center about $\mathbf{x}$.

5.6.2 Pair Correlation Function Averaging

Backus and simple averaging do not account for the scattering that can occur at the surface of heterogeneities and layer interfaces. The averaging based on the spatial correlation function approach incorporates the physical effects of frequency dependance which arise due to scattering during waves propagation in heterogeneous media. The pair correlation function accounts for all the interactions between each and every pair of points in space. Roy et al. (2001) used pair correlation function to upscale the elastic wave velocity assuming that the frequency dependence is only due to scattering phenomena. The theoretical formulation to calculate the frequency-dependent effective elasticity tensor and density in dispersive media is given by Shermergor (1977); Chesnokov et al. (1998, 2000) use the Feynman diagram technique to derive the theoretical model to calculate frequency dependent properties.

The pair correlation function formulation (Bayuk et al., 2003) to calculate the components of effective elastic properties is

$$C^{*}_{ijkl}(\omega,k) = \langle C_{ijkl}(\mathbf{x}) \rangle + \int \cos(k,\mathbf{x}) \left[\frac{\partial}{\partial x_n} \frac{\partial}{\partial x_q} G^{0}_{mp}(\omega,\mathbf{x}) \right] \overset{(cc)}{\mathbb{B}}{}^{pqkl}_{ijmn}(\mathbf{x}) d\mathbf{x} \ , \qquad (5.11)$$

and

$$\rho^{*}(\omega,k) = \langle \rho(\mathbf{x}) \rangle - \omega^2 \int \cos(k,\mathbf{x}) G^{0}_{ii}(\omega,\mathbf{x}) \overset{(\rho\rho)}{\mathbb{B}}(\mathbf{x}) d\mathbf{x} \ . \qquad (5.12)$$

where ω is the radial frequency, $\mathbf{k}$ is the wave number vector, $\mathbb{B}$ is the correlation function, $C^{*}_{ijkl}, (i,j,k,l = 1,2,3)$ is fourth rank effective elasticity tensor, G^{0} is the dynamic Green's function which depends on medium properties and frequency, and the superscripts cc and $\rho\rho$ denote auto-correlation function of stiffness tensors and density respectively.

Equations 5.11 and 5.12 are valid for an arbitrary anisotropic and heterogeneous media. If the medium is isotopic, G^{0} takes the form 5.13 (Bayuk et al., 2003):

$$G^{0}_{ij}(\omega,\mathbf{x}) = \frac{1}{\mathbf{x}} \left[h(\omega,\mathbf{x})\delta_{ij} + g(\omega,\mathbf{x}) \frac{x_i x_j}{\mathbf{x}^2} \right] \ , \qquad (5.13)$$

where

$$h(\omega \ \ \mathbf{x}) \ \equiv \ \frac{1}{4\pi\rho\omega^2\mathbf{x}^2} \left\{ \left[\left(1 + \frac{i\mathbf{x}\omega}{c} \right) e^{-\left(\frac{i\omega\mathbf{x}}{c}\right)} \right] \Big|_{c_t}^{c_l} + \frac{\mathbf{x}^2\omega^2}{c_t^2} e^{-\left(\frac{i\omega\mathbf{x}}{c_t}\right)} \right\} \ , \qquad (5.14)$$

and

$$g(\omega, \mathbf{x}) \equiv \frac{1}{4\pi\rho\omega^2\mathbf{x}^2}\left\{\left[3\left(1+\frac{i\mathbf{x}\omega}{c}\right)-\frac{\mathbf{x}^2\omega^2}{c^2}\right]\Bigg|_{c_t}^{c_l}\right\} \quad e^{-\left(\frac{i\omega\mathbf{x}}{c_t}\right)} \ , \tag{5.15}$$

where, c_l and c_t represent longitudinal and shear waves respectively.

The results of pair correlation averaging for P-wave and S-waves as a function of frequency are shown in Figures 5.12 and 5.13, respectively.

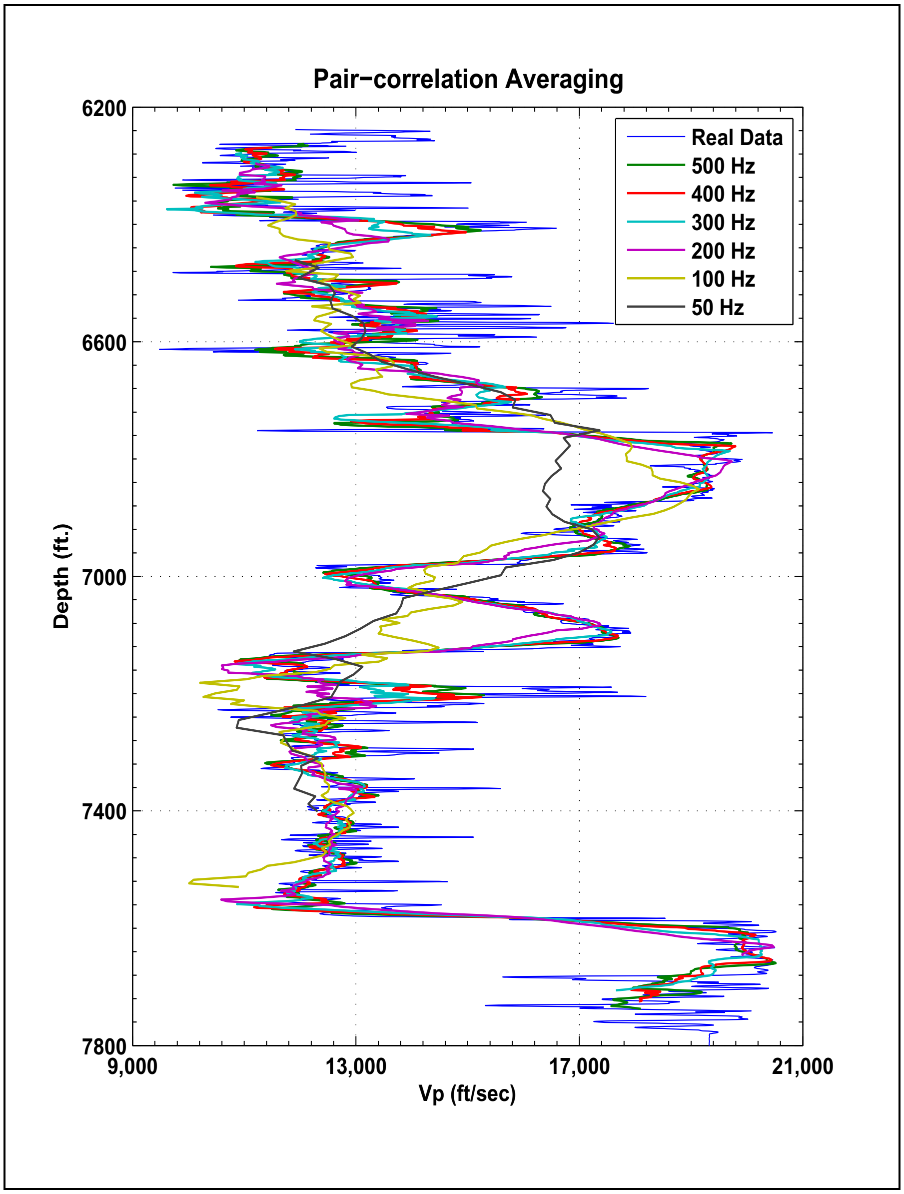

Figure 5.12: Color coded upscaling results of P-wave at various frequencies using pair correlation function averaging method. The real sonic frequency P-wave log is used for upscaling. The high frequency real data show large fluctuation of velocity along the depth. The upscaling result predicts a smoothing of the fluctuations and decreasing velocity at a lower frequencies.

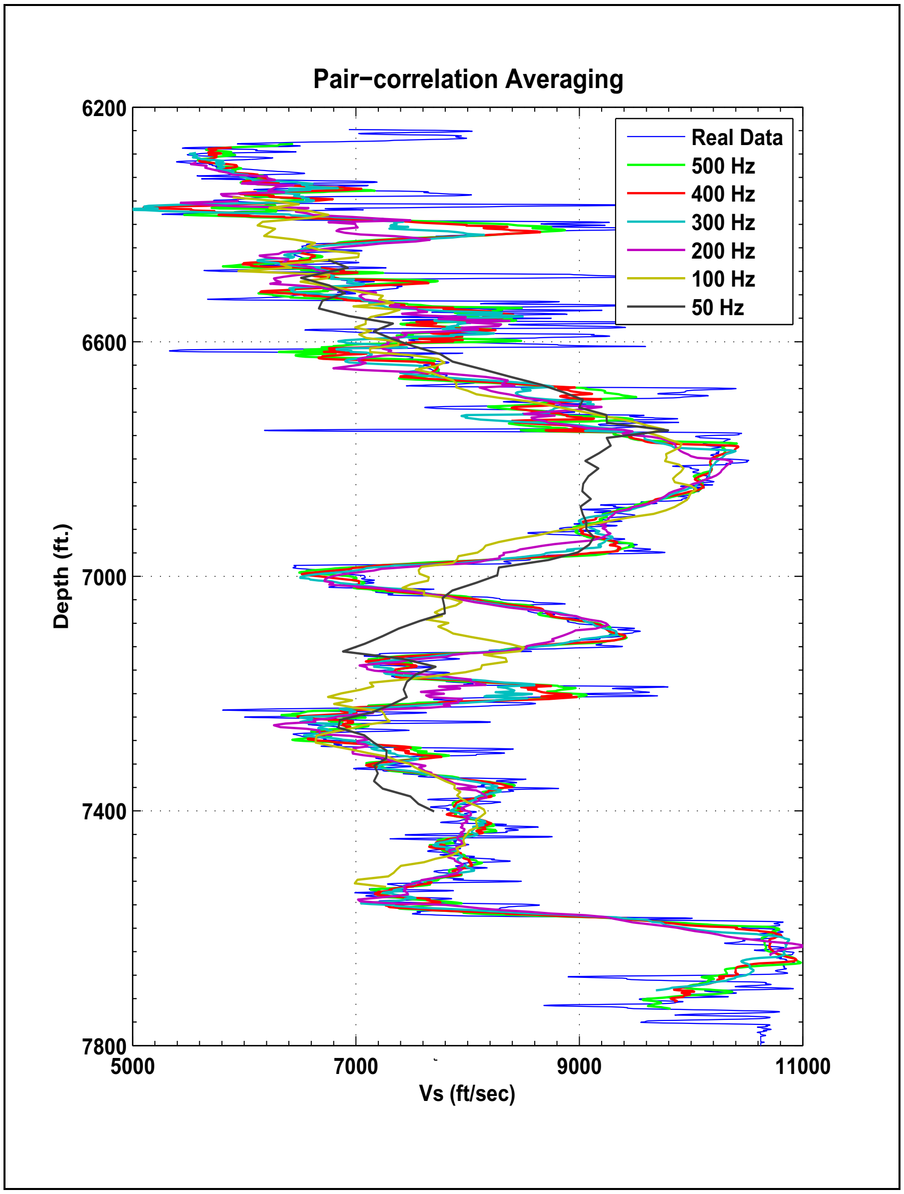

Figure 5.13: Color coded upscaling results of shear wave at various frequencies using pair correlation function averaging method. The real sonic frequency P-wave log is used for upscaling. The high frequency real data show large fluctuation of velocity along the depth. The upscaling result predicts a smoothing of the fluctuations and decreasing velocity at a lower frequencies.

5.7 Comparison of Upscaling Results

The results of three different upscaling methods are shown in Figures 5.14 to 5.21. The estimation of P-wave velocities at 500 Hz, 200 Hz, and 50 Hz, using three different methods of upscaling, are shown in Figures 5.14, 5.15 and 5.16, respectively. Also, upscaling results of S-wave velocities at 500 Hz, 200 Hz and 50 Hz are shown in Figures 5.17, 5.18, and 5.19, respectively. All figures show that the upscaling curves smooth the highly fluctuating real data. The lower the frequency, the more smooth are the upscaling results. Figures 5.14 and 5.17 show that at high frequencies there is only a small difference in upscaling results using the three methods. But as we decrease the frequency, the differences becomes larger as observed in Figures 5.15 and 5.18 for 200 Hz and 5.16 and 5.19 for 50Hz.

The difference in upscaling results obtained by these three upscaling methods are due to the difference between including or excluding the heterogeneities interactions (Tiwary et al., 2007a). If the concentration of heterogeneities are small, the inclusion interaction can be ignored (Grechka, 2007). Simple averaging, which ignores heterogeneity interactions provides significantly higher values of P- wave and S- wave velocities at 50 Hz than the other two methods (Figures 5.20 and 5.21). Figures 5.20 and 5.21 show that simple and Backus averaging will result P- and S-wave velocities that are too high.

In pair correlation function function averaging, only first-order interactions of stress fields with the inclusions are considered. However, if the inclusion density is large, the stress field around one inclusion may influence the stress field around other inclusions.

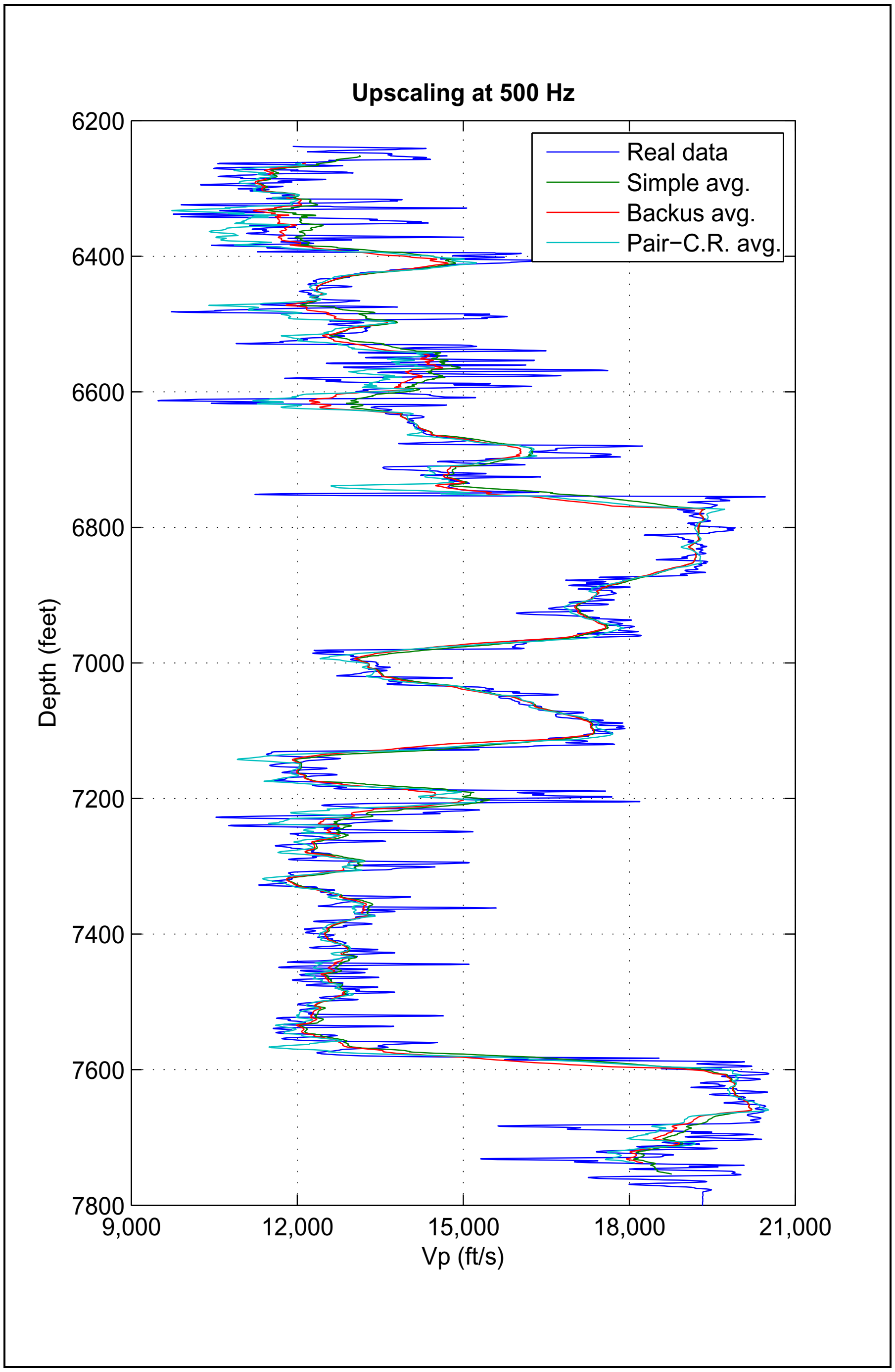

Figure 5.14: Comparison of upscaling methods obtained for Vp at 500 Hz using simple, Backus, and pair correlation, overlain on real sonic log P-wave input data (blue color).

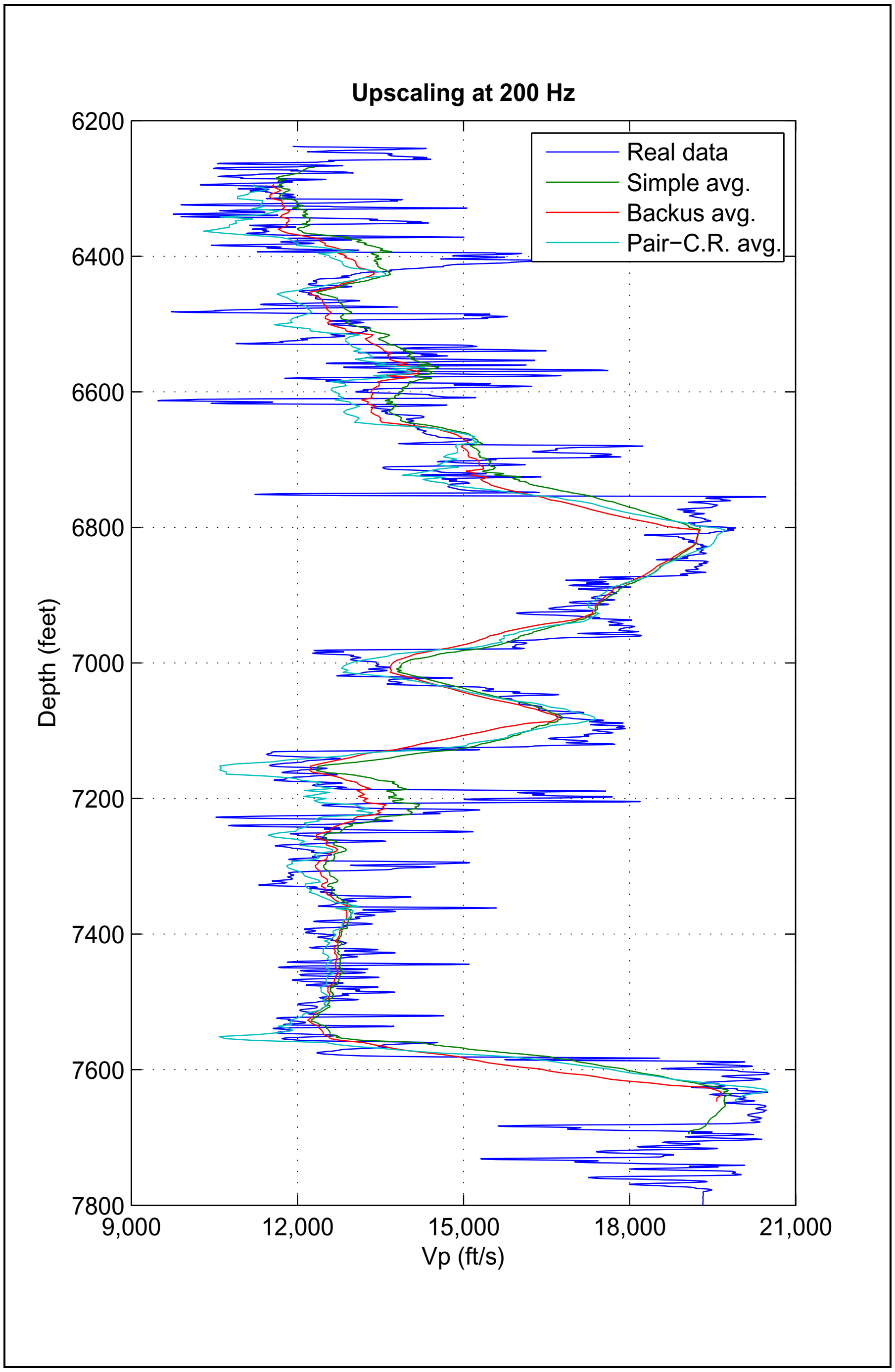

Figure 5.15: Comparison of upscaling methods obtained for Vp at 200 Hz using simple, Backus, and pair correlation, overlain on real sonic log P-wave input data (blue color).

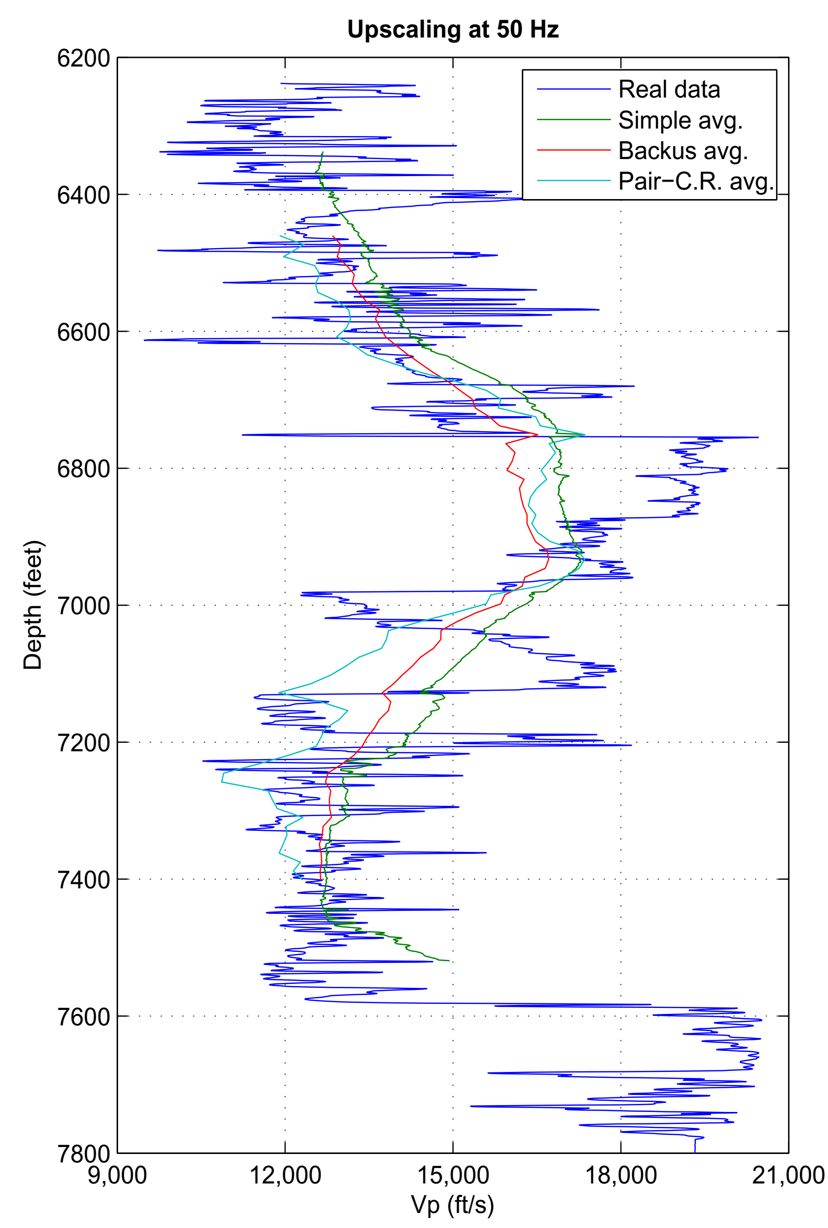

Figure 5.16: Comparison of upscaling methods obtained for Vp at 50 Hz using simple, Backus, and pair correlation, overlain on real sonic log P-wave input data (blue color).

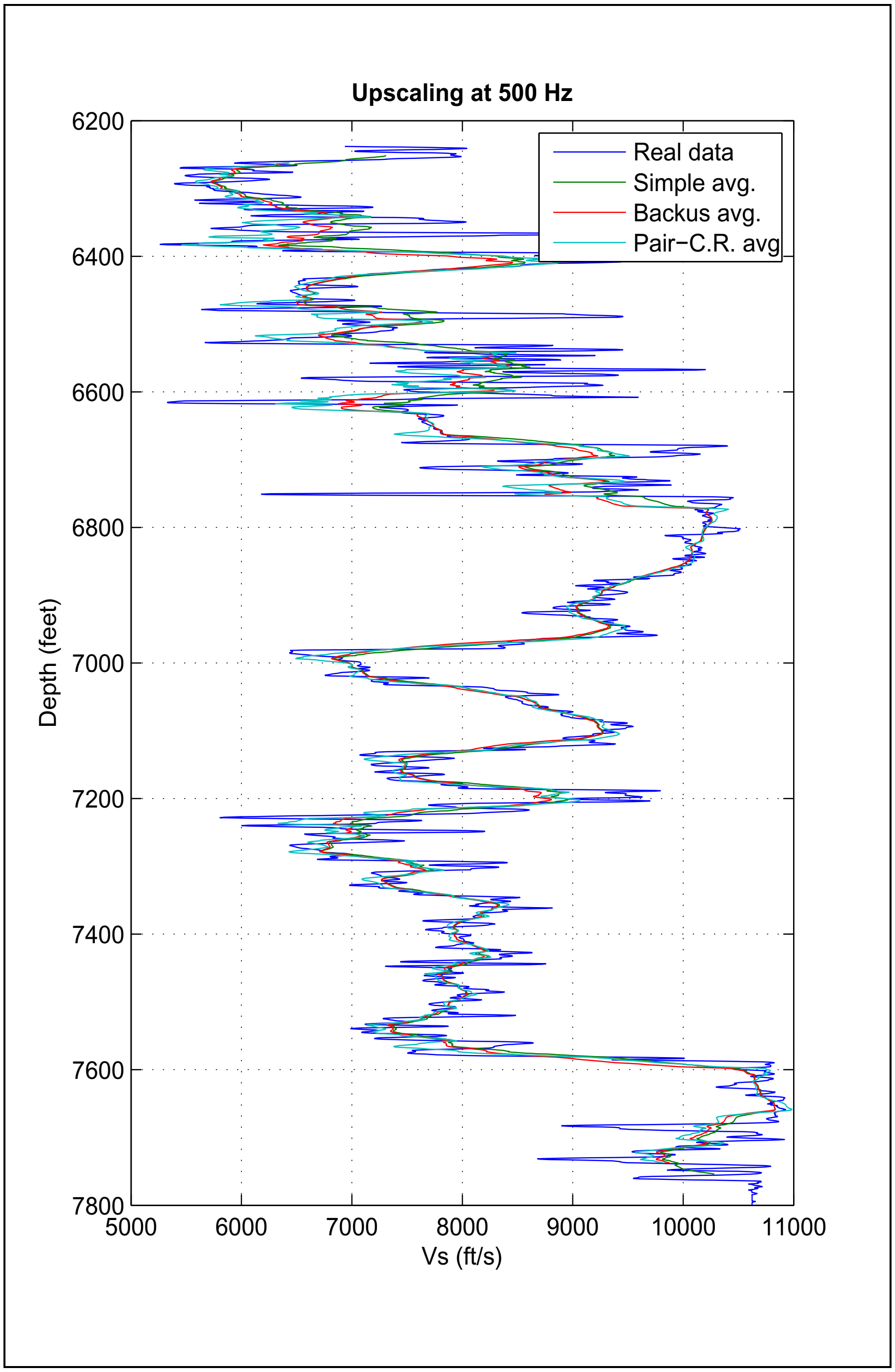

Figure 5.17: Comparison of upscaling methods obtained for Vs at 500 Hz using simple, Backus, and pair correlation, overlain on real sonic log shear wave input data (blue color).

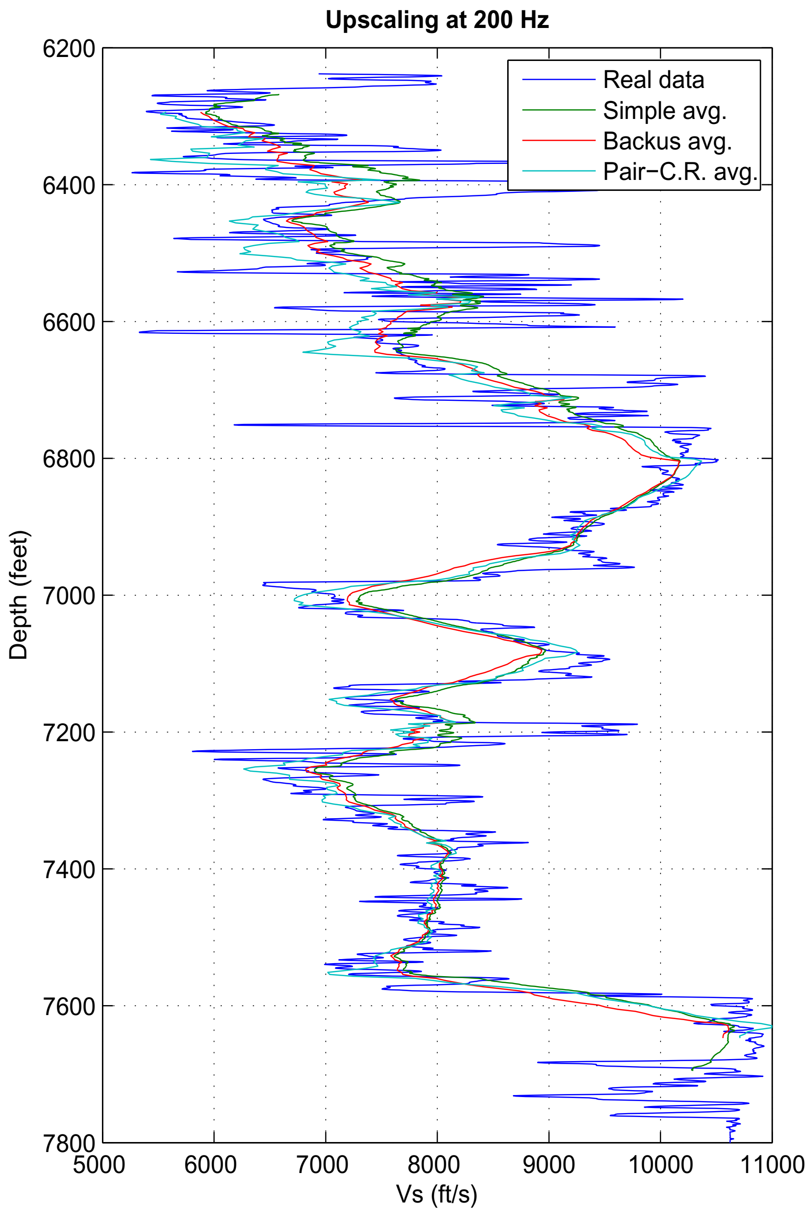

Figure 5.18: Comparison of upscaling methods obtained for Vs at 200 Hz using simple, Backus, and pair correlation, overlain on real sonic log shear wave input data (blue color).

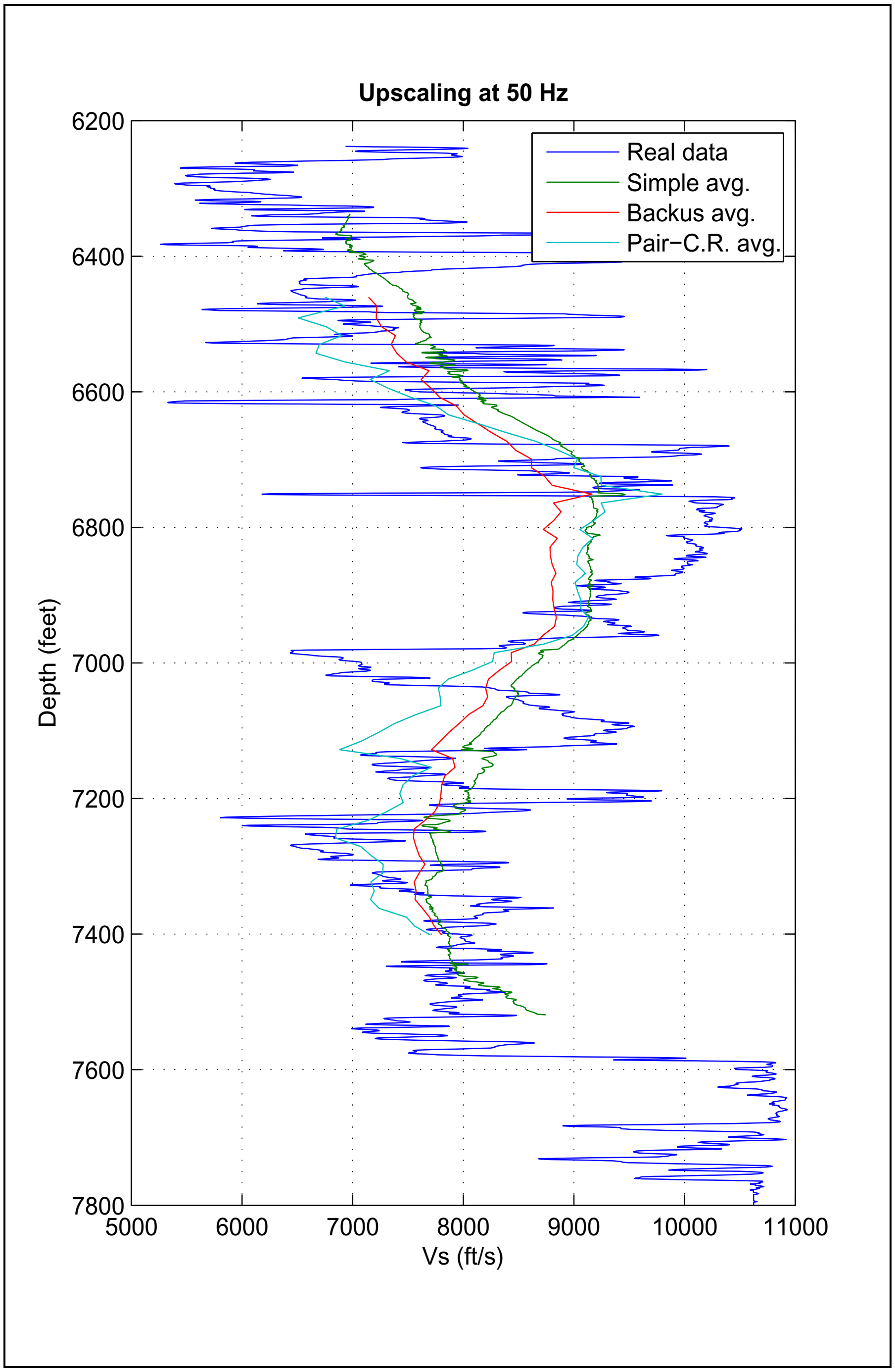

Figure 5.19: Comparison of upscaling methods obtained for Vp at 50 Hz using simple, Backus, and pair correlation, overlain on real sonic log shear wave input data (blue color).

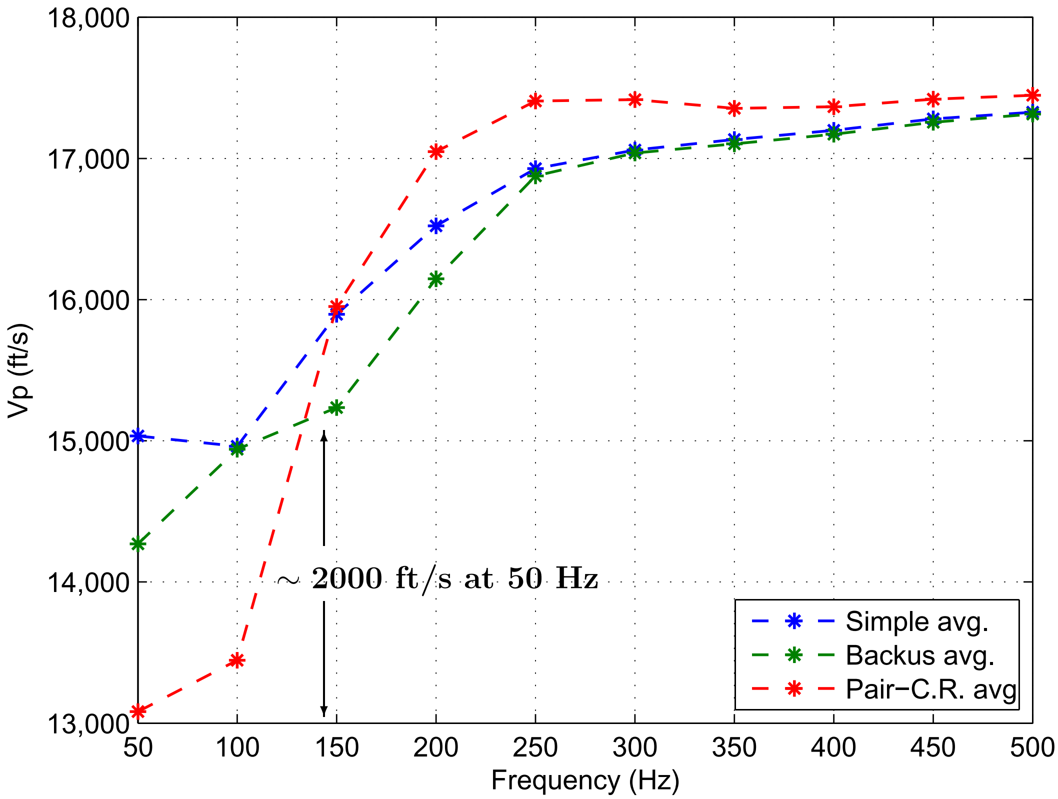

Figure 5.20: Upscaling results of P-wave velocity at various frequencies using three different upscaling methods, simple averaging, Backus averaging, and Pair-correlation function averaging at 7089 feet. At lower frequencies about 2000 ft/s difference in P-wave velocity is obtained by different upscaling methods, but this difference gets smaller at higher frequencies.

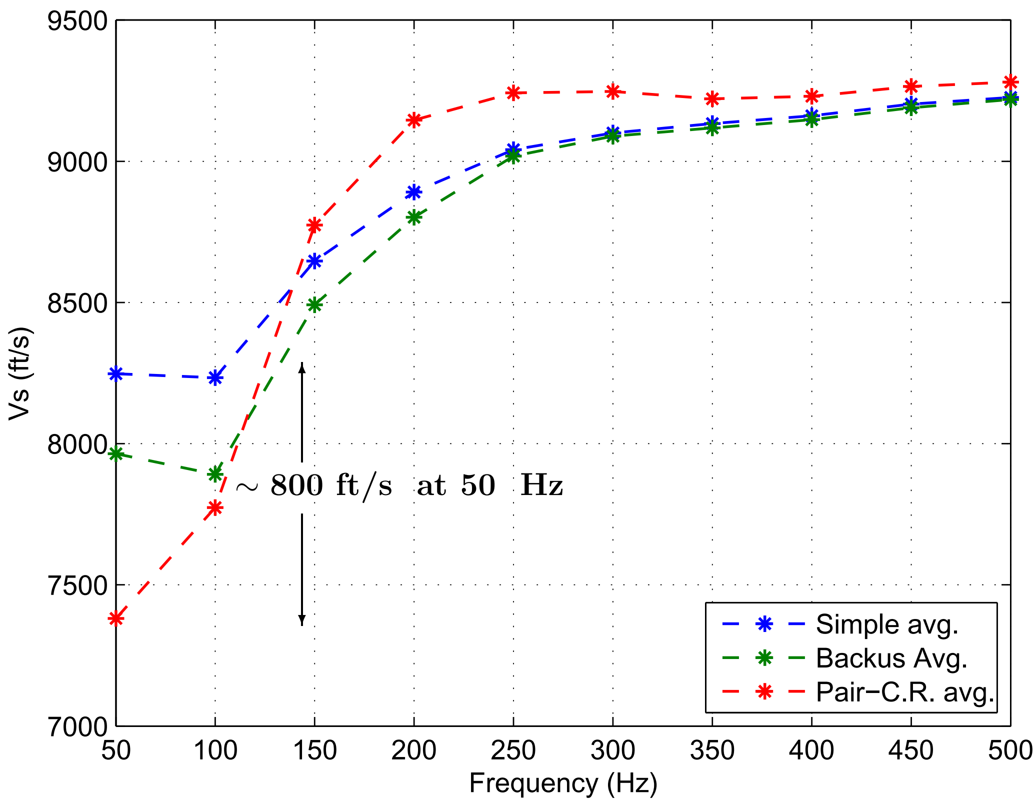

Figure 5.21: Same as Figure 5.20 but for shear wave velocity. At lower frequencies about 800 ft/s difference in shear wave velocity is obtained by different upscaling methods, but this difference gets smaller at higher frequencies.

5.8 Summary

The three different elastic upscaling methods provide different answers to the same question. This difference in the averaging method can be viewed as a difference in treatment of scattering attenuation by each of the methods considered. Pair correlation function averaging predicts the largest scattering attenuation, while simple averaging predicts the smallest. The effective dispersion due to the scattering may be viewed in this context as a measure of the degree of interaction of inclusions considered by each of the methods. The difference in results obtained by these methods for P-wave and S- wave upscaling shows $\sim$ 2000 ft/s and $\sim$ 800 ft/s respectively. The wave propagation in heterogeneous media suffers multiple scattering, particularly when the size of the wavelength is either comparable or smaller than the size of heterogeneities. In such circumstances it is necessary to consider higher-order interactions where the change in the stress field around a single heterogeneity due to elastic wave propagation will influence the stress field around other heterogeneities. Averaging based on the pair correlation function provides a way to consider the first-order interactions in the medium. Upscaling based on the pair correlation function, which accounts for both interaction and scattering in the heterogeneous media predicts lower values of elastic properties obtained by simple and Backus averaging.

Chapter 6

Conclusions

The Barnett Shale and equivalents currently produce some 55% of the U.S. natural gas supply. In spite of this importance almost all effective media theory has been developed for and applied to sand reservoirs. The main purpose of this dissertation has been to provide a fundamental understanding of shale anisotropy and wave propagation in cracked media. Clay mineral alignment and aligned cracks are considered to be the two main causes of shale anisotropy. Four shale models have been analyzed to investigate the isolated effect of clay mineral alignment and aligned cracks using effecting media theory based on the generalized singular approximation. Although both of these causes of anisotropy are well-documented in the existing literature, only a limited number of case studies address crack shape. There are also few experimental studies in which the shape of the cracks and matrix properties have been controlled. Thus theoretical modeling for arbitrary crack shape, crack concentration, and clay platelet alignment offers new insights into shale anisotropy.

Model studies conducted in this dissertation indicate that one cannot easily distinguish between gas or water saturation when clay mineral alignment is the main cause of anisotropy (i.e., cracks are randomly aligned), or when both the clay minerals and pores are aligned. When the mineral alignment is not the main cause of anisotropy, the singularity point disappears for gas saturation but does not for water saturation. When the matrix is isotropic and the cracks are aligned, the gas saturation can be distinguished from water-saturation using the P-wave signature.

Shale mineral alignment, pore alignment, aspect ratio and friability all impact shale anisotropy. Shale mineral alignment is very important when the role of aligned cracks is reduced, which occurs when shale has just undergone smectite to illite conversion but before cracking of any kerogen to oil has begun. Such simple models may allow one to evaluate the different stages in the burial history of shale.

Friability is an indirect measure of the way stress and/or strains are communicated through the rock when pores and matrix act together. Friability allows the "comparison body" to range between the classic Hashin-Shtrikman elastic bounds of a medium. As friability increases, the P and S anisotropy of the shale also increases. The amount of anisotropy caused by the shale matrix is controlled by the amount of the clay minerals in the shale; clay mineral alignment does not contribute significantly to anisotropy until it exceeds 10% of the total volume.

This dissertation provides a means to investigate the role of gas saturation, the creation of new pores and the ultimate state of the shale. Clay volume and clay alignment along with crack-induced porosity and crack alignment are the major factors causing anisotropy. Gas-filled cracks cause a greater degree of anisotropy because of a higher degree of contrast between host matrix and crack-filled fluid. The matrix dominates anisotropy when the cracks are water-filled. The crack dominates when they are gas-filled. With this understanding in mind one can start to explore a shale environment in order to investigate the hydrocarbon potential of the shale.

The ultrasonic measurements in this dissertation have been applied to nine different lithologic facies within the Barnett Shale. For each of the nine facies compressional and shear wave velocity are measured on samples at ultrasonic frequencies ($1MHz$). Elastic properties obtained from the rock samples belonging to the different facies indicate that the Barnett Shale can be characterized by five different seismic facies, which are either isotropic, or VTI in nature. The mineralogy-based velocities, which have been estimated using forward modeling and the ultrasonic lab measured velocities, are then used to extract the crack-induced porosity, the aspect ratio of the cracks, and the friability. Inverse modeling of measured velocities can thus be used as a tool to estimate crack parameters for reservoir exploration and exploitation. Also, the mineralogy-based estimates of the velocities can be used as a tool to characterize sedimentary facies in the absence of cores and log data.

The theoretical models commonly used to upscale heterogeneous elastic media are based on different physical considerations. Of the three different upscaling methods analyzed in this dissertation, indicate that the method based on the pair correlation method is preferred. The pair correlation method of upscaling assumes that the fluctuation in the physical properties is much smaller than the average values. The pair correlation method is more empirically reasonable and is based on more exact physics than the Backus and simple averaging. At the Barnett Shale depth (7089 ft) in the well the maximum difference in P- and S- wave velocities obtained by three different upscaling methods are 2000 ft/s and 800 ft/s respectively. This large difference in upscaled velocity and anisotropy may lead to poor seismic imaging.

The methods that account for interaction and scattering, based on the pair correlation approximation, results in a smaller velocity than Backus averaging, which ignores scattering. Simple averaging does not allow for either interaction or scattering. The higher upscaled velocity obtained by simple and Backus averaging in surface seismic frequency range may be attributed to not accounting for multiples by these methods. Pair correlation provides more accurate upscaling estimates of velocities at surface seismic exploration scales than Backus and simple averaging. However, future calibration studies require the highly-controlled measurements on synthetic rock samples.

Bibliography

Al-Khalifah, T., and Tsvankin, I., 1995, Velocity analysis for transversely isotropic media: Geophysics, **60**, 15501566.

Anderson, D., Minster, B., and Cole, D., 1974, The effect of oriented cracks on seismic velocities: Journal of Geophysical Research, **79**, 4011–4015.

Anstey, N. A., and O'Doherty, R. F., 2002, Cycles, layers, and reflections: Part 1: The Leading Edge, **21**, 44–51.

Auld, B. A., 1973, Acoustic fields and waves in solids.: John Wiley Sons, Inc.

Backus, G., 1962, Long-wave elastic anisotropy reduced by horizontal layering: Journal of Geophysical Research, **67**, 4427–4440.

Bass, J., 1995, Minerals Physics and Crystallography: A Handbook of Physical Constants: AGU.

Bayuk, I. O., and Chesnokov, E. M., 1997, Experimental and theoretical study of sedimetary rock properties: SEG Expanded Abstract, pages 984–986.

Bayuk, I., and Chesnokov, E., 1998, Correlation between elastic and transport properties of porous cracked anisotropic media: Journal of Physics and Chemistry of the Earth, **23**, 361–366.

Bayuk, I., and Chesnokov, E., 1999, Idenstification of the fluid type in a reservoir rock: Physics of the Solid Earth, **35**, 917–923.

Bayuk, I. O., Vikhorev, A. A., Hooper, J. M., Tertychnyi, V. V., Kukharenko, Y. A., and Chesnokov, E. M., 2003, Frequency dependent effects in porous rocks: SEG International Conference and Exhibition, Moscow, PS10.

Bayuk, I., Ammerman, M., and Chesnokov, E., 2007a, Elastic moduli of anisotropic clay: Geophysics., **72**, D107–D117.

——— 2007b, Upscaling of elastic properties of anisotropic rocks: Journal of Geophysical International.

Belikov, B. P., Alexandrov, K., and Ryzhova, T. V., 1970, Elastic Properties of Rock Forming Minerals and Rocks.: Nauka Publishers (in Russian).

Berryman, J., 1979, Long-wave elastic anisotropy in transversely isotropic media: Geophysics, **44**, 896–917.

Breeden, D., and Shipman, J., 2004, Shale analysis for mud engineers: AADE, pages 1–17.

Brown, R., and Corringa, J., 1975, On the dependance of the elastic properties of a porous rock and the compressibility of the pore fluid: Geophysics, **40**, 608–616.

Brown, W. F., 1955, Solid mixture permittivities: The Journal of Chemical Physics, **23**, 1514–1517.

Budiansky, B., and O'Connell, R., 1976, Elastic module of a cracked solid: International Journal of Solids and Structures, **12**, 81–97.

Cerveny, V., Molotkov, I. A., and Psencik, I., 1977, Ray method in seismology: Univ. Karlova.

Cheng, C., 1981, Crack models for a transversely anisotropic medium: Journal of Geophysical Research, **98**, 675–684.

Chesnokov, E., Kukharenko, Y. A., and Kukharenko, P. A., 1995, Method of diagram technique for calculation of effective physical parameters of microinhomogeneous media Method of diagram technique for calculation of effective physical parameters of microinhomogeneous media, SPIE-The International Society of Optical Engineers, Mathematical methods in Geophysical Imaging III, 72–91.

Chesnokov, E. M., Kukharenko, Y. A., and Kukharenko, P. Y. a., 1998, Frequency dependence of physical parameters in microinhomogeneous media: Space Statistics, Revue de L'Institute Francais du Petrole, **53**, 729–734.

Chesnokov, E. M., Queen, J., Kukharenko, Y. A., Bayuk, I. O., and Hooper, J., 2000, Dispersive properties of porous cracked media: Dispersive properties of porous cracked media:, 7th European Conference on the Mathematics of Oil Recovery, Baveno Italy, 6–7.

Christensen, N., and Johnston, J., 1995, Seismic anisotropy of shales.: Journal of Geophysical Research, **100**, 5991–6003.

Chung, D. H., Swica, J., and Crandall, W., 1963, Relation of single-crystal elastic constants to polycrystalline isotropic elastic moduli of mgo: Journal of the American Ceramic Society, **46**, 452–457.

Crampin, S., and Leary, P., 1993, Limits to crack density: the state of fractures in crustal rocks: SEG Expanded Abstract, **12**, 758–761.

Crampin, S., McGonigle, R., and Bamford, D., 1980, Estimating crack parameters from observations of p-wave velocity anisotropy: Geophysics, **45**, 345–360.

Crampin, S., McGonigle, R., and Ando, M., 1986, Extensive-dilatancy anisotropy beneath mount hood, oregon and the effect of aspect ratio on seismic velocities through aligned cracks: Journal of Geophysical Research, **91**, 12703–12710.

Crampin, S., 1978, Seismic wave propagation through a cracked solid: polarization as a possible dilatancy diagnostic: Geophysical Journal of the Royal Astronomical Society, **53**, 467–496.

Crampin, S., 1984, Effective anisotropic elastic constants for wave propagation through cracked solids: Geophysical Journal of the Royal Astronomical Society, **76**, 135–145.

Crampin, S., 1994, The fracture criticality of crustal rocks: Geophysical Journal International, **118**, 428–438.

Dellinger, J., and Vernik, L., 1994, Do traveltimes in pulse-transmission experiments yield anisotropic group or phase velocities?: Geophysics, **59**, 1774–1779.

Diego, T., and Douglas, R. G., 1999, Oxygen-related sediment microfabrics in modern “black shale”, gulf of california, mexico: Journal of Foraminiferal Research, **29**, 453464.

Douma, J., 1988, The effect of aspect ratio on crack-induced anisotropy: Geophysical Prospecting, **36**, 614–632.

Eshelby, D., 1957, The determination of the elastic field of an ellipsoidal inclusion, and related problems: Proceedings of the Royal Society, London, Series A, **241**, 376–396.

Floquet, G., 1883, Sur les équations differentielles linéaires à coefficients périodiques: Ann. École. Norm. Sup., **12**, 47–88.

Gale, J. F. W., Reed, R. M., and Holder, J., 2007, Natural fractures in the barnett shale and their importance for hydraulic fracture treatments: AAPG, **91**, 603622.

Gold, N., Shapiro, S. A., and Muller, T. M., 2000, An approach to upscaling for seismic waves in statistically isotropic heterogeneous elastic media: Geophysics, **65**, 1837–1850.

Grechka, V., 2007, Multiple cracks in vti rocks: Effective properties and fracture characterization: Geophysics, **72**, D81–D91.

Grubb, H. J., and Walden, A. T., 1995, Smoothing seismically derived velocities: Geophysical Prospecting, **43**, 1061–1082.

Hasin, Z., and Shtrikman, S., 1962, A variational approach to the theory of the effective magnetic permeability of multiphase materials: Journal of Applied Physics., **33**, 3125–3133.

Helbig, K., 1994, Foundations of anisotropy for exploration seismics: Pergamon.

Hornby, B., Schwartz, L., and Hudson, J., 1994, Anisotropic effective-medium modeling of the elastic properties of shales: Geophysics, **59**, 1570–1583.

Hudson, J., 1980, Overall properties of a cracked solid: Mathematical Proceedings of the Cambridge Philosophical Society, **88**, 371–384.

Hudson, J., 1981, Wave speeds and attenuation of elastic waves in material containing cracks: Geophysical Journal of the Royal Astronomical Society, **64**, 133–150.

Hudson, J., 1986, A higher order approximation to the wave propagation constants for a cracked solid: Geophysical Journal of the Royal Astronomical Society, **87**, 265–274.

Jacobsen, M., Minshull, T., and Singh, S., 2000, Elastic properties of hydrate-bearing sediments using effective medium theory: Journal of Geophyisical Research, **105**, 561–577.

Joachian, C. J., 1975, Quantum collision theory: North-Holland Publishing.

Johnston, J., and Christensen, N., 1994, Elastic constants and velocity surfaces of indurated anisotropic shales: Surveys in Geophysics, **15**, 481–494.

Johnston, D. I., 1987, Physical properties of shale at temperature and pressure: Geophysics., **52**, 1391–1401.

Jones, L., and Wang, H., 1981, Ultrasonic velocities in cretaceous shales from the williston basin: Geophysics, **46**, 288–297.

Katahara, K., 1996, Clay minerals elastic properties: SEG Expanded Abstract, **15**, 16911694.

Kriessman, C., Harrison, S., and Belson, H., 1958, Relationship between single crystal and effective polycrystalline anisotropy constants in ferrites: Journal of Applied Physics, **29**, 452–453.

Kuster, G. T., and Toksoz, N. M., 1974, Velocity and attenuation of seismic waves in two-phase media, i. theoretical formulations: Geophysics, **39**, 607–618.

Landau, L., and Lifshitz, E., 1986, Theory of Elasticity: Butterworth-Heinemann.

Levin, V., and Markov, M., 2005, Elastic properties of inhomogeneous transversely isotropic rocks: International Journal of Solids and Structures, **42**, 393408.

Liner, C., and Fei, T., 2007, The backus number: The Leading Edge, **26**, 420–426.

Lonardelli, I., Wenk, H. R., and Ren, Y., 2007, Preferred orientation and elastic anisotropy in shales: Geophysics, **72**, D33–D40.

Mase, G., 1970, Theory and problem of continuum mechanics: Mc Graw-Hill.

Mavko, G., Mukerji, T., and Dvorkin, J., 1998, The rock physics handbook: Cambridge University Press.

Moulton, J. D., Knapek, S., and Dendy, J. E., 1998, Multilevel upscaling in heterogeneous porous media: URL: citeseer.ist.psu.edu/212257.html.

Mukerji, T., Mavko, G., Mujica, D., and Lucet, N., 1995, Scale-dependent seismic velocity heterogeneous media: Geophysics, **60**, 1222–1233.

Musgrave, M. J. P., 1970, Crystal Acoustics: Holden Day.

Nishizawa, O., 1982, Seismic velocity anisotropy in a medium containing oriented cracks-transversely isotropic case: Journal of Physics of the Earth, **30**, 331–347.

Norris, A., 1985, A differential scheme for the effective moduli of composites: Mech. Mater., **4**, 1–16.

O'Brian, N. R., and Slatt, R. M., 1990, Argillaceous Rock Atlas: Springer-Verlag.

O'Connell, R. J., and Budiansky, B., 1974, Seismic velocities in dry and saturated cracked solids: Journal of Geophysical Research, **82**, 5719–5735.

Peselnick, L., and Robie, R., 1963, Elastic constants of calcite: Journal of Applied Physics, **34**, 2494–2495.

Postma, G., 1955, Wave propagation in a stratied medium: Geophysics, **20**, 780–806.

Rathore, J. S., Fjaer, E., Holt, R. M., and Renlie, L., 1995, P- and s-wave anisotropy of a synthetic sandstone with controlled crack geometry: Geophysical Prospecting, **43**, 711–728.

Reuss, A., 1929, Berechchnung der fliessgrenzen von mischsristallen auf grund der plastiziatsbedingung fur einkristalle: Zeitschrift fur Angewandte Mthematik und Mechanik, **9**, 49–58.

Roy, B., Queen, J., Bayuk, I. O., Kukharenko, Y. A., and Chesnokov, E. M., 2001, Prediction of frequency dependent velocity in porous reservoir: SEG Expanded Abstract, **20**, 1933–1936.

Ruger, A., 2001, Reflection coefficients and azimuthal avo analysis in anisotropic media: Society of Exploration Geophysicists.

Rytov, S., 1956, Acoustical properties of a thinly laminated media: Soviet Physics:Acoustics, **2**, 68–80.

Sayers, C., and Kachanov, M., 1995, Microcrack-induced elastic wave anisotropy of shales: Journal of Geophysical Research, **100**, 4149–4156.

Sayers, C. M., 2005, Seismic anisotropy of shales: Geophysical Prospecting, **53**, 667–676.

Schoenberg, M., and Douma, J., 1988, Elastic wave propagation in media with parallel fractures and aligned cracks: Geophysical Prospecting, **36**, 571–590.

Schoenberg, M., and Muir, F., 1981, A calculus for finely layered anisotropic media: Geophysics, **54**, 581589.

Schoenberg, M., and Sayers, C. M., 1995, Seismic anisotropy of fractured rock: Geophysics, **60**, 204–211.

Selley, R., 1998, Elements of Petroleum Geology: Academic Press.

Sheriff, R., 2002, Encyclopedia Dictionary of Applied Geophysics: SEG.

Shermergor, T. D., 1977, Theory of elasticity of microinhomogeneous media: Moscow, Nauka, (in Russian).

Singh, P., and Slatt, R., Sequence stratigraphy of Barnett Shale, Fort-Worth basin:, Devon Energy Inc., Quarterly Report, University of Oklahoma, September 2006.

Sparkman, M. A., 2006, Factors contributing to shale anisotropy: Investigation of shale anisotropy through mineralogy-based theoretical modeling: Master's thesis, School of Geology and Geophysics, University of Oklahoma.

Thomsen, L., 1986, Weak elastic anisotropy: Geophysics., **51**, 1954–1966.

Thomsen, L., 1995, Elastic anisotropy due to aligned cracks in porous rock: Geophysical Prospecting., **43**, 805–829.

Tiwary, D. K., Bayuk, I. O., Vikhorev, A. A., Ammerman, M., and Chesnokov, E. M., 2007a, Comparison of seismic upscaling methods: SEG Expanded Abstract., **26**, 1933–1936.

——— 2007b, Behavior of shear waves in water- and gas- filled cracks in anisotropic matrix: SEG Expanded Abstract, **26**, 1939–1940.

Tosaya, C., and Nur, A., 1982, Effects of diagenesis and clays on compressional velocities in rocks: Geophys. Res. Lett., **9**, 5–8.

Tsvankin, I., 1997, Anisotropic parameters and p-wave velocity for orthorhombic media: Geophysics, **62**, 1292–1309.

Vernik, L., and Liu, X., 1997, Velocity anisotropy in shales: A petrophysical study: Geophysics, **62**, 521532.

Vernik, L., and Nur, A., 1990, Ultrasonic velocity and anisotropy at petroleum source rocks: The bakken formation: 60th Ann. Intemat. 60th Ann. Intemat. Mtg.,Soc. Expl. Geophys., Expanded Abstracts, pages 845–848.

Vikhorev, A., Ammerman, M., Brown, R., Abaseyev, S., and Chesnokov, E., 2006, Full form synthetic seismogram calculations and determination of focal mechanism of frac events based on 3-c seismic array obserbations: Proceedings of the 100th Anniversary Earthquake Conference *in* the Seismological Society of America, pages 1514–1517.

Vikhorev, A. A., 2005, Wave propagation in random inhomogeneous medium with the accounting of relative moment and interaction of phases: Ph.D. thesis, The Russian Academy of Sciences.

Voigt, W., 1928, Lehrbuch der kristallphysik: Berlin: Teubner.

Wenk, H. R., and Houtte, P. V., 2004, Texture and anisotropy: Institute of Physics Publishing, **67**, 1367–1428.

Wenk, H. R., Lonardelli, I., Franz, H., Nihei, K., and Nakagawa, S., 2007, Preferred orientation and elastic anisotropy of illite-rich shale: Geophysics, **72**, D69–E75.

Willis, J., 1977, Bounds and self-consistent estimates for the overall properties of anisotropic composites: Journal of the Mechanics and Physics of Solids, **25**, 185–202.

Wood, A. W., 1955, A textbook of sound: The MacMillan Co., New York, pp 360.

Xu, S., and White, R. E., 1995, A new velocity model for clay-sand mixtures: Geophysical Prospecting, **43**, 91–118.

Xu, S., and White, R., 1996, Modeling transport properties of anisotropic shaly formation: 66 Annual International Meeting, SEG Expanded Abstract., **66**.

Xu, Z., Cornilsen, B., Popko, D., Wei, B., Pennington, W., and Wood, J., Quantitative mineral analysis by ftir spectroscopy:, *www.geo.mtu.edu/svl/pioneer/ftir/ftir_rpt.htm*, Michigan Technological University, 13/11/ 2007.

Appendix A

Phase and Group Velocity in Anisotropic Media

A.1 Phase Velocity

Let us consider Newton's Second Law to describe the motion of a volume element in a medium:

$$f_i = ma_i, \tag{A.1}$$

where f_i is the force, m is the mass and a_i is the acceleration. Hereafter, I will use vectors and tensors in the index form, i.e., $\vec{a} \leftrightarrow a_i$.

From continuum mechanics (Mase, 1970), we know that

$$f_i = \frac{\partial \sigma_{ij}}{\partial x_j}, \tag{A.2}$$

where, σ_{ij} is a second rank symmetric tensor.

From equation A.1 and A.2,

$$\frac{\partial \sigma_{ij}}{\partial x_j} = \rho \frac{\partial^2 u_i}{\partial t^2}. \tag{A.3}$$

where, u_i is the displacement vector and $\frac{\partial^2 u_i}{\partial t^2}$ is the acceleration.

In linear elastic inhomogeneous and arbitrary anisotropic media without initial stress, Hooke's Law can be expressed (Mase, 1970) as

$$\sigma_{ij}(\mathbf{x}) = C_{ijkl}(\mathbf{x})\varepsilon_{kl}, \tag{A.4}$$

where, C_{ijkl} is the tensor of elastic constants, or the stiffness tensor, and ε_{kl} is the strain tensor. The stiffness tensor, C_{ijkl}, is symmetric due to the symmetry of stress ($\sigma_{ij} = \sigma_{ji}$), and strain ($\varepsilon_{ij} = \varepsilon_{ji}$), and the scalar character of elastic energy (Landau and Lifshitz, 1986). In this case

$$C_{ijkl} = C_{jikl} = C_{ijlk} = C_{lkij}. \tag{A.5}$$

Substituting equation A.4 in A.3,

$$\frac{\partial}{\partial x_j}\bigg(C_{ijkl}(\mathbf{x})\varepsilon_{kl}(\mathbf{x})\bigg) = \rho \frac{\partial^2 u_i}{\partial t^2}. \tag{A.6}$$

Taking into account the expression for the linear strain tensor (Landau and Lifshitz, 1986):

$$\varepsilon_{kl}(\mathbf{x}) = \frac{1}{2}\bigg(\frac{\partial u_k(\mathbf{x})}{\partial x_l} + \frac{\partial u_l(\mathbf{x})}{\partial x_k}\bigg) \tag{A.7}$$

From equation A.6 and A.7,

$$\frac{\partial}{\partial x_j}\left[C_{ijkl}(\mathbf{x})\frac{1}{2}\left(\frac{\partial u_k(\mathbf{x})}{\partial x_l}+\frac{\partial u_l(\mathbf{x})}{\partial x_k}\right)\right]=\rho\frac{\partial^2 u_i}{\partial t^2}. \tag{A.8}$$

Since C_{ijkl} is a symmetric tensor, equation A.8 can be written,

$$\left(\frac{\partial}{\partial x_j}C_{ijkl}(\mathbf{x})\frac{\partial}{\partial x_l}\right)u_k=\rho\frac{\partial^2 u_i}{\partial t^2}. \tag{A.9}$$

If the medium is homogeneous, then the C_{ijkl}, σ_{ij} and ε_{ij} will be constant at any point in the medium, therefore equation A.9 can be expressed as

$$C_{ijkl}\ \frac{\partial^2 u_k}{\partial x_j \partial x_l}=\rho\frac{\partial^2 u_i}{\partial t^2}, \tag{A.10}$$

which is the wave equation for homogeneous arbitrary anisotropic media.

Let us consider the plane wave propagation in inhomogeneous media:

$$u_k = A\bullet P_i e^{-i(k_i x_i-\omega t)}, \tag{A.11}$$

where, u_k is a displacement vector, A is the amplitude of the displacement, P_k is the direction of the displacement (or displacement vector), and k_i is the wave vector in n_i direction. The wave vector $k_i = \mathbf{k}\bullet n_i$. x_i is the vector co-ordinate, t is the time, and ω is the angular velocity.

The condition for the existence of a plane wave in arbitrary anisotropic media (equation A.11) can be obtained by substituting expression A.11 into equation A.10. Before doing the substitution, let us present expression A.11 in the form:

$$u_k = A\bullet P_k e^{-ik(n_i x_i - vt)}, \tag{A.12}$$

where $v = \omega/\mathbf{k}$ is the phase velocity.

Substituting equation A.12 into A.10, and calculating the differential:

(1) First derivative over x_i:

$$C_{ijkl}\frac{\partial}{\partial x_j}\Big[\big(-ik\ n_i\ \delta_{il}\big)u_k\Big] = \rho v^2 u_i\ (-k^2) \tag{A.13}$$

where, $\delta_{il} = \frac{\partial x_i}{\partial x_l}$ is the Kronecker Delta. The Kronecker Delta, $\delta_{ik} = 1$ when $i = j$, and 0 when $i \neq j$. In the right side of equation A.13 the second derivative over time is already written.

(2) Second derivative:

$$C_{ijkl}\Big[\big(-k^2\ n_l\ n_j\big)u_k\Big] \quad = \quad \rho v^2 u_i\ (-k^2), \tag{A.14}$$

or,

$$C_{ijkl}\Big[\big(n_l\ n_j\big)u_k\Big] \quad = \quad \rho v^2 u_i. \tag{A.15}$$

Using equation A.12,

$$C_{ijkl}\big(n_l\ n_j\big)A \bullet P_k \quad = \quad \rho v^2 A \bullet P_i, \tag{A.16}$$

or

$$C_{ijkl}\big(n_l\ n_j\big)P_k \quad = \quad \rho v^2 P_i, \tag{A.17}$$

where, $n_i\delta_{il} = n_l$, and $n_i\delta_{ij} = n_j$.

After simple algebraic transformation equation A.17 can be written as

$$\left(C_{ijkl}\ n_j\ n_l\ - \rho v^2 \delta_{ik}\right) P_k \quad = \quad 0, \tag{A.18}$$

where, $P_i = \delta_{ik} P_k$ and δ_{ik} is the Kronecker Delta.

Equation A.18 represents the Green-Christoffel equation (Landau and Lifshitz, 1986), which can be written:

$$\left(\Gamma_{ik} - \rho v^2 \delta_{ik}\right) P_k = 0, \tag{A.19}$$

where,

$$\Gamma_{ik} = C_{ijkl}\ n_j\ n_l. \tag{A.20}$$

Expression A.20 represents the symmetric Green-Christoffel tensor, where $i, j, k, l = 1, 2, 3$.

Equation A.19 will have an unique solution if and only if the determinant of this equation is equal to zero. i.e, if

$$|\Gamma_{ik} - \rho v^2 \delta_{ik}| = 0. \tag{A.21}$$

The solutions of equation A.21 will have three eigenvalues (three different velocities) and three eigenvectors (three displacement vectors). The three different velocities will represent the phase velocities (v) in an arbitrary anisotropic media and the three displacement vectors the polarization of the wavefield.

For example let us obtain the exact expression for the phase velocities in transversely isotropic media with vertical axis of symmetry (VTI). According to Helbig (1994), VTI medium is characterized by an isotropic horizontal plane in which velocity does not depend on the direction of propagation of a wave (i.e., n_i), and vertical axis of a symmetry (Figure A.1).

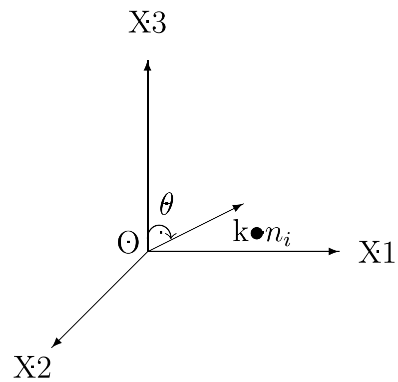

Figure A.1: Schematic representation of VTI medium, in which plane O X1 X2 represnts the plane of isotropy and O X1 X3 and O X2 X3 are the mirror planes. The angle (θ) is measured from the axis of symmetry to the direction of propagation of a wavefront.

In VTI media, equation A.21 can be solved analytically, and the three eigenvalues (phase velocities) can be expressed as a function of angle, θ, in the $\mathbf{k}$ vector direction. Following Ruger (2001) the phase velocities (V_P, V_{SH} and V_{SV}) in VTI media are:

$$V_P = \frac{1}{2\rho}\sqrt{(C_{11}+C_{44})\sin^2\theta + (C_{33}+C_{44})\cos^2\theta + K}, \tag{A.22}$$

$$V_{SV} = \frac{1}{2\rho}\sqrt{(C_{11}+C_{44})\sin^2\theta + (C_{33}+C_{44})\cos^2\theta - K}, \tag{A.23}$$

$$V_{SH} = \frac{1}{\rho}\sqrt{C_{66}\sin^2\theta + C_{44}\cos^2\theta}, \tag{A.24}$$

where, $K \equiv \sqrt{\left((C_{11} - C_{44}) \sin^2\theta - (C_{33} - C_{44}) \cos^2\theta\right)^2 + 4(C_{13} + C_{44})^2 \cos^2\theta \sin^2\theta)}$, and $C_{11}, C_{13}, C_{33}, C_{44}$, and C_{66} are the five independent elastic constants in VTI media.

Due to the symmetry of the Green-Christoffel matrix (equation A.20), at any given phase angle the polarization vectors P_k for SH, (quasi) SV, and (quasi) P are mutually orthogonal. However, the propagation direction (k_i) and the polarization direction (P_k) are in general orthogonal to each other only in the SH-wave. Since V_{SV} and V_{SH} are not equal to each other in anisotropic media, ($V_{SH} \neq V_{SV}$ in the same direction) splitting of the shear waves will take place. In other words, the two shear waves (V_{SH} and V_{SV}) travel at a different velocity in the same direction. Also, it can be noted that the periodical behavior of V_P, V_{SH} and V_{SV} is due to the fact that the equations A.22, A.23 and A.24 are presented via $sin\theta$ and $cos\theta$, which are periodic functions.

A.2 Group Velocity

Unlike isotropic media, in an anisotropic medium the displacement vector and the wave vector do not coincide with each other, and hence the velocity along the wave vector and along the energy flux (flow of energy) are different as well. The velocity along the wave vector is called phase velocity, and the velocity along the energy flux is called group velocity, or ray velocity.

Let us rewrite the Green-Christoffel equation A.17 as

$$C_{ijkl}\, n_j n_l\, P_k = \rho v^2 P_i. \tag{A.25}$$

Multiplying both sides of equation A.25 by P_i, we get

$$C_{ijkl}\ n_j n_l\ P_k\ P_i = \rho v^2 P_i^2 \tag{A.26}$$

where, P_i is a displacement vector. For the case in which P is a unit vector; $P_i^2 = P_1^2 + P_2^2 + P_3^2 = 1$. Then, equation A.26 can be presented in the following form:

$$C_{ijkl}\ n_j n_l\ P_k\ P_i = \rho v^2, \tag{A.27}$$

or

$$C_{ijkl}\ n_j n_l\ P_k\ P_i = \rho \omega^2 \frac{\lambda^2}{4\pi^2}, \tag{A.28}$$

where $v = \frac{\omega}{k} = \omega \frac{\lambda}{2\pi}$ is the phase velocity. Multiplying equation A.28 by $\frac{4\pi^2}{\lambda^2}$, we get:

$$C_{ijkl}\ P_i\ k_j k_l\ P_k = \rho \omega^2, \tag{A.29}$$

where $\frac{2\pi}{\lambda} n_j \equiv k_j$ and $\frac{2\pi}{\lambda} n_l \equiv k_l$. Differentiating A.29 with respect to k_j or k_l, we get:

$$2C_{ijkl}\ P_i\ k_l\ P_k = 2\rho\omega \frac{\partial \omega}{\partial k_j}, \tag{A.30}$$

or

$$C_{ijkl}\ P_i\ k_l\ P_k = \rho\omega \frac{\partial \omega}{\partial k_j}, \tag{A.31}$$

or

$$V_j^g = \frac{\partial \omega}{\partial k_j} = \frac{1}{\rho\omega} C_{ijkl}\ P_i\ k_l\ P_k, \tag{A.32}$$

where V_J^g is defined as the *group* or *ray* velocity in k_l direction. The expression in equation A.32 can also be written as

$$V_j^g = \frac{\partial \omega}{\partial k_j} = \frac{1}{\rho v} C_{ijkl}\ P_i\ P_l\ n_k. \tag{A.33}$$

By introducing the second Green-Christoffel tensor, we get:

$$T_{jk} = C_{ijkl}\ P_i\ P_l, \tag{A.34}$$

where T_{jk} is the energy vector. We can now write equation A.33 as

$$V_j^g = \frac{\partial \omega}{\partial k_j} = \frac{1}{\rho v} T_{jk}\ n_k, \tag{A.35}$$

where, ρ is the density of the medium, v is the phase velocity and n_k are the direction cosines. It is obvious from equation A.35 that the speed and direction at which a wavefront moves is different from the speed and direction at which T_{jk} moves. In other words, the phase velocity and group velocity in an anisotropic media move at different speeds and directions (Figure A.2).

The basic differences of wave propagation in anisotropic media and in isotropic media are:

1. the existence of periodical dependencies of velocities on wave vector direction (equation A.22, A.23, and A.24);

2. non-coincidence of the direction of propagation and particle displacement (equation A.19);

3. the non-coincidence of the magnitude of phase and group velocities and an angular dependence on this difference (equation A.35);

4. non-existence of pure longitudinal (V_P) or shear (V_{SV}) waves. These are, respectively, called quasi-P and quasi-SV wave (equation A.19). For waves propagating at an angle to the bedding plane, it is found that that the SV and P-waves couple so that neither is a pure mode, while SH-wave remains a pure mode; and

5. the existence of two shear waves. In transversely isotropic medium they are V_{SV} and V_{SH} (equation A.23 and A.24).

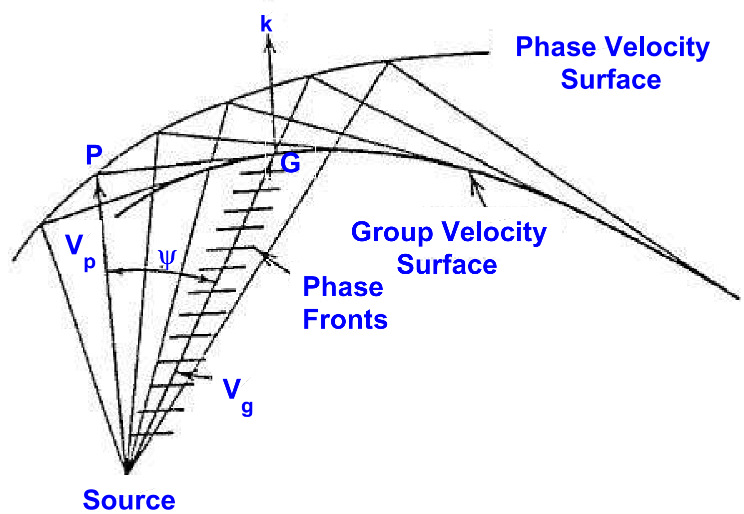

Figure A.2: Geometrical representation of plane waves from a point source in anisotropic homogeneous media. In an anisotropic media each plane waves will travel with an individual phase velocity. The locus of P and G, respectively, is called phase and group velocity. The angle between wavefront normal and group velocity direction is ψ. In true homogeneous and anisotropic media phase and group velocity travel with different velocities and in different directions. (Modified from Johnston and Christensen (1994)).

Appendix B

Representation of the Local Operator g in General Anisotropic Media

According to Bayuk and Chesnokov (1998) the calculation of effective elastic constants in heterogeneous anisotropic media can be constructed using the GSA method as shown in equation B.1 (also shown in equation 2.38).

$$\begin{aligned}\mathbf{C}^{*} &= \left\{\sum_{i=1}^{n} v_i \mathbf{C}_i \int P_i(\chi_i;\theta,\phi,\psi)\left[\mathbf{I}-\mathbf{g}_i(\mathbf{C}_i-\mathbf{C}^c)\right]^{-1}\sin\theta\, d\chi_i\, d\theta\, d\phi\, d\psi\right\}\times \\ &\quad \left\{\sum_{i=1}^{n} v_i \int P_i(\chi_i;\theta,\phi,\psi)\left[\mathbf{I}-\mathbf{g}_i(\mathbf{C}_i-\mathbf{C}^c)\right]^{-1}\sin\theta\, d\chi_i\, d\theta\, d\phi\, d\psi\right\}^{-1} \end{aligned} \quad \text{(B.1)}$$

where, v_i and $\mathbf{C}_i$ are the volume concentration and elasticity tensor of the i^{th} component respectively. $\mathbf{I}$ is the fourth rank unit tensor. The tensor $\mathbf{C}^0$ is the elasticity tensor of the so called comparison body which can be arbitrarily chosen. The tensor $\mathbf{g}$ is controlled by the properties of the comparison body and the inclusion shape. θ, ϕ and ψ are the three Euler angles.

The tensor g has a definite form for each type of inclusion (Bayuk et al., 2007a), as expressed in the follows equation:

$$g_{kmln}(\mathbf{x}) \equiv \frac{(a_{kmln} + a_{knlm})}{2}, \tag{B.2}$$

where

$$a_{iklm}(\mathbf{x}) \equiv \int_v G_{ik,lm}(\mathbf{x} - \mathbf{x}_1) d\mathbf{x}_1. \tag{B.3}$$

Here, $G_{ik,lm}$ is the second derivative of the Green's function with respect to lm, and a is the fourth rank tensor which is constant in the case of ellipsoidal inclusion, and can be written as

$$a_{imjn} = -\frac{1}{4\pi} \int_0^{\pi} \int_0^{2\pi} n_{mn} \Lambda_{ij}^{-1} d\Omega, \tag{B.4}$$

where

$$\begin{aligned} \Lambda_{ij} &\equiv C^0_{imjn} n_{mn}, \\ n_{mn} &\equiv n_m n_n, \end{aligned} \tag{B.5}$$

and

$$\begin{aligned} n_1 &= \frac{\sin\theta\cos\phi}{a_1}, \\ n_2 &= \frac{\sin\theta\sin\phi}{a_2}, \\ n_3 &= \frac{\cos\theta}{a_3}. \end{aligned} \tag{B.6}$$

$\mathbf{C}^0$ is the comparison body, a_1, a_2 and a_3 are the semi-axes of the ellipsoidal inclusion, and $d\Omega \equiv \sin\theta \; d\theta \; d\phi$.

Appendix C

Thomsen's Parameters in TI and Orthorhombic Media

C.1 VTI Media

VTI and orthorhombic media have three mutually orthogonal planes (Figure C.1). Let's represent these three orthogonal planes by $X1-X2$, $X2-X3$, and $X1-X3$. In the case of VTI medium, let's assume that the axis $X3$ represents the axis of symmetry, and therefore, plane $X1-X2$ will be the plane of isotropy. Also, there will be no shear wave splitting along the axis $X3$. That means the velocity of P-wave traveling in plane $X2-X3$, and $X1-X3$ will be the same, and so will be the two shear waves.

A Transversely isotropic medium can be fully defined by five independent elastic constants (Figure C.2). According to Thomsen (1986), a weakly TI media can be explained by three Thomsen's parameters (ϵ, γ and δ), which are basically the ratio of stiffness tensors (equation C.1, C.2 and C.3).

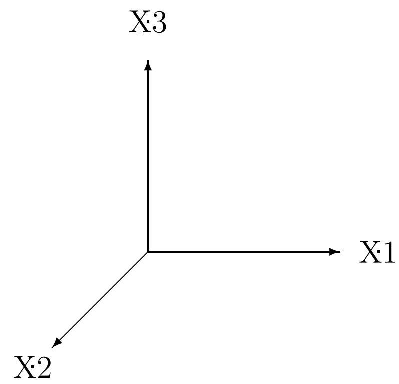

Figure C.1: Three mutually orthogonal planes in VTI, or orthorhombic media. In VTI media, plane X1-X2 will represent the plane of isotropy and X3 will be the axis of symmetry. In orthorhombic media, each of the three planes will be an anisotropic plane.

$$
\begin{array}{cc}
\textbf{(VTI symmetry)} & \textbf{(Orthorhombic symmetry)} \\
C_{IJ} = \begin{pmatrix} c_{11} & c_{12} & c_{13} & 0 & 0 & 0 \\ c_{12} & c_{11} & c_{13} & 0 & 0 & 0 \\ c_{13} & c_{13} & c_{33} & 0 & 0 & 0 \\ 0 & 0 & 0 & c_{44} & 0 & 0 \\ 0 & 0 & 0 & 0 & c_{44} & 0 \\ 0 & 0 & 0 & 0 & 0 & c_{66} \end{pmatrix} ; & C_{IJ} = \begin{pmatrix} c_{11} & c_{12} & c_{13} & 0 & 0 & 0 \\ c_{12} & c_{22} & c_{23} & 0 & 0 & 0 \\ c_{13} & c_{23} & c_{33} & 0 & 0 & 0 \\ 0 & 0 & 0 & c_{44} & 0 & 0 \\ 0 & 0 & 0 & 0 & c_{55} & 0 \\ 0 & 0 & 0 & 0 & 0 & c_{66} \end{pmatrix} \\
where, c_{12} = c_{11} - 2c_{66} &
\end{array}
$$

Figure C.2: Stiffness tensors in VTI and orthorhombic symmetry system. Note that five and nine independent elastic constants are required to characterize VTI and orthorhombic media, respectively.

$$\epsilon = \frac{c_{11} - c_{33}}{2c_{33}} \tag{C.1}$$

$$\gamma = \frac{c_{66} - c_{44}}{2c_{44}} \tag{C.2}$$

$$\delta = \frac{(c_{13} + c_{55})^2 - (c_{33} - c_{55})^2}{2c_{33}(c_{33} - c_{55})} \tag{C.3}$$

C.2 Orthorhombic Media

If these three axes represent orthorhombic medium, then each of the three planes will be anisotropic, and therefore, the splitting of the shear waves will take place along all three mutually perpendicular axes. An orthorhombic medium can be fully characterized by nine independent elastic constants. Tsvankin (1997) derived the anisotropic parameters for the orthorhombic medium in each of the three planes, as shown below.

Thomsen's parameters in the $X1 - X3$ plane:

$$\epsilon^{(2)} \equiv \frac{c_{11} - c_{33}}{2c_{33}}, \tag{C.4}$$

$$\gamma^{(2)} \equiv \frac{c_{66} - c_{44}}{2c_{44}}, \tag{C.5}$$

$$\delta^{(2)} \equiv \frac{(c_{13} + c_{55})^2 - (c_{33} - c_{55})^2}{2c_{33}(c_{33} - c_{55})}. \tag{C.6}$$

Thomsen's parameters in the $X2 - X3$ plane:

$$\epsilon^{(1)} \equiv \frac{c_{22} - c_{33}}{2c_{33}}, \tag{C.7}$$

$$\gamma^{(1)} \equiv \frac{c_{66} - c_{55}}{2c_{55}}, \tag{C.8}$$

$$\delta^{(1)} \equiv \frac{(c_{23} + c_{44})^2 - (c_{33} - c_{44})^2}{2c_{33}(c_{33} - c_{44})}. \tag{C.9}$$

Thomsen's parameters in the $X2 - X3$ plane:

$$\delta^{(3)} \equiv \frac{(c_{12} + c_{66})^2 - (c_{11} - c_{66})^2}{2c_{11}(c_{11} - c_{66})}. \tag{C.10}$$

Tsvankin (1997) pointed out that $\epsilon^{(3)}$ and $\gamma^{(3)}$ would be redundant for this plane.

Appendix D

Numenclature

$\mathbb{B}$ = Pair correlation function

C_{ijkl} or $\mathbf{C}$ = Fourth rank stiffness tensor

$\mathbf{C}^0$ = Stiffness tensor of the comparison body

C^*_{ijkl} or $\mathbf{C}^*$ = Fourth rank effective stiffness tensor

C'_{ijkl} or $\mathbf{C}'$ = Fluctuation in stiffness tensor

$\mathbf{C}^c$ = Stiffness tensor of the comparison body

$\mathbf{C}^c$ = Stiffness tensor of the matrix

$\mathbf{C}^I$ = Stiffness tensor of the inclusions

f_i = Body force

$\mathbf{G}$ = Green's function

g_{ijkl} = Local operator or singular component of the second derivative of the Green's function

$\mathbf{I}$ = Fourth rank unit tensor

$\mathbf{k}$ = Wave vector

K = Bulk modulus

K^* = Effective bulk modulus

P_i = Volume concentration of the i^{th} type of inclusion

$\mathbf{Q}$ = Integral operator or functional

$\mathbf{S}$ = Compliance tensor

$\mathbf{U}$ = Displacement

$\mathbf{U}'$ = Fluctuation in displacement

V_P = P-wave velocity; V_{S1} and V_{S1} = Two shear wave velocities

χ_i = aspect ratio of the i^{th} type of inclusion

δ_{ij}= Kronecker's delta

ε'_{ij} = Fluctuation in strain

ε, γ, and δ = Thomsen's parameters

λ and μ = Lamè parameters

μ = Shear modulus

μ^* = Effective shear modulus

ν = Volume concentration of a phase

ω = Angular/Cyclic frequency

ϕ = Total porosity

Φ = Crack-induced porosity

ρ = density

σ_{ij} = Stress

ε_{ij} = Strain

σ'_{ij} = Fluctuation in stress

θ, ϕ and χ = Euler angle